POLITECNICO DI MILANO
DEPARTMENT OF ELECTRONIC, INFORMATION AND BIOENGINEERING
DOCTORAL PROGRAMME IN INFORMATION

A TIME SERIES SYNTHESIZER OF TROPOSPHERIC IMPAIRMENTS AFFECTING SATELLITE LINKS DEVELOPED IN THE FRAMEWORK OF THE ALPHASAT EXPERIMENT

Doctoral Dissertation of:
Laura Resteghini

Supervisor:
Prof. C. Capsoni

Tutor:
Prof. M. D'Amico

The Chair of the Doctoral Program:
Prof. C. Fiorini

Year 2014 – Cycle XXVI

To my three best Projects:
my husband and my kids

"Life is the most romantic of all adventures,
but only those with an adventurer's heart can understand this."
Gilbert Keith Chesterton, Ortodossia, 1908

Acknowledgements

There are many people I would like to thanks that have encouraged and supported me during this PhD experience.

I would like to express my deep gratitude to Professor Carlo Capsoni, my research supervisor, for his patient guidance, encouragement and useful critiques of this research work. He was always available especially inspiring new solutions to research problems. I would also like to thank Professor Carlo Riva, for his advice and assistance, for the technical support with the databases and for the clarity in his explanations. My grateful thanks are also extended to Professor Aldo Paraboni who supported me during the Master thesis and my first experience as temporary researcher at the Politecnico. He introduced me to the propagation world, and encouraged me in starting my working experience as researcher. I will never forget his kindness, faith in me and his curiosity in going more into detail when a problem arisen. I would also like to extend my thanks to my colleagues Roberto Nebuloni and Lorenzo Luini and to my ex-colleagues Marco Luccini, Giacomo Amisano and Matteo Oldoni. Your friendship and your support expressed both on technical aspects and during the coffee breaks have been fundamental for the development of my work and especially for the writing of this thesis. Special thanks should be given to the staff, researcher professors of the Department: Michele D'Amico, Guido Gentili, Marco Ferrari, Marco Simonini, Ernestina Parente and Nadia Prada. A special thanks also to Antonio Martelluci who help me in my first experience as researcher at ESA. I am grateful to my colleagues of the open space: Francesco, Cristina, Giulia, Shalini, Sonda, Salar and Alessandro for their friendship.

Finally, I wish to thank my family. My parents that drive me from the early years to be inquiring. My husband Roberto for his support and encouragement throughout my PhD experience. Without his constant friendship, his love and his patience, probably I would never enjoined so much this amazing journey. And finally my two kids: Martina that survived for several months without her mum during the thesis composition (without making me feel guilty) and Tommaso that helped me writing the thesis without causing too much stress and nausea! This work is dedicated to you.

Abstract

TELECOMMUNICATION industry is rapidly moving toward the study and development of satellite system which exploit Extremely High Frequency bands (Ka and Q/V bands) to transmit broadcasting and telecommunication services. For these frequency bands, the capacity of the channel is increased to enable service like broadband internet access, but the transmitted signal are severely attenuated by the atmospheric components. Satellite system can exploit the use of Propagation Impairment Mitigation Techniques (PIMT) to reduce the negative effects of fading due to atmosphere but their development and design must be supported by the use of tropospheric channel models and synthesizers able to characterize the time varying channel not only in statistical terms.

In this work we focused on the study and development of a tropospheric time series synthesizer based on a large database of measurements. The use of data measured in propagation campaigns ensures a realistic behaviour of each atmospheric element. The synthesizer takes in input the long term statistic of rain attenuation, cloud and water vapor for a given location and return the time series of total attenuation that reproduces the input statistics. The model is valid for every link for site located in temperate regions.

Contents

CHAPTER 1

Introduction

The increasing diffusion of broadband internet connection and the development of Ultra High Definition TV (UHTV) requires the use of satellite communication systems able to provide large frequency bandwidth by making use of radio frequency carriers (Extremely High Frequency - EHF) up to Q/V Band. Moreover, the high channel capacity enables the system to provide high-speed, point-to-point wireless local area networks and broadband Internet access.

Some satellite-based service providers, such as EUTELSAT Company, start using satellite operating in Ka Band despite, at such these frequencies, the system has to cope with very strong attenuation introduced by the tropospheric constituents. Indeed, the physic of the channel is mostly influenced by the working frequency, and the gathered attenuation, which affects the signal, increases in severity with the increase of frequency. For a satellite system above Ka band, it is required the characterization of propagation factors that are normally considered negligible at lower frequency bands as clear-sky components (oxygen and water vapor) and clouds. The main source of signal degradation for satellite systems operating at these frequencies is represented by rain. However, even if rain strongly affects the signal power, this attenuation is limited in space and time. Clouds are present for the majority of the time and together with water vapor and oxygen represent the 'plateau' attenuation during rainy and non rainy periods.

In this respect, several Propagation Impairment Mitigation Techniques (PIMT) have been introduced to counteract all tropospheric impairments. These techniques exploit the peculiar properties of the atmospheric phenomena (rain events space and time decorrelation) and/or available on board extra resources (power, adaptive signal modulation and coding) and ensure an higher throughput and availability of the system. The design of a communication system exploiting PIMT requires the full characterization

of the medium between the transmitter and the receiver, not only in statistical terms but also in a time varying condition. Moreover, the accuracy of the testing procedure depends upon the ability of the synthesized scenario in reproducing all tropospheric components. Italy, through the Italian Space Agency ASI, has proposed and promoted the use of the experimental Q/V band frequency systems as part of the payload onboard Alphasat satellite launched on 25^{th} July 2013. One of the long-term scientific objectives is to collect data to design future PIMT. Furthermore, H2020-EO-2014-LEIT SPACE underline the necessity of a complete knowledge and modelling of atmospheric components in order to perform the validation of satellite systems. In this contest, the development and implementation of a time series synthesizer that allows the generation of the time varying condition of the channel through a careful characterization of the dynamic of attenuation that mimic measured time series represents an essential instrument. In the past, experimental data were used to carry out the design procedure. Unfortunately, they are not always worldwide available and if present, they have been collected for short periods.

The study performed during this PhD research focused on the investigation and modelling of the atmospheric components that mainly affect the transmission of signals in free space condition. In particular, the aim of this study is the development of a generator of time series of attenuation to simulate the variability in time of the tropospheric components separately and their combination in total attenuation for working frequencies up to 70 GHz. The basic idea is to start from real measurements collected during propagation campaigns to generate time series of attenuation for each atmospheric component reproducing the statistic of attenuation at a selected location for defined Satcom parameters (frequency, elevation angle). The input database is accurately modified and scaled to better adapt to the site-specific climatology of the location. The measurement database taken into consideration is the one provided by the ITALSAT experiment over 7 years of measurements. The data collected by different instruments (radiometer, beacon receiver and raingauge) are used to generate a database of time series for water vapor, clouds and rain events. The synthesizer generates for each atmospheric component, separately, a time series of attenuation of measured data and then a time series obtained by the combination of all atmospheric effects (water vapor, oxygen, clouds and rain). The model is considered applicable to middle latitude region for satcom systems with working frequency between 5 and 70 GHz and elevation angle between 5° and 90°.

In the literature there are several synthesizers devoted to the generation of time series of rain attenuation, but only another tropospheric time series synthesizer is now available. This model, defined in Rec. ITU-R 1853 [1] aims at modelling all atmospheric components and effects (water vapor, oxygen, clouds, rain and scintillations) for terrestrial paths and earth-satellite slant paths. The frequency is included between 5 and 70 GHz and elevation angle between 5° and 90°. The generation of single atmospheric components is obtained separately and finally they are properly combined. Clouds and rain distributions are approximated by a log-normal distribution while for the water vapor a Weibull distribution is assumed. The distribution parameters can be determined from local measured data from experimental data or from ITU-R models [1].

The peculiarity of the synthesizer developed in this study is the strong physic back-

ground ensured by the use of data measured in propagation campaigns. We considered as input three different databases: one composed by daily time series of liquid water, another by daily time series of water vapor and the third by time series of rainy attenuation events. The input databases, appropriately scaled to ensure the presence of the higher values of cloud, water vapor and rain attenuation, maintain the realistic behaviour of each events. We keep together the daily liquid water and water vapor time series to allow the joint generation of two time series that preserve the synchronous variation of the two processes as they are measured. Indeed, the two quantities cannot be considered as completely disjoint but there is a relationship underlined by the daily, seasonal and annual behaviour of these quantities. The adoption of measured data ensures the natural maintenance of this relationship. In the case of the rain attenuation events database, the collected measurements ensure the realistic shape of events and the presence of an adequate variability and number of events to accurately reproduce the statistics of any location. Finally, the composition of all tropospheric components is achieved through a new algorithm based on the identification and classification of cloud types (Cloud Type Algorithm CTA). This new procedure guarantees an accurate superimposition of all events according to the physical properties of clouds.

In this framework we assess the ability of the time series synthesizer in reproducing the climatology of a given location by selecting measured time series of clouds, water vapor and rain. The outcome of this study could potentially be used within these contexts:

- investigation and design of PIMT, as Uplink Power Control ULPC and Adaptive Code and Modulation ACM, which need a full characterization of the propagation channel (rain and non rain attenuation). In particular, for such techniques, the study of the short term fluctuations of the signal is fundamental for the characterization of control loop parameters;
- testing of PIMT that requires an accurate reproduction of a realistic scenario for non rainy and rainy condition for site specific climatology.

1.1 Thesis outline

Here we report a short description of the contents of the thesis to give a general overview of the work.

Chapter 2

In the first part of Chapter 2 we provide a description of the most relevant fading effects caused by atmospheric components of interest for satellite systems with transmitting frequency above 10 GHz. After a short overview of the composition of atmosphere, we focus on the tropospheric components represented by: water vapor, oxygen, hydrometeores in form of cloud and rain and finally turbulence. Water vapor and oxygen induce an absorption effect on the transmitted signal while hydrometeores introduce both absorption and scattering effect. Furthermore the rain particles introduce a depolarization effect. Finally turbulence induce a fast fluctuation of the received signal (scintillations). In the second part of the chapter we briefly make an overview of main Propagation Impairment Mitigation Techniques (PIMT) exploited by earth-satellite system to counteract the fading of the atmosphere, and those that could be

designed and implemented making use of a tropospheric time series synthesizer.

Chapter 3
In Chapter 3 we make a review of the most relevant time series synthesizer of atmospheric components. These models can be subdivided into two categories: atmospheric synthesizer for modelling rain attenuation and for total attenuation. The former class contains models based on: the Maseng-Bakken model [2], statistical conditional probabilities [3] [4], Markov chains [5] and synthesis of rain rate series and conversion to attenuation [6]. The latter class includes only the tropospheric attenuation time series synthesizer described Rec.ITU-R P.1853-1 [1] and the model presented in this thesis.

Chapter 4 In Chapter 4 we begin considering the non rainy attenuation components focusing in particular on the modelling of Integrated Liquid Water Content (ILWC) and Integrated Water Vapor Content (IWVC). To retrieve ILWC and IWVC quantities we take as input the radiometric data collected during ITALSAT campaign (7 years from 1994 until 2000) in Spino d'Adda. One critical step of this retrieval is represented by the identification, discrimination and interpolation of the rainy periods in order to avoid the error in the esteem of ILWC and IWVC. The rainy periods identification is obtained considering three databases of measurements (raingauge, beacon receiver and radiometer) properly combined. Then, the annual seasonal and daily trend of ILWC and IWVC quantities is analysed to verify if their time variation and behaviour shows a dependency from each other. We assess that ILWC and IWVC cannot be considered as completely disjoint as highlight by the conjunct classification of ILWC and IWVC daily time series. We assumed 24 hours as the basic time frame for the time series of ILWC and IWVC. Consistently with this observation, during the cloud and water vapor time series generations we prefer to maintain a connection between ILWC and IWVC daily time series, instead of keeping separated the two synthesize procedures.

Chapter 5
In Chapter 5 we describe the functionality of the time series synthesizer for ILWC and IWVC components. Daily time series are properly catalogued into a set of classes according to ILWC and IWVC maximum values. The resulting databases (one for ILWC and IWVC) are assumed, after an appropriate scaling, as suitable for the generation of time series in temperate climate for middle latitude sites. The synthesis of ILWC an IWVC is performed with two separated procedures. The cumulative distribution functions (objective CDF) of ILWC and IWVC are taken as input by two optimization procedures that return the number of daily time series to be selected from each ILWC and IWVC class. For the time series selection, we identify the daily time series of ILWC and IWVC that jointly satisfy the solution of the two optimizations. The synthetic time series are validated over 7 sites to assess the ability of the system in reproducing the input statistics of ILWC and IWVC (*discrepancy factor*). Furthermore, to give a feeling of the realistic behaviour of synthetic time series automatically introduced by the synthesizer we qualitative assessed the realistic behaviour of intra annual variability.

Chapter 6
In Chapter 6 we focused on the synthesis of rain attenuation events. We generated a database composed of time series of attenuation of rainy events extracted by 7 years (1994-2000) of measurements at 18.7 GHz in Spino d'Adda during the ITALSAT cam-

paign. Each time series of attenuation has a different duration and is catalogued in 10 classes according to the peak of attenuation it experiences. This database is assumed as input to reproduce the specific long term statistic of rain attenuation for any site in middle latitude regions. A dedicated optimization takes as input the objective CDF of rain attenuation, provided either by measured data or by ITU-R models, and return the total amount of rainy time to be selected from each class. Then, the events of rain attenuation are selected. The validation of the time series of attenuation synthesis is performed making use of DBSG5 database of measurements collecting an adequate number of sites and for numerous scenarios with different elevation angles and frequencies. The performance of rain synthesizer is assessed both for the first and second order statistics taking as reference the performance of ITU-R tropospheric time series generator [1].

Chapter 7

Finally, in Chapter 7 the composition of all synthesized effect is addressed to generate synthetic time series of total attenuation. As mentioned before, the time series of ILWC and IWVC are properly scaled to adapt to specified Satcom frequency and elevation angle. A constant value of oxygen attenuation is derived from ITU-R or radiosoundings for the defined frequency and elevation. The cloud intervals included into the ILWC time series are selected and catalogued to identify the ones that with higher probability sustain a rain event, the so called rainy windows. Then, the time series of total attenuation is built up by overlapping the rainy events to the proper rainy windows.

Chapter 8

In Chapter 8 we draw the conclusion of this work focusing in particular to the possible applications of the total attenuation time series generator and to future works.

Appendix A

The development of a synthetic time series of total attenuation requires an accurate superimposition of tropospheric phenomenon as water vapor, cloud and rain events. The cloud type algorithm described in this appendix helps in the identification of the cloud that have higher probability of rain inside and therefore suitable for overlapping rain events.

1.2 Main results obtained

1. Assessment of the retrieval technique of ILWC and IWVC from 7 years of radiometric measurements and development of a new procedure for the identification of rainy intervals within radiometric data. During this study we observed a non marginal relationship between ILWC and IWVC on daily basis which is useful to implement the time series synthesizer with properly correlated time series of ILWC and IWVC.

2. Development and implementation of a new algorithm for the identification and classification of clouds within the ILWC time series. The cloud type algorithm CTA helps in the identification of clouds that are interested by rain with high probability.

3. Development and implementation of a simulation tool to synthesize time series of total attenuation that includes tropospheric components of water vapor, oxygen, cloud and rain. The time series of the different atmospheric components are

properly combined and scaled to the defined Satcom frequency ad elevation angle. The synthesizer has been tested for frequency ranges between 5 and 70 GHz and elevation angles from 5° till 90°.

CHAPTER 2

Atmospheric attenuation and Propagation Impairment Mitigation Techniques

2.1 Introduction

The increasing use of frequency bands above 10 GHz for satellite services has highlighted the necessity for estimating propagation factors that are normally considered benign or negligible at the lower frequency bands. At these frequencies, rain attenuation is considered the dominant factor. In particular absorption and scattering caused by rain, hail, ice crystals, or wet snow can cause a reduction in transmitted signal amplitude (attenuation) which reduces the reliability and performance of the space communication link. Other effects can be depolarization and scintillations induced by atmospheric turbulence. Despite that, for system with low availability satellite links, also the characterization of cloud attenuation and water vapor is needed.

To counteract propagation effects, the simplest solution is oversize the system parameter (transmitted power), but it is not always feasible. Therefore, modern satellite system exploit Propagation Impairment Mitigation Techniques (PIMT) to cope with fading effects.

In the first part of this chapter we provide an overview of the main tropospheric components and their effects on the transmitted signal for satellite system with frequency up to 50 GHz. In the second part, we make a small review of PIMT that could take advantage, during the design and test phase, from the modelling of propagation channel by means of time series synthesizers.

Figure 2.1: *Atmosphere image take by International Space Station (ISS-NASA).*

2.2 Structure of the atmosphere

By studying the propagation channel characteristics of a satellite-earth radio-link it is mandatory to carefully investigate the Earth atmosphere. The atmosphere is a thermodynamic system composed essentially by water, gas and aerosol in different percentages that surrounds the Earth till about 500 km. This region is where several physical processes essential for the life on the Earth take place. The composition of the atmosphere is constituted by nitrogen (78%), oxygen (21%), argon (0.9%), carbon dioxide (0.03%), water vapor (0.0 to 4.0%) and trace of gases (neon, helium, krypton, and xenon). The atmosphere's pressure and density decrease exponentially with altitude forced by gravity. The variation of atmospheric temperature with height,exhibits a cycling pattern, caused by solar and Earth's radiation. The atmosphere is subdivided into layers according to their thermal state. The vertical changes in temperature are important since they produce weather events to the closest Earth's surface region. The scheme of the layers of atmosphere is reported in Fig. 2.2.

The ionosphere is the higher part of the atmosphere from about 60 km till 450 km of altitude. The ionosphere represents the lower part of the thermosphere, a region where temperature can rise up to 2000 K due to the solar radiation. In this layer, the solar radiation (in form of ultraviolet radiation and X-ray) generates the ionisation of gas molecules contained in the atmosphere. The ionisation is defined as the number of free electron per volume unit and it depends mainly from solar radiation intensity, pressure and atmosphere composition. The pressure and atmospheric composition is dependent from the altitude while the solar radiation has a cyclic variability according to the night/day time and season. Therefore, due to its different electrical structure, the ionosphere is generally represented as a structure of layers, whose depth is variable. A generalized model of the vertical structure of the atmosphere is given by the 1976

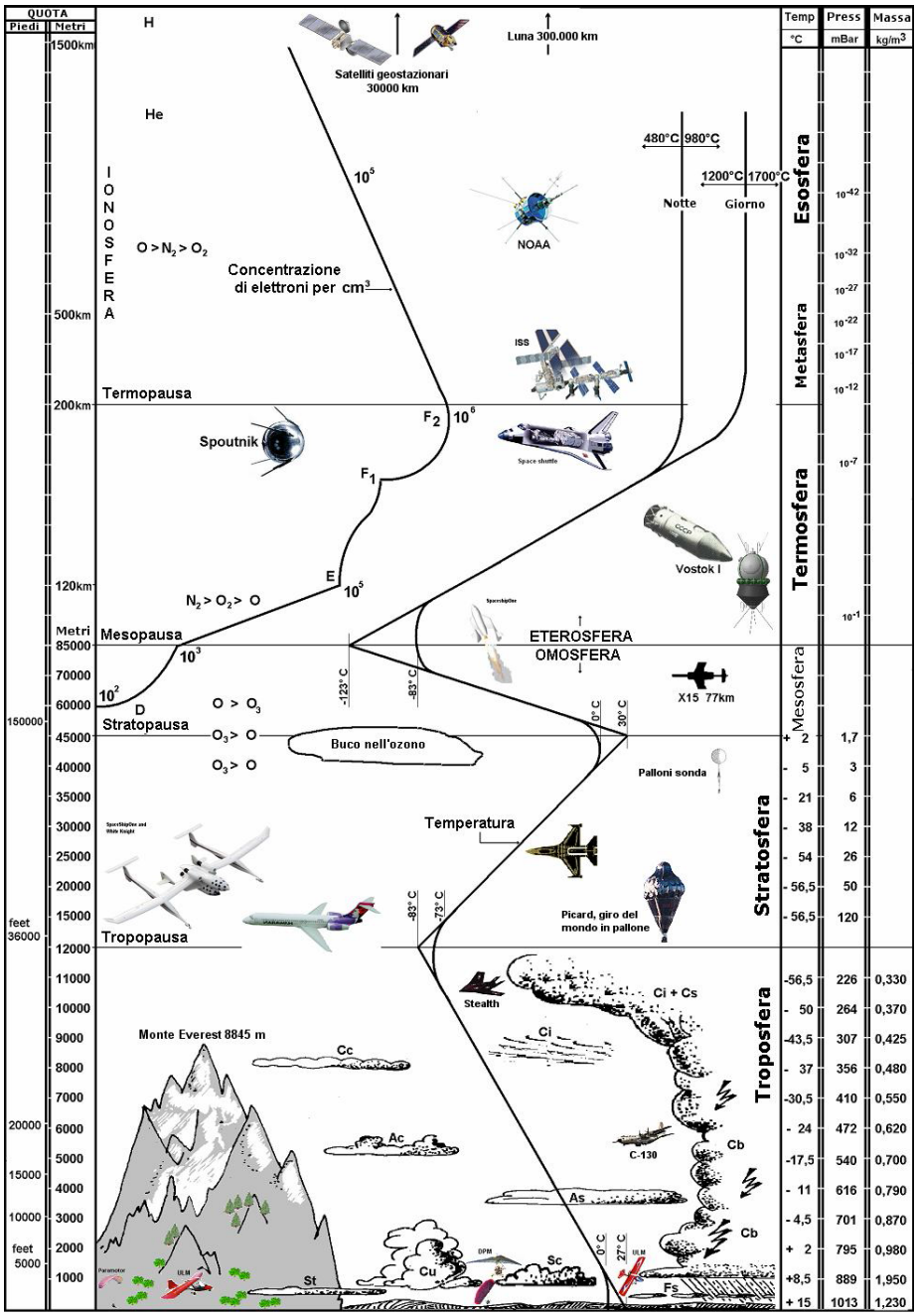

Figure 2.2: *Atmosphere structure and layers.*

U. S. Standard Atmosphere. Annual, seasonal and monthly averages of temperature, pressure and water-vapour pressure as a function of altitude are provided by ITU-R model.

The mesosphere is a layer located around 50 and 90 km altitude and it is the coldest region of the atmosphere.

The stratosphere is a region between about 11-12 km and 50 km, where air flow is mostly horizontal. In this layer the temperature increases due to strong absorption of solar ultraviolet radiation by the ozone layer, located near 25 km above the earth's

surface. The ozone layer is fundamental since it prevent an intense flux of ultraviolet radiation from reaching the surface.

The troposphere, is the lower layer of the atmosphere (from Earth's surface to 11-12 km). It is where all the Earth weather phenomenon are originated and it contains the 80% percentage of the mass of atmosphere. The temperature, pressure and density of the air is decreasing constantly with the increasing of altitude. Indeed the troposphere is heated by "the ground" and ocean. Sunrise radiate the surface that generate warm air that tends to rise and became colder. The troposphere contains the 99% of the water vapor in the atmosphere. Water vapor concentrations vary with latitude (from north to south). The thickness of troposphere is dependent from the latitude: is about 16 km at the equator and 8-12 km at the poles.

In this work we focus on the study of the behaviour of tropospheric components, that are the primary source of degradation of signal for transmission frequency above 10 GHz. The troposphere affects the electromagnetic waves in the microwave band in two different ways: the clear-air effects of gases and eater vapor induce signal delay, ray bending, absorption, reflection and tropospheric scattering, while the hydrometeores (fog, clouds, precipitation, aerosols) produce attenuation, cross polarization and scattering. The fading effects caused by each tropospheric phenomenon is investigated in the next section.

2.3 Tropospheric components

The absorption effects of the troposphere is mainly caused by its composition: dry part (nitrogen, oxygen, argon, carbon dioxide, water vapor) and liquid water (fog, clouds, hydrometeores) and finally pollution and aerosol.

The clear-sky attenuation is due to gasses and in particular oxygen and the water vapor. Water vapour is primarily found in the troposphere. indeed almost 50% of water vapour in the atmosphere is found between 0 and 1.5 km. Less than 5-6% of water vapour is found above 5 km and less than 1% is found in the stratosphere. This source of attenuation is always present and, while the oxygen can be assumed as constant without losing generality, the water vapor is highly variable during the year.

The attenuation due to hydrometeores (cloud, fog and rain drop) is dependent on two factors: the energy absorption caused by Joule effect and the wave diffusion induced by the particles. The attenuation generated by hydrometeores can be classified into cloud attenuation and rain attenuation. The cloud attenuation is dependent on small hydrometeores or liquid water suspended in the troposphere in forms of clouds or fog. The rain attenuation is due to bigger hydrometeores precipitating and is the main source of attenuation, even if it is particularly limited in time and space.

2.3.1 Gaseous attenuation modelling

Electromagnetic wave propagation in the frequency range from 20 till 300 GHz is affected by fading effects due to gaseous attenuation mainly caused by the absorption of two components: the dry part of atmosphere (oxygen) and the water vapor.

Absorption of electromagnetic energy by gaseous molecules usually involves the interaction of electric or magnetic component of the incident wave with an electric or magnetic dipole [7]. The oxygen molecule has a permanent magnetic moment arising

from two unpaired electron spins. Magnetic interaction produces a family of rotation lines around 60 GHz and an isolated line at 118.8 GHz.

Water vapor is a molecule with an electric dipole. Through an electric interaction with the incident electric field, water vapor produces rotational lines at 22.2, 183.3, and 323.8 GHz and at several frequencies in the far-infrared band. Each of the absorption spectral lines has a certain width because the energy levels vary when molecules are in motion. In Fig. 2.3 are reported the zenith profile of attenuation for water vapor and oxygen for a frequency range up to 350 GHz [8].

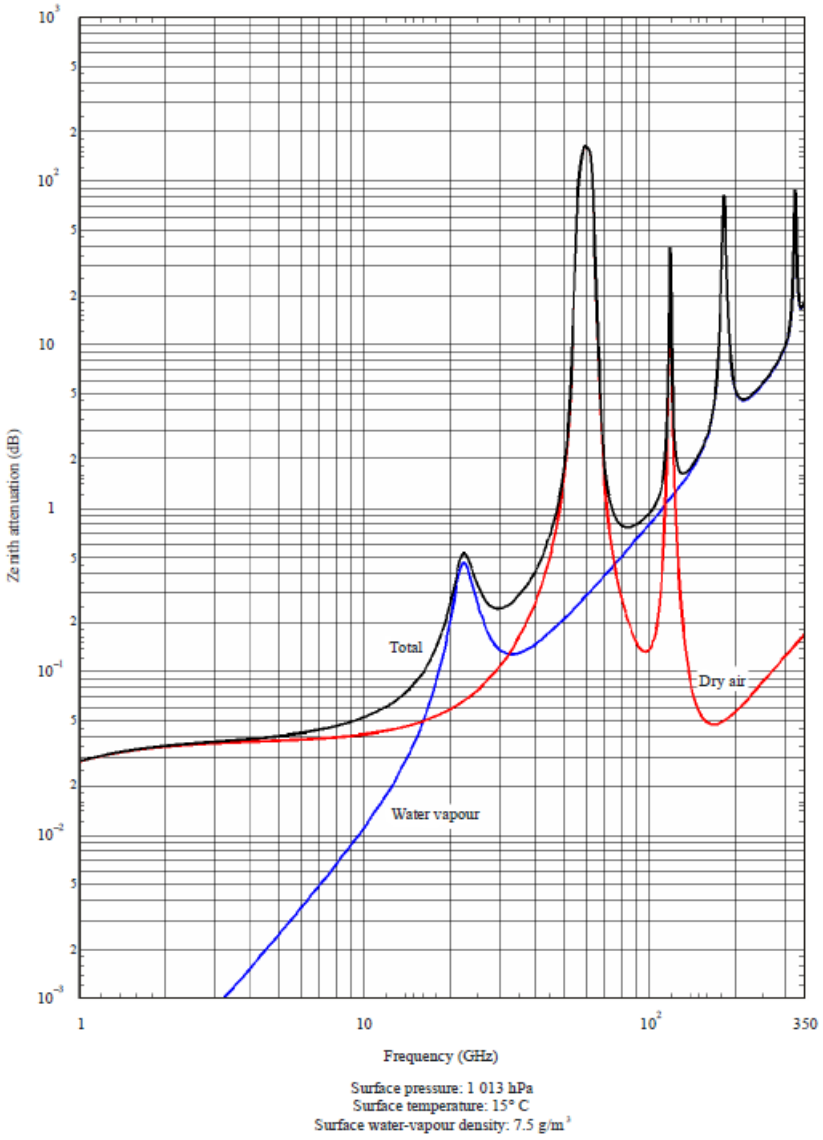

Figure 2.3: *Zenith profile of oxygen and water vapor attenuation as dependent from frequency [8].*

The specific attenuation γ_g due to gases [dB/km] in Rec. ITU-R 676-10 [8], is defined as the sum of specific attenuation due to oxygen γ_{OXY} and water vapor γ_V as function of frequency f:

$$\gamma_g(f) = \gamma_{OXY}(f) + \gamma_V(f) = 0.01820 f N''(f) \tag{2.1}$$

with N'' the imaginary part of complex refractivity expressed as function of air pressure, water vapor and temperature. To integrate the specific attenuation along the slant path we need to model the atmosphere as horizontal layers, specifying the profile of pressure, temperature and humidity along the path by means of radiosounding or, in case not available, with Rec. ITU-R 835-5 [9], using the Microwave Propagation Model [10]. The zenith attenuation due to gases A_g [dB] through the Earth's atmosphere is defined as the sum of zenith attenuation due to oxygen A_{OXY} and water vapor A_V as function of frequency f [GHz]:

$$A_g(f) = A_{OXY}(f) + A_V(f) = \int_h^\infty \gamma_{OXY}(z,f)dz + \int_h^\infty \gamma_V(z,f)dz \tag{2.2}$$

where h is the station altitude. Assuming an elevation angle θ comprise between 5° and 90° we calculate the path attenuation through the cosecant law as:

$$A_g(f) = \frac{A_{OXY}(f) + A_V(f)}{\sin(\theta)} \tag{2.3}$$

In case high accuracy is not required, a simplified procedure evaluates the gas attenuation in most of the cases up to 350 GHz is also described in [8]. The yearly averaged gaseous attenuation at the zenith can be calculated, by multiplying the approximated gaseous specific attenuation at ground level, which is a function of ground water vapour density, temperature and pressure, by its effective height, which depends only on frequency and pressure. Therefore, the total zenith attenuation is defined as:

$$A_g(f) = A_{OXY}(f) + A_V(f) = \gamma_{OXY} h_{OXY} + \gamma_V(z,f) h_V \tag{2.4}$$

where h_{OXY} and h_V are the equivalent height which are dependent on pressure, that can vary with latitude, season and climate. Assuming an elevation angle θ comprise between 5° and 90° we calculate the path attenuation through the cosecant law as in 2.3 making use of surface meteorological data.

2.3.2 Cloud attenuation modelling

Cloud and fog are composed by small suspended drops. The maximum diameter of the water droplets found in clouds is of the order of 50 μm [11]. Clouds are composed of water droplets and ice crystals. Due to the low dielectric constant of ice and the small size of the constituent particles, the ice cloud are not expected to cause appreciable attenuation to radiowaves for frequencies below about 50 GHz.

The attenuation due to fog is not significant for frequency below 100 GHz. For example, in case of moderate fog (0.05 g/m^3) the order of magnitude for attenuation is comprise between 0.002 dB/km and 0.1 dB/km for frequencies at 20 and 60 GHz, respectively, while for more heavy fog (0.5 g/m^3) it reaches 0.02 dB/km and 1 dB/km, respectively.

The Rayleigh approximation [12] of Mie scattering theory can be adopted for this drops diameter up to 200 GHz and therefore the cloud absorption is independent from the Droplet Size Distribution (DSD) within the cloud. The cloud attenuation results as dependent on Integrated Liquid Water Content ILWC and on temperature. In Rec. ITU-R 840-6 [13] cloud attenuation A_C [dB] is evaluated as:

$$A_C = \frac{L_{red} K_l}{\sin(\theta)} \tag{2.5}$$

Figure 2.4: *Cloud image take by International Space Station (ISS-NASA).*

with L_{red} [mm] the ILWC retrieved at 0°C, K_l the specific attenuation coefficient [(dB/km)/(g/m^3)] and θ lies between 0 and 90°. The specific attenuation coefficient K_l is defined as function of frequency f as:

$$K_l = \frac{0.819f}{\epsilon''(1+\eta^2)} \tag{2.6}$$

and

$$\eta = \frac{2+\epsilon'}{\epsilon''} \tag{2.7}$$

where ϵ is the complex dielectric permittivity of water, dependent from temperature, and evaluated across the frequency range 1-1000 GHz which uses a double-Debye relaxation approximation.

Several models are available for the prediction of cloud attenuation [14] [15], but they are either poor estimators or the input data required are difficult to obtain for a general purpose application. The best of these models is the Salonen [16] that suffers from a cosecant elevation angle dependence, which renders its use for low elevation angle paths questionable. Rec. ITU-R 840-6 [13] provides a model to predict the attenuation due to clouds and fog on Earth-space paths. In this recommendation they suggest also a method to predict the rain attenuation at one frequency knowing the propagation effect at a different one (frequency scaling procedure).

2.3.3 Rain attenuation modelling

Rain droplets result in absorption and diffusion of the incident radio wave energy, with independent contributions which may be integrated. The determination of rain attenuation is dependent from the precipitation intensity (rainfall rate R [mm/h]). The specific rain attenuation γ_R [dB/km] is expressed as a power law equation:

$$\gamma_R = kR^\alpha \tag{2.8}$$

where k and α are coefficients that depends on frequency and polarization. Several expression of these coefficients according to different polarization (horizontal or vertical) are reported in Rec. ITU-R 838-3 [17]. Assuming that rain is homogeneous along the inclined path, the rain attenuation can be obtained by multiplying the specific attenuation for a given rain intensity for the length of the path. However, since the rain can be assumed as homogeneous only for small areas, the attenuation A_R due to a rain volume L can be expressed by:

$$A_R = \int_0^L \gamma(x)dx \quad [dB] \tag{2.9}$$

where γ is the specific attenuation of the rain volume [dB/km]. The water drops are in first approximation assumed to be spherical, and the contributions of each drop are additive and independent of the other drops. Assuming a plane wave of power density P_t, incident on a volume of uniformly distributed spherical water drops of radius a, extending over a length L, the received power P_r is given by:

$$P_r = P_t e^{-cL} \tag{2.10}$$

where c is the attenuation coefficient for the rain volume [km^{-1}]. The attenuation is evaluated as:

$$A = 10 \log \frac{P_t}{P_r} = 4.343cL \quad [dB] \tag{2.11}$$

The attenuation coefficient c can be obtained as the product between the water droplets density per unit volume, ρ, and the extinction cross-section of drops Q_t, equal to the ratio between the lost power density and the total incident power density:

$$c = \rho Q_t \tag{2.12}$$

Q_t is the sum of the cross-sections for absorption and scattering, it is function of the drop radius a, the wavelength of the radio wave λ and the complex refractive index of the water drop m. Assuming $n(a)$ as the Drop Size Distribution DSD, c can be expressed as:

$$c = \int Q_t(a, \lambda, m)n(a)dr \tag{2.13}$$

$n(a)da$ can be interpreted as the number of drops per unit volume with radii between a and $a + da$. The specific attenuation γ is then derived from Eq. 2.11, with $L = 1$:

$$\gamma = 4.343 \int Q_t(a, \lambda, m)n(a)da \tag{2.14}$$

The above result emphasizes the dependence of rain attenuation on drop sizes, drop size distribution, rain rate and extinction cross-section. The first three parameters are characteristics of the rain structure only, the extinction cross-section introduces the dependence on the frequency and temperature. All the parameters exhibit time and spatial variability which are not deterministic, or directly predictable. Hence, most analyses of rain attenuation must resort to statistical means to evaluate the impact of rain on communication systems.

Q_t can be obtained by referring to the classical scattering theory of Mie for a plane wave radiation upon an absorbing sphere. If the wavelength is considerably larger than

the dimension of the drop ($2\pi a \ll \lambda$) the Rayleigh cross-section is:

$$Q_t = \frac{8\pi^2}{\lambda} a^3 \text{Im}\left[\frac{m^2-1}{m^2+2}\right] \tag{2.15}$$

The DSD, $n(a)$, depends on the rain rate and type of storm activity, it has been found to be well represented by an exponential function:

$$n(a) = N_0 e^{-\Lambda a} = N_0 e^{-[cR^{-d}]a} \tag{2.16}$$

where R is the rain rate in mm/h and a the drop radius in mm. N_0, c, d are constants to be determined from measured distribution and describe different kinds of rain.

Given the distribution of drop diameters in Eq. 2.16 and the rain cross section description, total rain attenuation for the path L is obtained by integration of Eq. 2.14 over the extent of the rain volume. This integration procedure is not a straight task since Q_t and r distribution generally vary along L and these variabilities must be included in the calculation.

The prediction of rain attenuation CDF starting from the rainfall intensity CDF represents a big effort for many researchers. Several model have been developed (SCExCell [18], ITU-R Rec. P.618-11 [19] and Synthetic Storm Technique [6]). In particular, the Rec. ITU-R 618-11 provides estimation of long-term statistic of rain attenuation for slant path for a satcom system up to 55 GHz. This model requires in input the point rainfall rate at 0.01 % of time, the working frequency and the parameters that characterize the earth station as elevation angle, altitude and latitude.

2.3.3.1 Hydrometeores depolarization

The depolarization effect [7] is introduced by non-spherical hydrometeores and ice that cause a change in polarization of the electromagnetic wave propagating through the atmosphere. This phenomenon affects system transmitting two independent orthogonal polarized signals for optimum RF spectrum utilization. The depolarization can induce a crosstalk, i.e. part of the energy transmitted by the original polarization (copolar channel) is transferred to the orthogonal polarization (cross-polar channel).

As the size of a hydrometeores increases, the shape changes from spherical to oblate spheroid. The drops may also be inclined with respect to the horizontal plane with an angle ϕ, due to the wind. In Fig. 2.5 we report an example of the system geometry. The non spherical shape of drops induce a difference in the propagation characteristics (phase coefficient and specific attenuation) along two drop axes.

The cross-polarization discrimination (XPD) defined for linear polarized waves, is expressed as:

$$XPD = 20 \log \frac{|E_{11}|}{|E_{12}|} \tag{2.17}$$

where E_{11} is the received electric field in the copolar channel and E_{12} is the electric field converted to the orthogonal cross-polar channel.

In Rec. ITU-R P.618-11 [19] an accurate description of the calculation of statistic of hydrometeor-induced cross-polarization is provided (due both to rain and ice). To evaluate the statistic, several parameter are required:

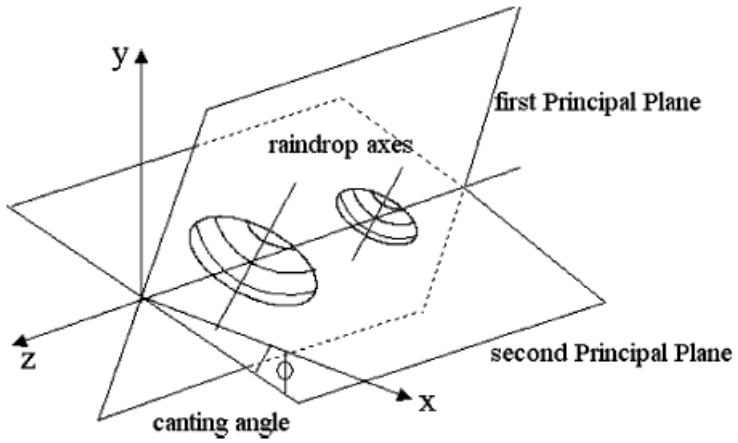

Figure 2.5: *Geometrical representation of the hydrometeores with spheroidal shape and inclined with respect to the principal planes [20].*

- A_p: rain attenuation exceeded for the percentage of time p, also called Co-Polar Attenuation (CPA) [dB];
- τ: tilt angle of the linearly polarized electric vector [deg];
- f: frequency [GHz] comprise between 6 and 55 GHz;
- θ: path elevation angle [deg] below 60°.

The XPD not exceeded for the p % of time is defined as follow:

$$XPD = U - V(f) \log_{10} CPA \tag{2.18}$$

where the coefficients U and $V(f)$ are dependent on frequency and on the variables previously listed. In particular we consider for V:

$$V(f) = \begin{cases} 30.8 f^{-0.21} & 6 \leq f < 9 \text{ GHz} \\ 12.8 f^{0.19} & 9 \leq f < 20 \text{ GHz} \\ 22.6 & 20 \leq f < 40 \text{ GHz} \\ 13.0 f^{0.15} & 40 \leq f \leq 55 \text{ GHz} \end{cases} \tag{2.19}$$

while for U we have the composition of several factors:

$$U = C_f + C_\tau + C_\theta + C_\sigma \tag{2.20}$$

In details we have a frequency dependent term C_f:

$$C_f = \begin{cases} 60 \log f - 28.3 & 6 \leq f < 9 \text{ GHz} \\ 26 \log f + 4.1 & 9 \leq f < 36 \text{ GHz} \\ 35.9 \log f - 11.3 & 36 \leq f \leq 55 \text{ GHz} \end{cases} \tag{2.21}$$

a polarization improvement factor C_τ:

$$C_\tau = -10 \log[1 - 0.484(1 + \cos 4\tau)] \tag{2.22}$$

a elevation angle dependent term C_θ:

$$C_\theta = -40\log(cos\theta) \tag{2.23}$$

and finally a canting angle dependent term C_σ:

$$C_\sigma = 0.0053\sigma^2 \tag{2.24}$$

where σ is the standard deviation of the raindrops canting angle distribution ϕ shown in Fig. 2.5. In [19] is also provided a scaling procedure to derive the XPD statistic for a given frequency starting from the statistic at another frequency and polarization tilt angle.

In [20] a new version for V band of Eq. 2.18 formulation is defined as [20]:

$$XPD = 0.5CPA - 33 \tag{2.25}$$

The relative error (averaged in the CPA range between 0 and 30 dB) between the model and measurements is about 3.5%, with a standard deviation of about 7%.

2.3.4 Scintillation

Scintillation [7] [19] are rapid fluctuations of the amplitude, phase, angle of arrival and polarization of the radiowave signal caused by time depending irregularities in the propagation channel. Scintillation of the received signal is caused by small-scale refractive index inhomogeneities induced by atmospheric turbulence along the propagation path. They affect signal properties for earth-space links above 10 GHz.

The scintillation magnitude is dependent on the variation of the refractive index and increases with frequency and path length. It decreases according to the decrement of the antenna beamwidth, due to the aperture averaging. It is seasonally and local climate dependent effects and it is more relevant in equatorial region. Slant paths at low elevation angles are most significantly affected by scintillation turbulence. Scintillation can have an impact on the performance of satellite system with low margin and may interfere with tracking systems or propagation impairment mitigation techniques.

In Rec. ITU-R P.618-11 [19] is provided a model to predict the attenuation due to scintillation by distinguishing among system at elevation angle above or below 5° and fades above or below 25 dB. Three different models are considered: above 5° of elevation angle, below 5° with fades above 25 dB and below 5° and fades below 25 dB. An overview of tropospheric scintillation models is presented in [21]. The statistical model [22] is based on the observation that scintillation is at least partly associated with the presence along the path of heavy cloud. Another statistical model for predicting tropospheric amplitude scintillation on a earth-satellite links is presented in [23]. The mean value and the variance of the log-amplitude fluctuations of the received electromagnetic field are directly derived from conventional radio-sounding observations.

2.4 Review of Propagation Impairment Mitigation Techniques

Nowadays satellite systems make use of high frequency ranges (20-70 GHz) to take advantage of higher capacity to transmit broadband service link HDTV and wide band internet. By utilizing higher frequency bands such as Ka (20-30 GHz) or Q/V (40-50

GHz) bands, for a traditional satellite system with fixed antenna front end are allocated respectively 1 GHz and 3 GHz [24]. At these frequency bands, the propagation channel induces strong fade on the transmitted signal causing all the propagation effects described so far: power absorption, depolarization, scattering, etc. Therefore, to allow the transmission at these frequencies without oversize satellite elements and power, several Propagation Impairment Mitigation Techniques (PIMT) are exploited. These techniques allow systems with small power margin to be effective in overcoming cloud, gas and rain attenuation while ensuring a given system availability. The availability is defined as the time percentage in a year when the Bit Error Rate (BER) is below the desired threshold. While, the fade margin is defined as the difference expressed in dB between the attenuation leading to an outage and the attenuation in clear-sky condition. There are different implementations of PIMT that can be catalogue into three categories [25]:

- EIRP control techniques: modification of the transmitted power or of the antenna gain in order to compensate channel absorption effects;
- Adaptive transmission techniques: adaptation of signal properties (code,modulation or both) to counteract signal degradation due to channel fading ;
- Diversity protection schemes: exploitation of rain spatial or temporal decorrelation to overtake rain events fading.

Several study have been carried on this subject [26],[27] and an accurate review of PIMT has been developed in the framework of COST 255 [28].

In this section the main PIMT are presented, going into detail for those that are mainly interesting for the exploitation of a synthesizer of time series of total attenuation. For these PIMT, the accurate time varying modelling of all tropospheric components (gas, clouds and rain attenuation) is a fundamental prerequisite for both design and testing. Indeed, as will be presented in the following chapter, the characterization of the propagation channel (not only in statistical term) is required for the design of the entire system properties and in particular for the PIMT control loop and finally for the testing procedure.

2.4.1 EIRP control techniques

In this category, the system adapts the transmitted power or antenna gain in order to counteract the attenuation induced by atmospheric components. The EIRP (effective isotropic radiated power), expressed as function of the transmitted power and the antenna gain, is the power that an isotropic antenna would emit to generate the same power density of the real antenna in the direction of maximum gain. The modification of the transmitted power can be performed both in up and down link, from ground or from satellite antenna (Uplink Power Control ULPC and Downlink Power Control DLPC). On the contrary, the antenna gain modification is performed only from satellite by means of a Spot Beam Shaping (SBS), where the shape of the antenna pattern is changed so that the power received on the ground remains nearly constant, even under rainfall conditions.

2.4.1.1 Uplink and Downlink Power Control

The power control technique [29] is usually performed at the ground station by adapting the transmitted power of the antenna to accomplish the channel fading condition. These systems restore the Carrier-to-Noise Ratio (C/N_0) through an increment of the Earth-Station transmitted power. The system can be controlled with an open or close control loop. For the close control loop, the satellite antenna evaluates the Signal to Noise Interference Ratio (SNIR) of the received signal and send at the ground antenna this information to accordingly modify the power of the transmitted signal. On the contrary, for the open control loop, the ground antenna evaluates the channel attenuation by making use of an ad-hoc signal transmitted by the satellite antenna and after a frequency scaling of the estimated attenuation on the downlink channel, the ground antenna modify the power of the transmitted signal in order to overtake the estimated uplink attenuation. An error can occur in the translation of the downlink attenuation into the estimated uplink attenuation. To the opposite, the close loop suffer of an intrinsic delay of the estimated attenuation of twice time of the round tripe between ground station and satellite.

Usually, the link quality is estimated in term of BER, therefore the close loop system must determine the required SNIR threshold who satisfy the BER target [30].

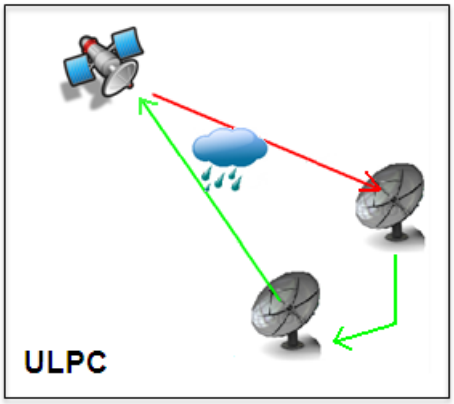

Figure 2.6: *Reconfigurable antenna (Downlink Power Control DLPC) scheme.*

The DLPC is generally non used since it is more complicated to control the onboard satellite power system directly from Earth. Several configuration of beamforming networks have been studied with traveling-wave tube amplifiers (TWTA) [31],[32] and multi-port amplifiers (MPA) [33], but it quite complicated to perform a real time change of the transmitted power.

2.4.1.2 Spot Beam Shaping

An example of the SBS is represented by the reconfigurable antenna system. The reconfigurable antenna, as shown in Fig. 2.7, exploits a multi-spot antenna controlled by a beamforming network to adaptively increases the transmitted power towards those sub-region affected by bad weather conditions, ensuring at least the desired amount of power to those region affected only by clear sky effects.

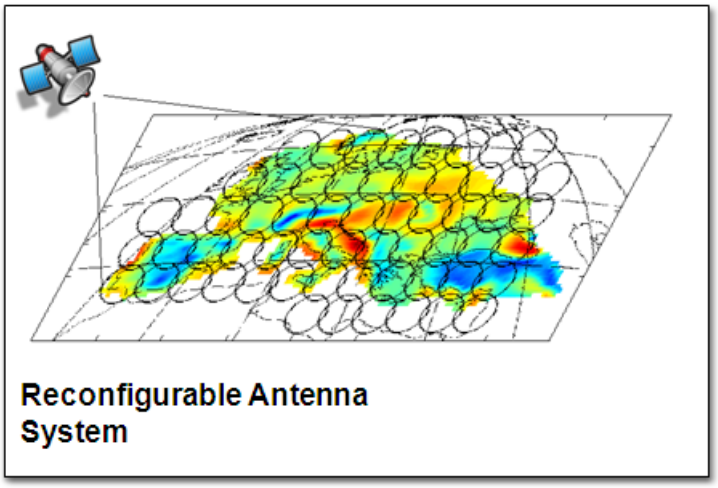

Figure 2.7: *Reconfigurable antenna (Downlink Power Control DLPC) scheme.*

2.4.2 Adaptive transmission techniques

The adaptive transmission technique modifies the transmitted signals adapting separately, or together, the code (Adaptive Coding AC), the modulation (Adaptive Modulation AM) or the data rate (Data Rate Reduction DRR) in order to maintain the required system availability. The objective of this class of PIMT is to reduce the vulnerability of the transmitted signal to error burst and to have a more robust modulation in case of fading condition.

2.4.2.1 Adaptive Coding and Modulation

The Adaptive Coding and Modulation (ACM), shown in Fig. 2.8, is a technique that modifies the single user information rate by changing modulation type and coding rate, while maintaining constant the symbol rate. The aim of this technique is to dynamically select, based on the current channel quality, the transmission Modulation and Coding (ModCod) pair which maximizes spectral efficiency satisfying the required BER.

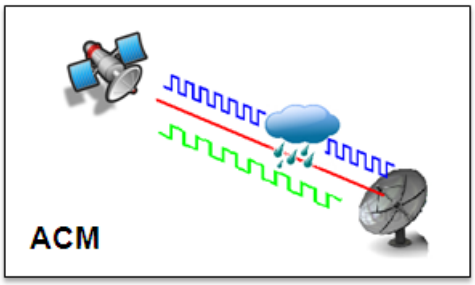

Figure 2.8: *Adaptive Coding and Modulation (ACM) scheme.*

The coding is adopted to ensure a redundancy in the transmitted signal and therefore reduce the negative effects of errors. With an increased redundancy (i.e. a more robust code) the probability of error decreases. At the same time, while the redundancy increases, the required bandwidth increases. In case of fading on the propagation channel, errors do not occur randomly but in burst, therefore a way to reduce this effect is to

introduce a more robust coding. The short fading effect can be reduced by using the interleaving [34] and in case of strong fading the concatenated codes can be implemented [34].

The change of modulation is adopted to modify the spectral efficiency (number of bit per second assuming a given bandwidth). When the system is in clear-sky condition, the transmitter increases the spectral efficiency of the system by adopting modulation scheme such as 16-PSK or 64-PSK, while in case of fading condition it use a more robust modulation scheme as BPSK or QPSK. Indeed, for M-ary PSK modulation scheme, the distance between consecutive amplitude and phase is reduced, therefore it is more sensitive to error [25].

ACM allows a decrease in the required C/N_0 while maintaining the link performance in terms of BER. AC and AM aim at a reduction in the required energy-per-information bit level (E_b/N_0), which translates into a decrease in the required C/N_0 [24].

2.4.3 Diversity protection schemes

The objective of these techniques is to re-direct or delay the transmitted signal in order to avoid impairments due to meteorological perturbation. These techniques are adopted only to prevent from rain attenuation, since these events are relatively localized and limited in time. The main relevant diversity technique is the Space Diversity (SD). The signal is transmitted by the satellite to two (or multiple) earth stations that are spaced in order to exploit the inhomogeneity of raincells. The signals received by the earth-stations are then transmitted to a master station that combines the received information (see Fig. 2.9).

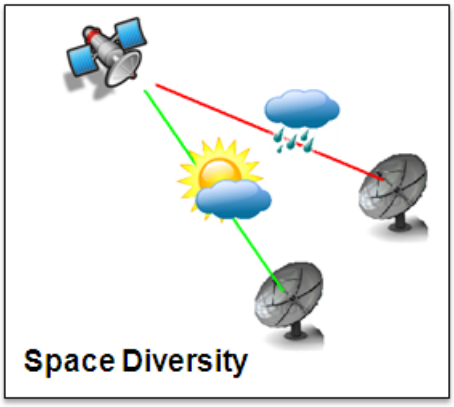

Figure 2.9: *Space Diversity (SD) scheme.*

CHAPTER 3

Review of dynamic channel models

3.1 Introduction

The design and implementation of satellite systems working at frequency above 20 GHz require the utilization of Propagation Impairment Mitigation Technique(PIMT) to cope with fade conditions caused by atmospheric components. At such frequency bands, the negative effects introduced by rain and atmospheric components as water vapor, cloud and oxygen become relevant and can severely affect the satellite-earth communication because of strong extra attenuations. Traditional satellite systems can overtake these attenuation effects with a large but uneconomical (if possible) over-dimensioning satellite on-board power. PIMT may in principle mitigate the impairments caused by the propagation of satellite signals throughout the atmosphere. They are adaptive communication systems that try and compensate in real time for tropospheric attenuation effects affecting the slant path by modifying for example the atenna pattern and the signal modulation and code.

In chapter 2 we focused on some system architectures that are exploited for PIMT: the Adaptive Code and Modulation, the Up Link Power Control and the Reconfigurable Antenna system. The critical design issues for these systems are represented by two different aspects: the design of the system margin and availability to be accounted to face the fading effects of rain and not rainy components and the adaptive resource management, i.e. the dynamic allocation of the resources according to the propagation channel condition. In this chapter we report a short overview of the main time series synthesizer developed in the last 10 years. These model have been compared into the ESA/ESTEC/Contract N°20887/06/NL/LvH and COST 280 action "Propagation Impairment Mitigation for Millimetre Wave Radio Systems" to resume the peculiarities of each synthesizer and to highlight the potential utility in the design and development of Propagation Impairment Mitigation Technique(PIMT). The main characteristics of

each model are presented and compared.

3.2 Time series synthesizer

Time-series synthesizers are models that reproduce the dynamic time varying channel by synthesis or by selection from database of measured data. The synthetic time series synthesized by these models focus on the production of different aspects and characteristics of the propagation channel as:

- The long-term CDF of attenuation;
- The fade slope and fade duration statistics;
- Scintillation characteristics;
- Eventually instantaneous frequency scaling characteristics;
- Depolarisation effects.

These models are of interest for PIMT in the design and operative phases, both for broadcasting or telecommunications satellite applications. These phases have to be carried out carefully and require precise information of the propagation channel and fading effects, not only in statistical terms. Indeed, the synthesizer allows the generation of the time varying condition of the channel and carefully characterizes the dynamic of attenuation that mimic the real measured time series. Therefore, in case of PIMT design they are useful for the development of new methodologies and for the study of control loop parameters. The control loop must, in fact, be able to track the signal fluctuation (fast and slow fluctuation) to mitigate the propagation impairments in real time by dynamically allocate the system resources. For the operational part, they are considered for the testing and validation of PIMT system.

In the past, experimental data have been used for the design and testing of PIMT techniques, but they are not world-wide available, therefore there is the need of a synthetic time series synthesizer that can reproduce the climatology of different locations and furthermore that can be adapted to different radio-link parameters.

In the following paragraph the most relevant time series synthesizers are briefly presented. We defined two macro categories: one devoted to the generation of the rain attenuation time series, the other one able to synthesize the time series of total attenuation. The latter category contains only the model provided by ONERA and defined in the Rec. ITU-R 1853-1n and the model that is presented in this thesis.

3.3 Rain attenuation time series synthesizers

3.3.1 Models based on the Maseng-Bakken model

3.3.1.1 ONERA-CNES spectral model

This model aims at synthesizing time series of rain attenuation [35]. It is a stochastic model which exploit the first order Markov theory presented by Maseng and Bakken [2]. They made two hypotheses for the rain attenuation process A_{Rain}:

- the long-term distribution of rain attenuation is log-normal, characterized by two parameters: the mean m and the standard deviation σ of log-attenuation;

- rain attenuation can be transformed into a first order stationary Markov process using the non linear transformation: $X = \frac{\ln A_{Rain} - m}{\sigma}$, where A_{Rain} is rain attenuation in dB.

Therefore, we need three input parameters: the log normal parameter m and σ and the β (s^{-1}) parameter that is used to describe the dynamic of rain attenuation. These parameters must be determined on a long-term basis, from local experimental data or from Recommendation ITU-R P.618. Furthermore, to correct the dynamic of the time series generated by the model, an additional parameter A_{offset} [dB] is introduced. This quantity is subtracted to the generated time series of rain attenuation to match the required probability of rain.

In Fig. 3.1 we report the block scheme of this model. The discrete white Gaussian noise $n(t)$ is low pass-filtered and transformed in a log normal distribution in a memoryless non-linear device and is calibrated to match the desired attenuation statistics with the A_{offset} parameter. The result of this process is the generation of the A_rain time series.

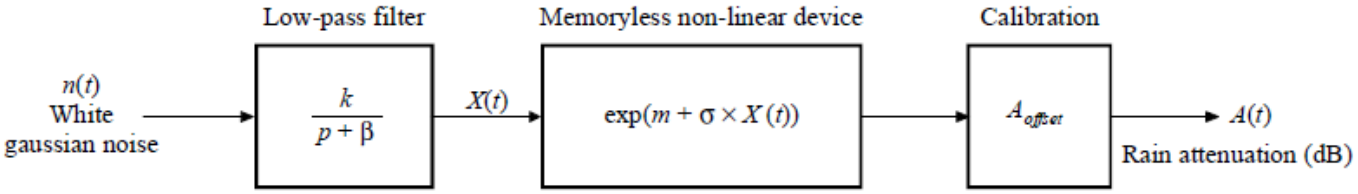

Figure 3.1: *Principle of the ONERA-CNES spectral model.*

Here we report the results of the first order statistic validation for this synthesizer. The model has been tested over four database of measurements:

- 7 years of measured rain attenuation events from the ITALSAT experiment in Spino D'Adda (SPI) for two frequencies (18.7 and 49.9 GHz) and the elevation angle of 37.7°

- 34 months of measured rain attenuation events from the OLYMPUS experiment in Louvain-la-neuve (LLN) for frequency of 30 GHz and the elevation angle of 27.6°

- 37 months of measured rain attenuation events from the OLYMPUS experiment in Lessive (LSV) for frequency of 20 GHz and the elevation angle of 27.8°

- 4 years of measured rain attenuation events from the ACTS experiment in CRC-Ottawa (SPI) for two frequencies (20 and 27 GHz) and the elevation angle of 30.3-32.6°

For each links 10 years of equivalent synthetic data have been generated. The resulting RMS fo the Co-Polar Attenuation are reported in Tab. 3.1 [35].

Table 3.1: *RMS error for attenuation CDF [%]*

	LLN @ 30 GHz	LSV @ 20 GHz	SPI @ 18.7 GHz	SPI @ 49.9 GHz	CRC @ 20 GHz	CRC @ 27 GHz
Onera model	19.7	21.1	18.0	21.4	24.3	22.1

3.3.2 Models based on statistical conditional probabilities

These models are based on the knowledge of the statistical conditional probabilities that the attenuation will be equal to a certain value at time $t+\Delta t$ knowing two previous attenuation values: A_0 at time t, and A_{-1} at time $t-\Delta t$.

3.3.2.1 Van de Kamp Two-samples model

The Van de Kamp model [3],[36],[37] returns a time series of rain attenuation for the desired location. The model predicts the probability distribution of rain attenuation a short time after a given value, depending on two previous samples of rain attenuation. This peculiarity allows the design and validation of the tracking loop of that system that exploit PIMT, since it helps identifying the speed of updating for the tracking loop.

The model is described as follows. The probability distribution $p(A)$ of attenuation A at time $t+\Delta t$ is dependent from A_0 at time t, and A_{-1} at time $t-\Delta t$ and is given by:

$$p(A) = \frac{m_A}{2A\sigma_A}\left(\frac{\pi m_A \ln(A/m_A)}{2\sigma_A}\right) \tag{3.1}$$

where m_A and σ_A are dependent on the two previous attenuation values A_0 and A_{-1}, as:

$$m_A = A_0\left(\frac{A_0}{A_{-1}}\right)^{\alpha_2} \tag{3.2}$$

and

$$\sigma_A = A_0\sqrt{\beta_2 \Delta t} + A_0\gamma_2(a - e^{-|ln(A_0/A_1)|}) \tag{3.3}$$

assuming a Δt=10 s. The parameters α_2,γ_2 and β_2 vary according to the considered location (as reference for the western Europe are: $\alpha_2 = 0.4$,$\gamma_2 = 0.43$ and $\beta_2 = 2x10^{-4}s^{-1}$) and can be derived from measured data. Furthermore, the model requires as input the maximum attenuation or the maximum duration of the rain fade event.

3.3.2.2 DLR channel model

The DLR channel model [4],[38] is an approach based on a mix of a Markov chain and Gaussian random variables. The model classifies the measured attenuation time-series into three types of signal segments:

- segments with almost constant received power, referred to as C, i.e. segments with a difference between two samples (spaced of approximately 1 minute) smaller than 1 dB;
- segments of decreasing received power, referred to as D, i.e. segments with a difference between two samples that is decreasing of a value bigger than 1 dB;
- segments of increasing received power, referred to as U, i.e. segments with a difference between two samples that is increasing of a value bigger than 1 dB.

Each sample type is characterized with the distributions of $P(y|x)$,i.e. the likelihood that the attenuation is y dB conditioned that $\Delta\tau$ (in the order of 1 minute) seconds before it has been x dB (determined over the full range of x with a step size of at most 0.2 dB to provide accurate results) [38]. An example of the distribution for summer and spring in proposed in Fig. 3.2.

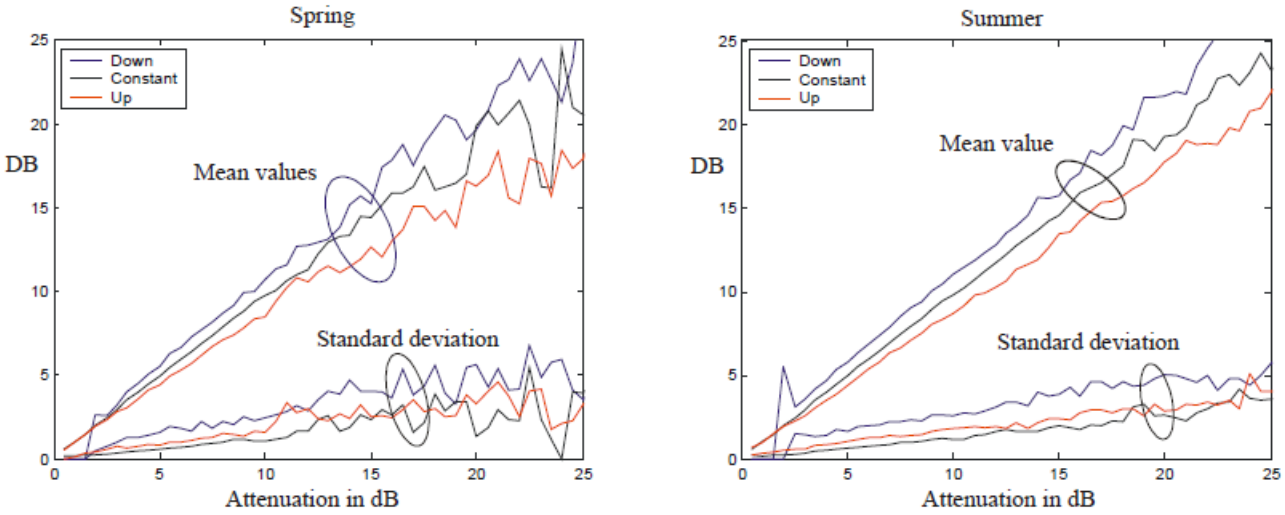

Figure 3.2: *Mean and standard deviation of the measured PDF of $P(y|x)$ for spring (left) and summer (right).*

The model provides the transition between the various types of signal segments depending on the outcome of a Gaussian random variable. Every new i^{th} outcome $a((i+1)T_s)$ of the channel model is the result of one single experiment of the Gaussian random variable with the mean value and standard deviation of the measured PDF of $P(y|x)$ where $x = a(iT_s)$ is the previous outcome of the channel model (with $T_s = \Delta\tau^{-1}$). The procedure is the following:

1. Calculate the type of signal segment $\Delta(iT_s)$ from the two previous outcomes $a(iT_s)$ and $a((i-1)T_s)$;
2. Determine the attenuation level of the previous outcome $x = a(iT_s)$;
3. Get mean value and standard deviation of random variable;
4. Carry out the new outcome $a((i+1)T_s)$ of the attenuation time-series.

This channel model requires as inputs the sets of mean values and standard deviations for $P(y|x)$. These sets can be obtained from experimental time series or should be taken from a location of the same climatic zone as the one used for the simulation.

3.3.3 Models based on Markov chains

3.3.3.1 2-states Markov chain model coupled to "Event-on-Demand" generator

This model is a new synthesizer obtained by associating the idea of a 2-states Markov chain model with an "Event-on-Demand" generator [5],[39],[40]. This model aims at

synthesizing time series of rain attenuation only. It is a cascade of two models: the first part called *macroscopic* model is based on 2-state Markov chain and a *microscopic* model based on the "on demand" procedure. The macroscopic model provides a time-series consisting of two possible states '1'(rain) and '0'(no rain, i.e. clear sky attenuation only). An example is shown in Fig. 3.3. The only parameter we need in input is the probability of rain attenuation (p_1) and the probability of transition from the rain to the no rain state (p_{10}). The microscopic model provides the rain attenuation events to be filled in into the coarse time series of rain/no rain intervals. The Lacoste-Carrie' model is a stochastic model that requires in input three parameters: the event duration D, the peak attenuation A_{max} and the temporal position of the maximum D_{peak}. Assuming a given value of D to obtain A_{max} and D_{peak} the system constructs an a priori structure as follows: generate bins of 5 minutes length containing experimental events with [A_{max},D_{peak}] and finally generates a matrix with pairs of [A_{max},D_{peak}] quantities. For each interval of length D of the macroscopic time series we choose the proper bin and the pair [A_{max},D_{peak}] is selected randomly.

To create each event, a stochastic interpolation based on the analytical expression of probability:

$$p(A(t)|A(t-\Delta t_1), A(t+\Delta t_2)) = \frac{p(A(t+\Delta t_2)|A(t))xP(a(t)|A(t-\Delta t_1))}{p(A(t+\Delta t_2)|A(t-\Delta t_1))} \quad (3.4)$$

assuming that $A(t)$ is a first order stationary Markov process and knowing $A(t-\Delta t_1)$ and $A(t+\Delta t_2)$. It can be proved [5] that this probability is log-normal with mean and standard deviation written as function of parameter m, σ and β. An example of the generated event is given in Fig. 3.4.

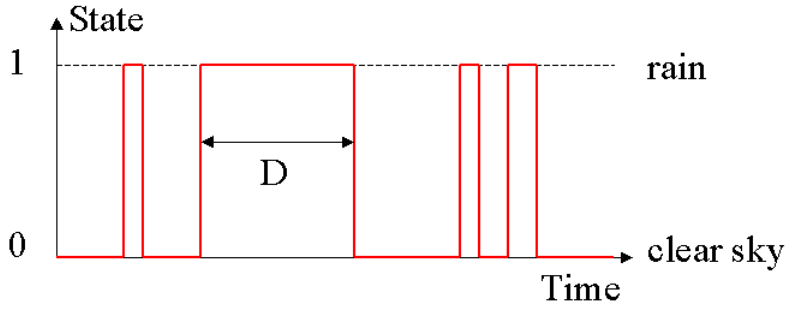

Figure 3.3: *Example of 2-state time series of rainy periods of time.*

3.3.4 Synthesis of rain rate series and conversion to attenuation

3.3.4.1 Synthetic Storm Technique

This model [6] is able to generate time series of attenuation, starting from the rain rate time series of rain storm, collected at a site with a rain gauge. The synthetic storm technique requires in input only the radiowave characteristics of the link (frequency, polarisation and elevation angle above 20°) and a database of measured rain rate for the site of interest (maximum integration time of 1 minute).

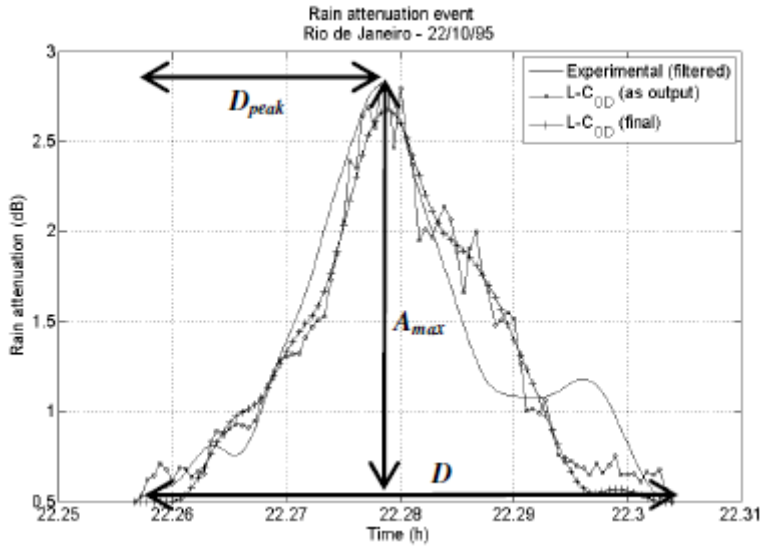

Figure 3.4: *Example of On demand generated event.*

The principle of the synthetic storm model is to convert the rain rate time series measured in a given site into a rain rate space series along a line, by using an estimate of the constant wind speed v (at 700-mbar level) to transform time to distance, through a convolution integral. In [41] it was shown that the statistical properties of rain attenuation derived from a large sample of rain rate time series agree fairly good with the measured rain attenuation, and that predictions are insensitive to the value of v.

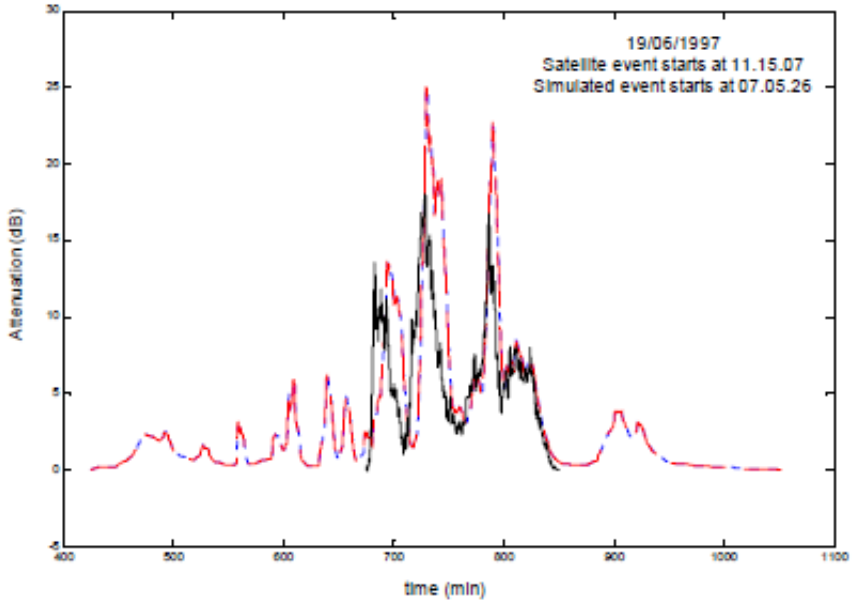

Figure 3.5: *An example of measured and predicted rain attenuation time series: measured data (black), 5 s time resolution (red) and 60 s time resolution (blue) [38].*

The model assumes a vertical structure of rain with two layers of precipitation of

different thickness: the first layer is rain (hydrometeors in the form of raindrops, water temperature of 20°C) with uniform rain-rate R (mm/h), while the second is the melting layer, i.e. melting hydrometeores at 0°C, with always uniform vertical precipitation rate given by $3.134R$. The height of the precipitation above sea level is assumed to be the ITU-R 0°C isotherm height above sea level (for a site in the Northern hemisphere at latitude $\phi \geq 23°$ is given by $5 - 0.075(\phi - 23)$ km). The depth of the melting layer is 0.4 km, regardless of the latitude. As far as rain attenuation is concerned, the two layers describe, on the average and effectively, all rain events made up of the two main types of precipitation, i.e. stratiform and convective. Rain attenuation, A (dB), is calculated as a line integral of the specific rain attenuation $Y = kR^{\alpha}$ (dB/km), according to the values of rain-rate found in the rain-rate space series obtained with the synthetic storm technique.

3.4 Total attenuation time series synthesizers

3.4.1 Tropospheric attenuation time series synthesizer (Rec. ITU-R P.1853-1)

The proposed model is the only synthesizer available today in the literature able to generate tropospheric components such as cloud, water vapor, oxygen and scintillation. The operative procedure is detailed in the Recommendations ITU-R P.1853-1 [1]. The synthesizer structure is depicted in Fig. 3.6 and the single components are considered as follows:

1. the rain attenuation is generated making use of the well defined ONERA-CNES spectral model presented in paragraph 3.3.1.1;
2. integrated liquid water contents (ILWC) is generated through a log-normal model and the clouds content is then translated into cloud attenuation with the Recommendation ITU-R P.840;
3. integrated water vapour content is modelled with a Weibull distribution and it is converted into attenuation based on Recommendation ITU-R P.676;
4. the oxygen attenuation, assumed as constant value, is computed starting from Recommendations ITU-R P.676 [8] and ITU-R P.1510 [42];
5. scintillation is assumed as a low pass filtered white Gaussian noise.

3.4.1.1 Rain attenuation time series

For the generation of rain attenuation time series the system exploits the ONERA-CNES spectral model previously defined and depicted in 3.1. The mean and standard deviation m and σ are derived from CDF of rain attenuation from local measured data or derived from Rec. ITU-R P. 618 [19]. The probability of rain P_0 is determined from Rec. ITU-R P.837 and the attenuation offset is assumed as $A_{offset} = e^{m+\sigma Q^{-1}(\frac{P_0}{100})}$.

3.4.1.2 Scintillation time series

The scintillation time series is obtained by filtering white Gaussian noise $n(t)$ with a low pass filter as shown in Fig. 3.7.

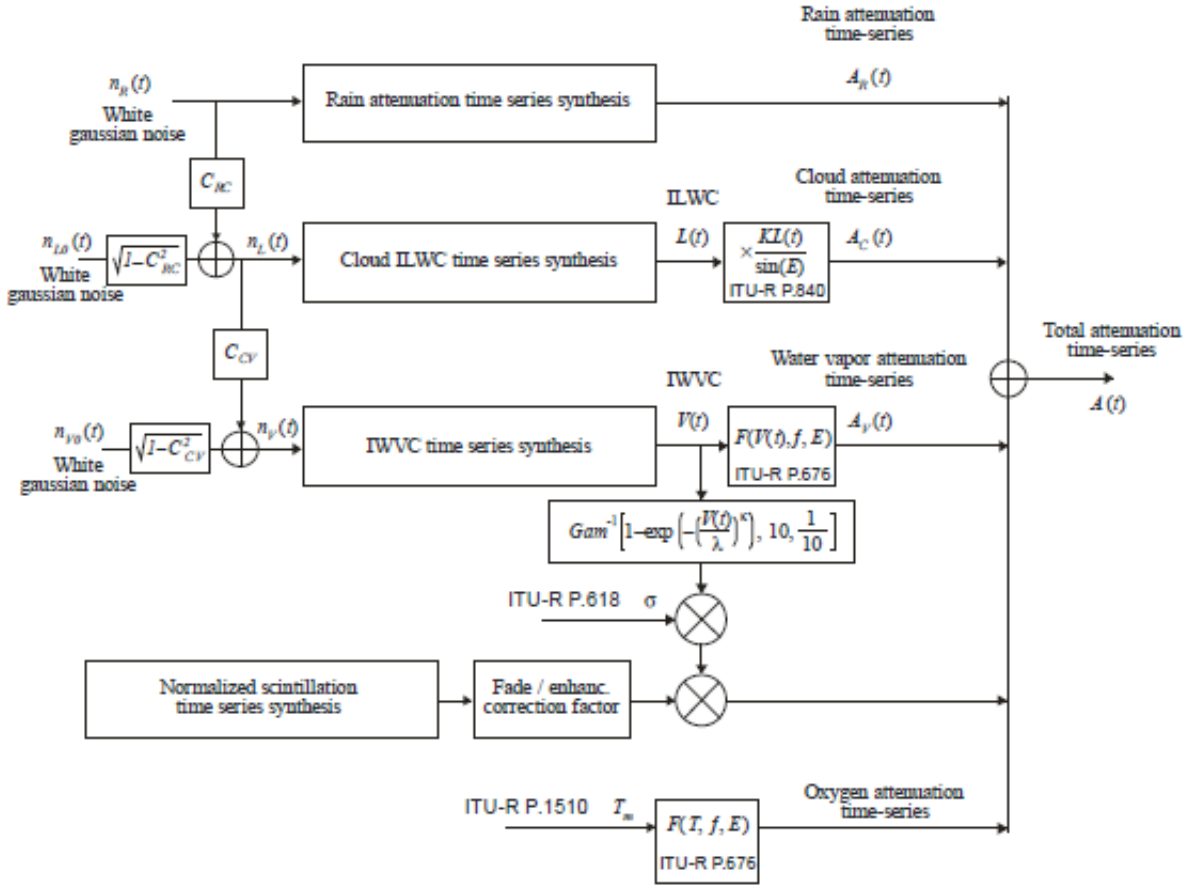

Figure 3.6: *Block scheme of the tropospheric attenuation time series synthesizer (Rec. ITU-R P.1853-1) [1].*

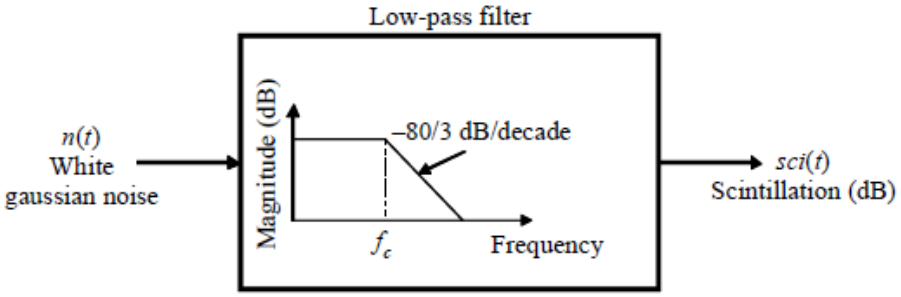

Figure 3.7: *Block scheme of scintillation time series synthesizer.*

3.4.1.3 Cloud attenuation time series

The statistic of the long-term integrated liquid water content (ILWC) is assumed to have a log-normal distribution. The time series is obtained by filtering white Gaussian noise $n(t)$ with a low pass filter, which is then truncated with the threshold α to match the probability of cloud occurrence P_{CLW} and transformed into a log-normal distribution with a memoryless non-linear device as shown in Fig. 3.8. The mean m and standard deviation σ and the probability of cloud occurrence P_{CLW} are derived from Rec. ITU-

R P.840. For the truncation threshold it is assumed $\alpha = Q^{-1}(P_{CLW})$ with the function Q defined in Rec. ITU-R P.1057. The low pass filter parameters are defined as: $\beta_1 = 7.17x10^{-4}(s^{-1})$, $\beta_2 = 2.01x10^{-5}(s^{-1})$, $\gamma_1 = 0.349$ and $\gamma_2 = 0.830$.

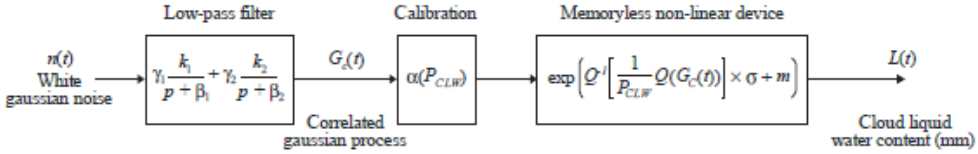

Figure 3.8: *Block scheme of liquid water time series synthesizer [1].*

The cloud liquid time series is interpolated in case the rain event is generated (A_{rain} >0 dB) and in case ILWC is higher than 1 mm (scattering condition).

3.4.1.4 Water vapor attenuation time series

The statistic of the long-term integrated water vapor content (IWVC) it is obtained with a Weibull distribution. The time series is synthesized with a white Gaussian noise $n(t)$ low pass filtered and transformed with memoryless non linear device into a Weibull distribution. The Weibull distribution parameters κ and λ are defined from the CDF of IWVC derived from local measurement data or, when not available with Rec. ITU-R P.836. The low pass filter parameter is $\beta_V = 3.24x10^{-6}(s^{-1})$.

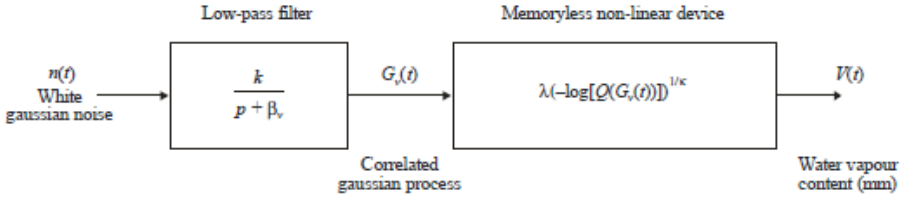

Figure 3.9: *Block scheme of water vapor time series synthesizer [1].*

3.4.1.5 Total attenuation time series

Total attenuation is computed as:

$$A(kT_s) = A_R(kT_s) + A_C(kT_s) + A_V(kT_s) + A_O + Sci(kT_s) \tag{3.5}$$

where k is the index of each sample and T_s is the time interval between consecutive samples.

An appropriate correlation (C_{RC}=1) is assumed between clouds and rain and the higher probability of occurrence of clouds with respect to rain probability guarantee to have rain events combined with clouds. A correlation coefficient C_{CV} between liquid water and water vapor has been arbitrarily set to 0.8.

This model is valid for earth-satellite system with a frequency range from 4 till 55 GHz and elevation angle between 5° and 90°.

CHAPTER 4

Liquid water and water vapor database

4.1 Introduction

In this chapter the retrieval procedure adopted for the extraction of Integrated Liquid Water Content (ILWC) and Integrated Water Vapor Content (IWVC) from the Brightness Temperature measured by a two-channel Microwave Radiometer (MWR) is presented. This procedure, based on the radiative transfer function of atmosphere, allows the determination of the ILWC and IWVC quantities making use of retrieval coefficients derived from radiosounding experiments (FERAS). The retrieved amount of ILWC is properly corrected by a "clear-sky correction procedure", which is able to reduce the error introduced by an improperly refined or infrequent calibration procedure. Then, once the time series of ILWC and IWVC quantities are obtained, we introduce a new procedure for the identification and removal of the embedded rainy periods. The proposed criterion for the detection of rainy periods is based on the intersection of three databases that detect different rain characteristics (rain rate, rain attenuation and Sky Status Indicator SSI).

Finally, to identify the proper criterion for the synthesis of ILWC and IWVC time series, the similarity in their annual, seasonal and daily trends are assessed. We observed a non marginal relationship between ILWC and IWVC processes and therefore we decide to maintain a connection in the generation of the ILWC and IWVC time series. In particular, we consider the daily basic time series as the time frame for the generation of synthetic time series.

4.2 Liquid water and water vapor content retrieval

Radiometers are wideband receivers able to detect the emitted sky radiation. These instruments are useful to estimate and evaluate the amount of Integrated Liquid Water

Content (ILWC) and Integrated Water Vapor Content (IWVC) present in the atmosphere. Two different retrieval procedures are present in literature: the site-dependent [43] and the site-independent [44] [45] procedure. The site-dependent procedure based on site-specific climatology, implies the use of radiosounding measurements combined with cloud detection algorithm to estimate the retrieval coefficients for liquid water and water vapor attenuation estimation. While, considering a site-independent procedure, we only need to know some ancillary information such as surface temperature, pressure and humidity to estimate the liquid water and water vapor quantities.

In this thesis we exploit a well known site-dependent procedure being available several years of radiosounding measurements collected by the Radiosonde Observations (RAOBS) FERAS Database provided by ESA.

4.2.1 Calculation of retrieval coefficients

The RAOBS FERAS Database is constituted by ten years (1980-1989) of vertical profiles of pressure, temperature and relative humidity detected at 0 and 12 UTC in non rainy conditions. The radiosounding measurements have been collected in 350 sites all over the world, and we assumed the Linate airport of Milano (45.26° N; 9.17° E) as reference site for the Spino d'Adda station. The vertical profiles are used as input to the Liebe "Microwave Propagation Model " MPM93 propagation model in order to derive the water vapor attenuation and to the Liebe MPM93 propagation model combined with the Salonen and Uppala cloud detection model to evaluate the cloud attenuation.

The Liebe MPM93 [10] is able to compute the atmospheric radio refractivity N of the main atmospheric components by taking as input certain meteorological variables. Considering the vertical profiles of pressure, temperature and relative humidity ,it evaluates the refractivity of non precipitating components as oxygen, water vapor and suspended water droplets at each layer of the atmosphere. The refractivity characterizes the response of a medium as ratio between the light speed in the vacuum and the speed in the medium, so it allows the estimation of the attenuation for all components. This model is reliable for frequency up to 1000 GHz.

The Salonen and Uppala model [16] is a cloud detection procedure that takes in input the radiosounding vertical profile to evaluate the liquid water density of the cloud necessary to the Liebe MPM93 to evaluate the total cloud attenuation. Furthermore, as will be shown later in this chapter, this model allows the calculation of clouds attenuation.

To perform the estimation of ILWC and IWVC we must evaluate the retrieval coefficients necessary for the inversion of brightness temperature. For each radiosounding, combining the Liebe MPM93 and Salonen-Uppala models, we are able to detect the exact value of ILWC and IWVC, the attenuation values of oxygen, water vapor and liquid water along the zenith and the mean radiating temperature. Furthermore, by a linear least-square fitting [43] of cloud attenuation against ILWC content and water vapor attenuation against IWVC content, the mass absorption coefficients a_V and a_L [dB/mm] are evaluated. In the following section the detailed procedure to estimate the retrieval coefficients is discussed.

4.2.1.1 Water vapor and cloud attenuation estimate

In the Liebe MPM93 model, the total path attenuation A_g [dB] due to oxygen and water vapor is derived as the integration of the specific attenuation γ_g [dB/km] dependent from the height z and the frequency f along the slant path at elevation angle θ and assuming that the atmosphere is horizontally homogeneous as:

$$A_g = \int_h^\infty \frac{\gamma_g(z,f)}{\sin(\Phi(z,\theta))} dz \tag{4.1}$$

where:

- $$\Phi(z,\theta) = \arccos[\frac{(r+h)n(h)cos(\theta)}{(r+z)n(z)}] \tag{4.2}$$
- r: Earth radius (6370 km);
- n: air refractivity index;
- h: station altitude;
- θ: elevation angle higher than 10°;

and with the specific gases attenuation [dB/km] defined as:

$$\gamma_g(z,f) = 0.1820 f N''(f) \tag{4.3}$$

where N'' is the frequency dependent absorption term of radio refractivity. The radio refractivity is a complex variable expressed as:

$$N = N_0 + N'(f) + jN''(f) \tag{4.4}$$

where N_0 is the non dispersive term, $N'(f)$ is the dispersive phase shifting term, and $N''(f)$ is the dispersive absorption term.

Similarly, in the Liebe MPM93 model the specific attenuation due to clouds is expressed as function of liquid water content as:

$$\gamma_c(z,f) = 0.1820 f N''_w(f) \tag{4.5}$$

with

$$N''_w(f) = \frac{9}{2} \frac{w}{\epsilon''(1+\eta^2)} \tag{4.6}$$

where

- w: liquid water content (g/m^3);
- $\eta = \frac{2+\epsilon'}{\epsilon''}$;
- ϵ': real part of permittivity of water;
- ϵ'': complex part of permittivity of water;

The complex permittivity of water is obtained with the double Debye model [10] as :

$$\epsilon(f) = \epsilon'(f) + j\epsilon''(f) \tag{4.7}$$

with

$$\epsilon'(f) = \epsilon_2 + \frac{(\epsilon_0 - \epsilon_1)}{1 + (f/f_D)^2} + \frac{(\epsilon_1 - \epsilon_2)}{1 + (f/f_S)^2} \tag{4.8}$$

$$\epsilon''(f) = \frac{f(\epsilon_0 - \epsilon_1)}{f_D[1 + (f/f_D)^2]} + \frac{f(\epsilon_1 - \epsilon_2)}{f_D[1 + (f/f_S)^2]} \tag{4.9}$$

where

- $\epsilon_0 = 77.67 + 103.3(\Theta - 1)$;
- ϵ_1 = 5.48;
- ϵ_2 = 3.51;
- $f_D = 20.09 - 142(\Theta - 1) + 294(\Theta - 1)^2$ [GHz];
- $f_S = 590 - 1500(\Theta - 1)$ [GHz];
- $\Theta = 300/T$ [1/K];

The liquid water content estimate is obtained applying the Salonen-Uppala model [16] as dependent on relative humidity, temperature and pressure profiles. The cloud detected in each pressure level is estimated according to a critical humidity as a function of the pressure level height [%]:

$$U_C(h) = 1 - \alpha \cdot \sigma(h)(1 - \sigma(h))[1 + \beta(\sigma(h) - 0.5)] \tag{4.10}$$

where

- α = 1;
- $\beta = \sqrt{3}$;
- $\sigma(h)$ is the ratio between the pressure at the level h and at the surface level;

The cloud presence is detected when the measured humidity is higher than the critical humidity evaluated at the same pressure level.

Then, when a level is assumed as cloudy, the liquid water content w [g/m^3] is expressed as function of the temperature as:

$$w = \begin{cases} w_0(1 + ct)(\frac{h_c}{h_r})p_w(t), & t \geq 0\ ^\circ\text{C} \\ w_0 e^{ct}(\frac{h_c}{h_r})p_w(t), & t < 0\ ^\circ\text{C} \end{cases} \tag{4.11}$$

where

- t = temperature [°C];
- h_c = height from the cloud base [m];
- w_0 = 0.17 [g/m^3];

- c = 0.04 [°C^{-}1];
- h_r = 1500 [m];
- $p_w(t)$ is the liquid water fraction that is approximated by the function:

$$p_w(t) = \begin{cases} 0, & t \leq -20\ ^\circ\text{C} \\ 1 + \frac{t}{20}, & -20 < t \leq 0\ ^\circ\text{C} \\ 1, & t > 0\ ^\circ\text{C} \end{cases} \tag{4.12}$$

Finally, the mass absorption coefficients $a_{V,f}$ and $a_{L,f}$ [dB/mm] at frequency f are derived by solving with a linear least-square fit the following equations:

$$A_{V,f} = a_{V,f} V \tag{4.13}$$

$$A_{L,f} = a_{L,f} L \tag{4.14}$$

with

- $A_{V,f}$ and $A_{L,f}$ total zenith attenuation due to water vapor and liquid water at frequency f [dB];
- $V = \int_0^\infty \rho_V(z)dz$ the integrated water vapor content [mm] with $\rho_V(z)$ water vapor content at height z [g/m^3];
- $L = \int_0^\infty \rho_L(z)dz$ the integrated liquid water content [mm] with $\rho_L(z)$ liquid water content at height z [g/m^3];

4.2.2 Retrieval procedure

The ILWC and IWVC can be accurately retrieved by the sky noise temperature evaluated by means of a two channel MWR. The frequencies of the MWR should be chosen such that one is more sensitive to the water vapor and the other one is more responsive to liquid water. The total zenith attenuation A_f [dB] derived by radiometer brightness temperature at frequency f is defined as:

$$A_f = 10 log_{10}(\frac{T_{mr} - T_c}{T_{mr} - T_{sky,\theta}}) \sin(\theta) \tag{4.15}$$

where

- T_{mr} is the mean radiating temperature which has a monthly and seasonal variation between 260 and 280 K [46];
- T_c is the cosmic temperature (equal to 2.73 K);
- θ is the elevation angle of the Satcom system;
- $T_{sky,\theta}$ is the sky noise temperature detected by the radiometer at the elevation angle θ.

Under the hypothesis of non-scattering condition (absence of rain) and in local thermodynamic equilibrium we can assume that the total attenuation detected by the MWR is composed by:

$$A_f = A_{O,f} + A_{V,f} + A_{L,f} \tag{4.16}$$

where

- $A_{O,f}$ is the zenith attenuation due to oxygen at frequency f;
- $A_{V,f}$ is the zenith attenuation due to Precipitable Water Vapor at frequency f;
- $A_{L,f}$ is the zenith attenuation due to Liquid Water Path at frequency f.

For a dual channel receiver at frequency f_1 and f_2 we can rewrite Eq. 4.16 as

$$\begin{cases} A_{f_1} = A_{O,f_1} + a_{V,f_1} V + a_{L,f_1} L \\ A_{f_2} = A_{O,f_2} + a_{V,f_2} V + a_{L,f_2} L \end{cases} \tag{4.17}$$

By inverting the system of equations 4.16 and knowing the retrieval coefficients $a_{V,f}$, $a_{L,f}$ and $A_{O,f}$ calculated through radiosounding measurements we retrieve the value of V and L as follows:

$$\begin{cases} V = a_0 + a_1 A_{f_1} + a_2 A_{f_2} \\ L = b_0 + b_1 A_{f_1} + b_2 A_{f_2} \end{cases} \tag{4.18}$$

where a_0 [mm],b_0 [mm],a_1 [mm/dB],b_1 [mm/dB],a_2 [mm/dB], and b_2 [mm/dB] are respectively defined as:

$$\begin{aligned} a_0 &= \frac{A_{O,f_2} a_{L,f_1} - A_{O,f_1} a_{L,f_2}}{D} \\ b_0 &= \frac{A_{O,f_1} a_{V,f_2} - A_{O,f_2} a_{V,f_1}}{D} \end{aligned} \tag{4.19}$$

$$\begin{aligned} a_1 &= \frac{a_{L,f_2}}{D} \\ b_1 &= \frac{-a_{V,f_2}}{D} \end{aligned} \tag{4.20}$$

$$\begin{aligned} a_2 &= \frac{-a_{L,f_1}}{D} \\ b_2 &= \frac{a_{V,f_1}}{D} \end{aligned} \tag{4.21}$$

with D [dB^2/mm^2]:

$$D = a_{V,f_1} a_{L,f_2} - a_{V,f_2} a_{L,f_1} \tag{4.22}$$

4.2.3 Clear-sky correction procedure

The accurate retrieval of ILWC represents an important condition for the meticulous study of cloud properties. It is not automatically ensured that an accurate measurement of sky noise temperature gives a careful retrieval of ILWC. There are several sources of errors in ILWC retrieval. First, the calibration of MWR that occur in a long term observation (calibration bias, drift) [47]. Afterwards, uncertainties can be introduced by the estimation of absorption coefficients of ILWC and IWVC, or random noise can

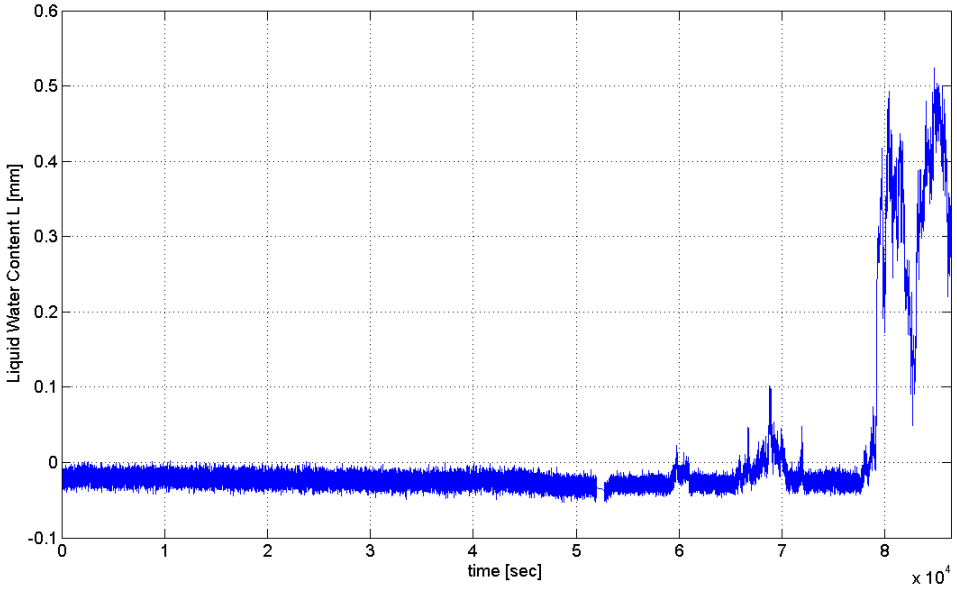

Figure 4.1: *An example of ILWC time series affected by calibration error.*

be produced by the system. An example of how the ILWC retrieval can be affected by these errors is shown in Fig. 4.1, where the lower values of ILWC are below zero.

The adoption of high-frequency channels (mm- and submm-wavelengths) in a traditional two channel MWR enhances the accuracy of low values of ILWC [48]. Furthermore, it has been proved that the employment of a Millimeter Cloud Radar (MMCR) helps in the improvement of ILWC retrieval [49]. Since the database used in our simulation is historical, we introduce the approach presented in [47], which exploits the clear-sky measurements (in absence of ILWC content) obtained by MWR as a reference for adjusting and recalibrating all ILWC measurements. The procedure is presented in the following.

Firstly, we evaluate the total attenuation A_f at the given radiometric frequencies as in Eq. 4.16 and we retrieve a first guess of ILWC and IWVC contents. We identify in the time series of retrieved ILWC the clear-sky periods, i.e. absence of ILWC, lasting at least one hour. The averaged value of total attenuation in each of these intervals A_{CLR} is assumed as the reference attenuation for the closest cloudy period. The value A_{CLR} at frequency f represents the sum of the contribution of oxygen, IWVC and ϵ_{CLR} which collects errors introduced by calibration and measurements uncertainties. Therefore, assuming the total attenuation time series during a cloudy period at frequency f we have:

$$A_f = A_{O,f} + A_{V,f} + A_{L,f} + \epsilon_f \tag{4.23}$$

where ϵ_f includes the uncertainties introduced by calibration and errors in measurements. The selected closest period of clear-sky condition can be expressed as:

$$A_{CLR,f} = A_{O,CLR,f} + A_{V,CLR,f} + \epsilon_{CLR,f} \tag{4.24}$$

By subtracting Eq. 4.24 to Eq. 4.23 we obtained:

$$\Delta A_f = A_f - A_{CLR,f} = [A_{O,f} - A_{O,CLR,f}] + [A_{V,f} - A_{V,CLR,f}] + A_{L,f} + [\epsilon_f - \epsilon_{CLR,f}] \tag{4.25}$$

The variation of oxygen and IWVC within a cloudy period can be assumed as sufficiently small then, Eq. 4.25 can be written as a single term dependent from IWVC variation and ILWC quantity:

$$\Delta A_f = \Delta A_{V,f} + A_{L,f} \tag{4.26}$$

For a two channel MWR, the retrieved ILWC is defined as:

$$L = b_1 \Delta A_{f_1} + b_2 \Delta A_{f_2} \tag{4.27}$$

where b_1 and b_2 previously defined in 4.20 and 4.21. In this formulation, the retrieval of ILWC is not dependent from IWVC retrieval anymore and is less sensitive from mass coefficient absorption uncertainties and MWR calibration.

An example of the effectiveness of the "clear-sky correction procedure" is illustrated in Fig. 4.2. In this figure, in blue is reported the time series of ILWC retrieved with original procedure illustrated in section 4.2.2. The same time frame is retrieved by performing the "clears-sky correction procedure" (red line). The new procedure ensures a better estimation of lower magnitude of ILWC, which are the range of value mainly affected by the calibration error.

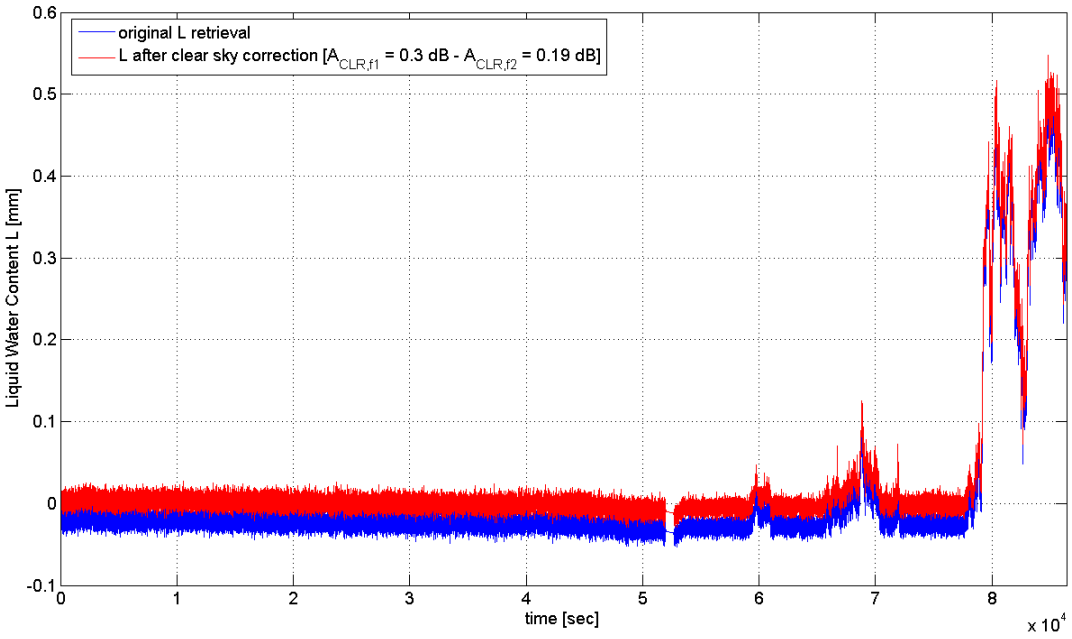

Figure 4.2: *Effects of clear-sky correction procedure on the retrieval of ILWC. In blue is reported the original value of L while in red is visible the correction of L values by means of the clear-sky correction procedure.*

To ensure a proper estimation of ILWC values, from this point forward, we will assume L_{min}=0.01 mm as the minimum ILWC value detectable by the MWR. Values below this threshold are assumed as zero.

4.3 Rain detection and removal

The retrieval of ILWC and IWVC is obtained on a large database (7 years from 1994 until 2000) of radiometric measurements collected by a two channel MWR at 23.8 and 31.6 GHz in Spino d'Adda for a slant path at 37.7° of elevation. The retrieval technique allows the determination of ILWC and IWVC quantities knowing the total attenuation (scaled from slant path to total zenith attenuation) at the two MWR frequencies, the retrieval coefficients and the medium temperature derived by radiosounding campaign. One critical step of this retrieval is represented by the identification, discrimination and interpolation of rainy periods in the time series of ILWC and IWVC. Indeed, when heavy rain is present on the slant path, the scattering effect introduced can cause severe alteration of the estimated total attenuation. The measured attenuation in this case is not dependent only on cloud and water vapor content, therefore the retrieval procedure is not applicable. The accurate identification of the time series of attenuation interested by rain is a demanding procedure. The risk is that, in presence of light rain, too many samples of clouds could be assumed as rainy and removed in favour of having larger percentage of rainy time. The proposed criteria for the detection of rainy samples is based on the intersection of three databases which collects data from three instruments: a raingauge, a beacon receiver and a MWR. Each one of these databases detects different rain characteristics.

Finally , the effects of rain interval detection and removal are assessed by evaluating the percentage of rain time and the single inter annual variability of CDF of ILWC and IWVC. We observe that the rainy samples removal procedure generates a time percentage of rain that is consistent with ITU-R [50] and furthermore, the CDF of ILWC and IWVC show good agreement with the reference CDF of ITU-R model.

4.3.1 Rain indicator and databases

We consider three different ancillary databases of co-located measured data:

- raingauge to detect rain rate (RR);
- beacon receiver to detect rain attenuation (AR);
- radiometer to evaluate the Sky Status Indicator (SSI).

Each of these databases refers to different aspects of a rain event, so the joint use ensured an effective tool to identify rainy periods. Indeed, while the raingauge provided information only of rain at the station, the beacon receiver and the SSI detected rain also along the slant path. Let us start considering separately each database focusing on their peculiarity.

The rain rate was measured by a raingauge located next to the MWR in Spino d'Adda [51]. The rain rate database collects 7 years (1994-2000) of rain rate measurements sampled each minute and has an availability close to 100% of time [52], so it is entirely reliable for our analysis. The raingauge detects only the rain event located in Spino, and not the slant path events.

The beacon receiver measured 7 years (1994-2000) of total attenuation at 18.7, 39.6 and 49.5 GHz along a slant path of 37.7° towards the ITALSAT satellite [52]. Since, to

extract the rain attenuation events, the zero dB level that identifies the clear-sky attenuation threshold in the beacon measurements is obtained by means of the radiometer outputs, the evaluation of rain attenuation could be biased and influenced by a possible error in the identification of the "non-rainy" threshold. In our analysis we have considered only recorded samples when no satellite outages and no measurement failures for any beacon occurred and therefore we identify for beacon measurements at 18.7 GHz an availability of 93.4% of time for 7 years of measurements [52].

The Sky Status Indicator (SSI) [53] [54] [55] [56] is an ancillary quantity extracted by two channel radiometric measurements. The principle behind this parameter is that brightness temperature values are related with the absorption property of the atmosphere, and consequently to the state of the atmosphere (clear-sky, cloudy or rainy conditions). To detect the scattering phenomenon along the radiometric path, a simple procedure considers the ratio between the brightness temperature detected at f_1=23.8 GHz and f_2=31.6 GHz frequency. The basic idea is that for clear-sky condition the relationship between the brightness temperature at two frequencies is linear (dependent only on oxygen and water vapor), while in presence of heavy clouds and rain it become strongly non-linear. Fig. 4.3(a) shows the linear relation between the brightness temperature at two frequencies in clear-sky condition while Fig. 4.3(b) shows the non linear dependence between the brightness temperature at two frequencies for different atmospheric conditions. The ratio between the brightness temperatures is defined as:

$$SSI = \frac{(T_{f2} - k_1)}{T_{f1}} \tag{4.28}$$

with T_f the brightness temperature at frequency f [GHz] and k_1 is a constant value that takes into account the water vapor contribution. The k_1 value is defined as the constant term of the intercept between brightness temperature at frequencies f_1 and f_2 in clear-sky condition (red curve of Fig. 4.3(a)) according to the equation:

$$T_{31.6} = k_0 T_{23.8} + k_1 \tag{4.29}$$

and therefore we derived k_1=9.19 and k_0=0.42.

The cumulative distribution function of SSI values over the 7 years of measurement reported in Fig. 4.4 shows three different areas with variable slopes. The change of slope indicates a modification in the meteorological condition. The SSI values below 0.4 indicates a clear-sky weather state while SSI values comprises between 0.4 and about 0.8 refer to a cloudy/heavy cloudy condition and finally SSI values higher than 0.8 are with higher probability referring to samples under rain. The transition area between two atmospheric states is not well defined, so the determination of a fixed threshold for identifying rainy samples represents a delicate procedure.

An example of the time series of SSI, rain rate and rain attenuation with the corresponding ILWC are depicted in Fig. 4.5.

The objective of this analysis is to find a simple methodology to identify the rainy periods within the time series of radiometric measurements. We can trust on raingauge measurements to detect only local rain intervals. To detect the rain on the slant path we decide to use SSI parameter instead of simply keeping into account the rain interval detected by the beacon receiver since it is less affected by outage time and it is not biased by the identification of the "0 dB level threshold". Furthermore, the SSI is derived only from radiometer measurements and therefore it would be useful to identify a

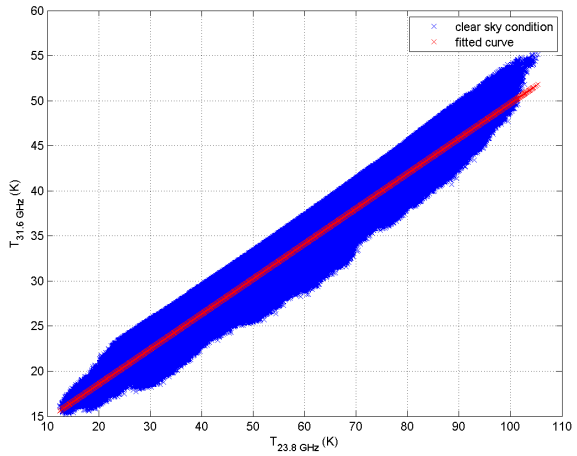

(a)

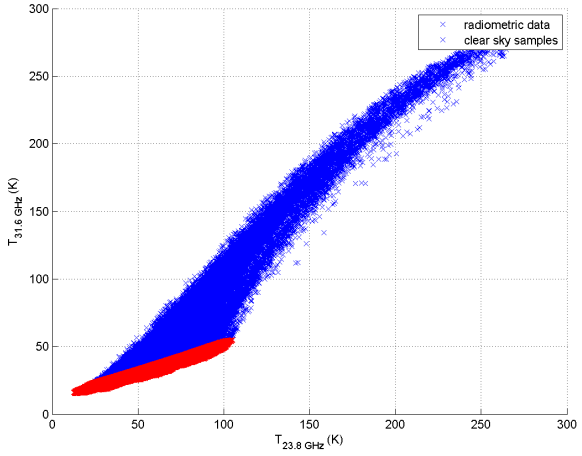

(b)

Figure 4.3: *Scatter plot of minute averaged samples of T_f at f_1=23.8 GHz and f_2=31.6 GHz for the years 1994 in clear-sky (a) and in different atmospheric conditions (b).*

threshold that can be applied to other experiments when beacon measurements are not available. Therefore we exploit the beacon measurements only to identify an appropriate threshold for the SSI parameter. In conclusion, we use the raingauge measurements and the SSI parameter to detect rain intervals.

4.3.2 Rainy intervals detection

The most important and difficult part of the combination of these three information is represented by the identification of the appropriate thresholds to detect the rain presence [57]. Indeed, each database collects a continuum of information (the beacon and radiometric measurements were sampled with a sampling frequency of 1 Hz, while for the raingauge were collected a sample each minute) that needed a threshold to identify which periods were affected by rain.

The thresholds are fixed to relative high values to ensure the effective presence of

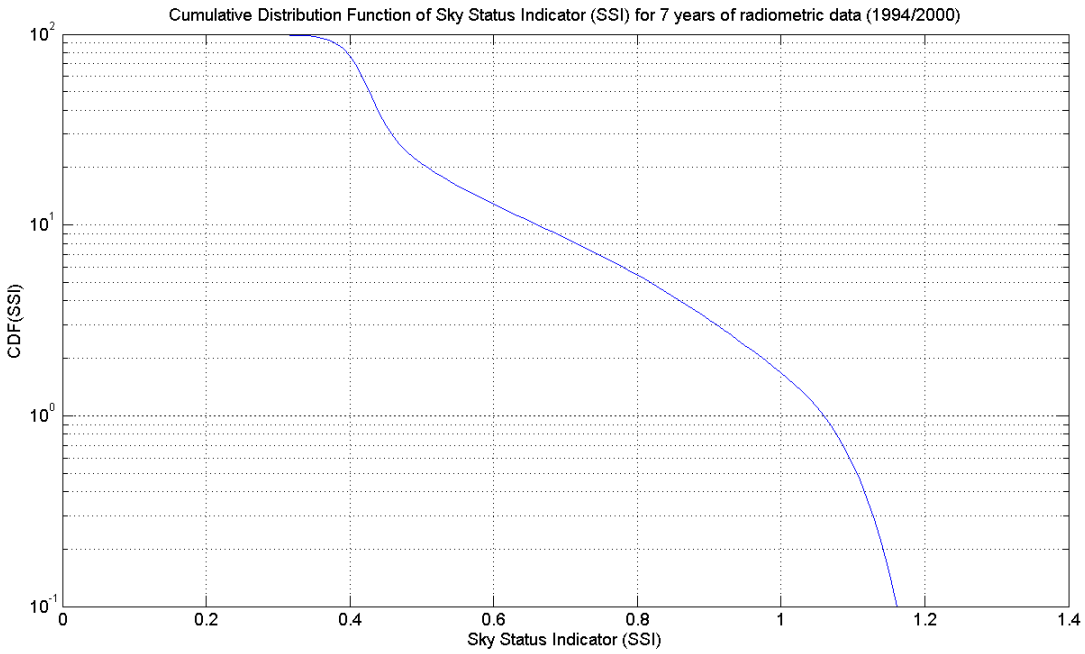

Figure 4.4: *Cumulative Distribution Function of Sky Status Indicator (SSI) values for 7 years (1994-2000) of radiometric measurements*

rain and to avoid uncertainties that are present before/after a rainy interval. We start considering the most appropriate threshold for SSI. Since we define the SSI threshold according to beacon database we assume $A_R > 0$ dB as threshold for rain attenuation. After having selected the time frames of rain attenuation (greater than 0 dB), we consider the values of SSI experienced during these periods. As shown in Fig. 4.6, we observe that 55 % of rainy periods have a SSI higher or equal than 0.87, that we assume as the threshold to identify rainy events in time series of radiometric measurements. Finally, we set up a fixed threshold for the rain rate database of $RR > 1$ mm/h. This value is adequately selective in the determination of rainy events since it cuts off the portion of time with very light rain.

An example of the detection of rainy samples for the raingauge and radiometric measurements are reported in Fig. 4.7. In Fig. 4.7(a) the Rain Rate is thresholded with the value $RR > 1$ mm/h, while in (b) the time series of SSI is thresholded with a value $SSI \geq 0.87$. The detected rainy samples in the two time series are almost coincident.

Then, the interpolation procedure takes place. When a sample is marked as rainy by at least one of these rain indicators (SSI or RR) the sample is defined as definitely interested by rain. The time series intervals that are labelled as rainy are interpolated according to the last sample before and first sample after the rainy period in order to retrieve the proper value of Liquid Water and Water Vapor Content. Moreover, there are some additional consideration to be pointed out. When an interval of consecutive rainy samples is shorter than 5 minutes, that samples are not considered as rainy. On the contrary if the non-rainy period between two rainy intervals is shorter than 10 minutes, all those samples are labelled as rainy. Furthermore, a daily time series is catalogued as rainy only if the longer rainy interval last more than 5 minutes.

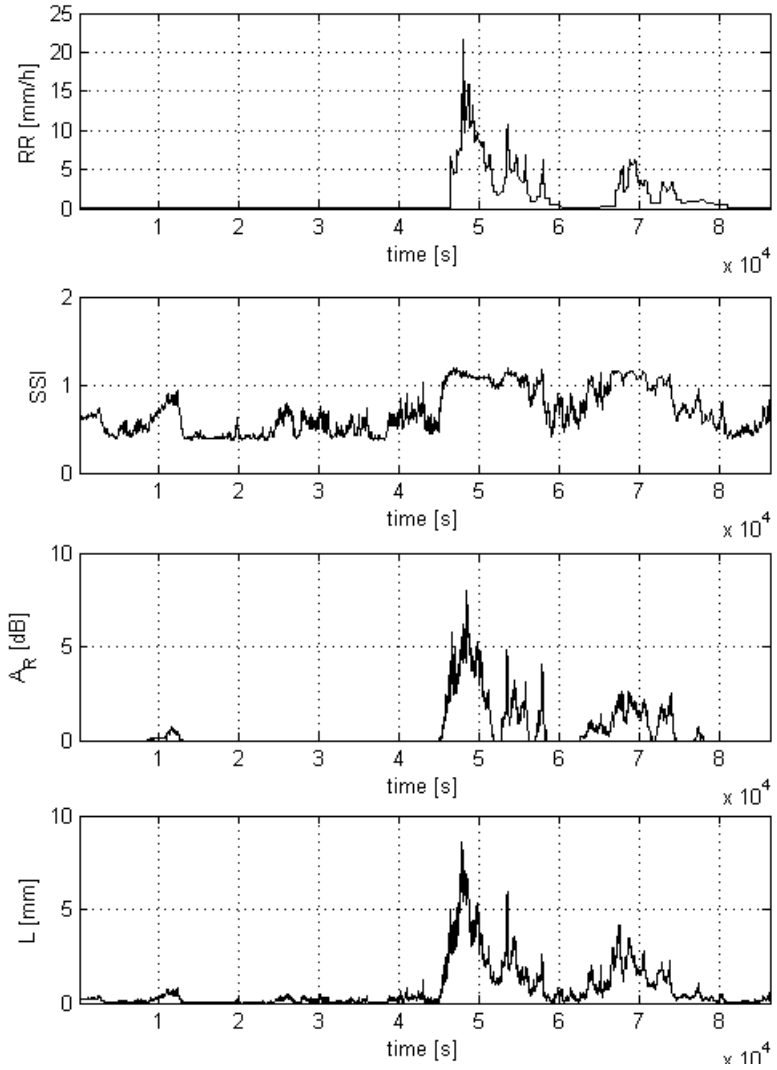

Figure 4.5: *An example of RR, SSI and A_R values excursion and ILWC variation for 07/01/1994.*

An example of the interpolation procedure for Liquid Water and Water Vapor Content is shown in Fig. 4.8 where in black are depicted the original contribution of water vapor (a) and clouds (b) and in magenta the contribution of interpolated values during rainy intervals. As shown in Fig. 4.8(a) the interpolation procedure erases the strong fluctuations of Water Vapor values present during rainy periods producing an almost constant value within rain event. In Fig. 4.8(b) the Liquid Water values increase drastically in presence of rainy events. The interpolation procedure removes the contribution due to rain drops during the rainy events while maintaining a plateau of clouds.

4.3.2.1 Rain time percentage probability

Once the rainy samples are properly detected, we can evaluate the percentage of time of rainy events of each year (P_0) for the raingauge (RR>1 mm/h), the SSI databases ($SSI \geq$0.87) and the resulting percentages evaluated considering the union of both SSI and RR (Tab. 4.1). From this table is evident the variability of the percentage time

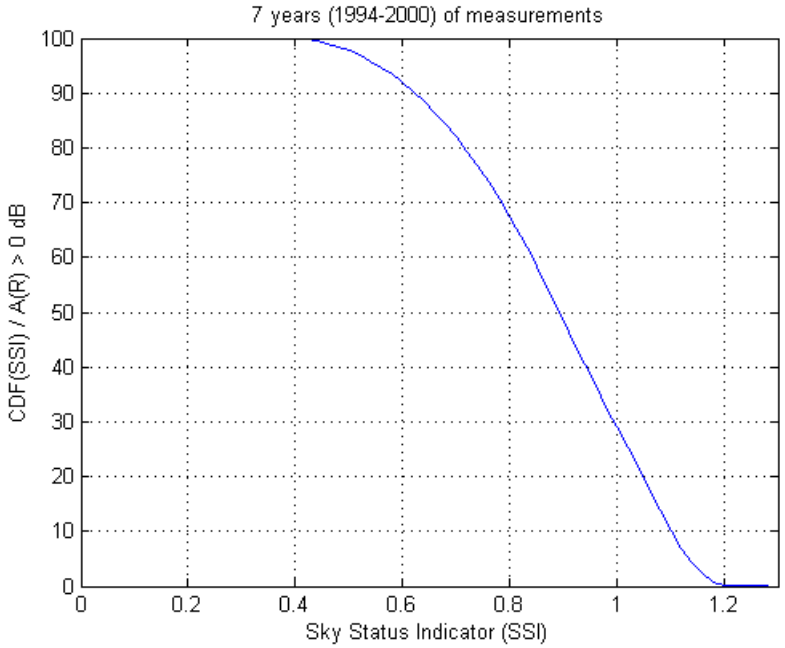

Figure 4.6: *Cumulative Distribution Function of Sky Status Indicator (SSI) values assumed within a rainy intervals detected by A_R>0 dB*

among different years that has an equal trend for both RR and SSI indicator, i.e. for example the minimum value occurs in the same year (1998). The averaged percentage of rain event detected for the entire period is consistent with per percentage determined with ITU-R [50].

Table 4.1: *Raingauge percentage of rainy time (P_0) detected assuming a rainy threshold of RR > 1 mm/h, percentage of rainy time (P_0) detected by Sky Status Indicator assuming a rainy threshold of $SSI \geq$0.87 and percentage of rainy time (P_0) detected by combined rain database with $SSI \geq$0.87 and RR > 1 mm/h.*

Year	1994	1995	1996	1997	1998	1999	2000	1994/2000
P_0 (RR > 1 mm/h)	2.30	1.85	3.24	1.76	1.12	2.29	2.65	2.17
P_0 ($SSI \geq$0.87)	3.63	3.44	4.03	3.17	2.79	3.80	4.96	3.69
$P_{0,rain}$	4.68	4.62	5.65	4.16	3.50	4.86	6.07	4.79

4.3.2.2 Annual variability

We consider the annual CDF of ILWC and IWVC in order to asses the annual variability of these processes after the interpolation of rain intervals. In Fig. 4.9 we report the comparison between CDF obtained from ITU-R models and the minute averaged CDF of ILWC and IWVC values for the database of 7 years (1994-2000) of radiometric measurements. We observed high similarities between the CDF curves referred to the same parameters. To assess the inter-annual variability of these quantities, we also report in Fig. 4.10 the single year CDF curves. As expected from the measurements, there is a significant inter-annual variability from one year to another. This fluctuation

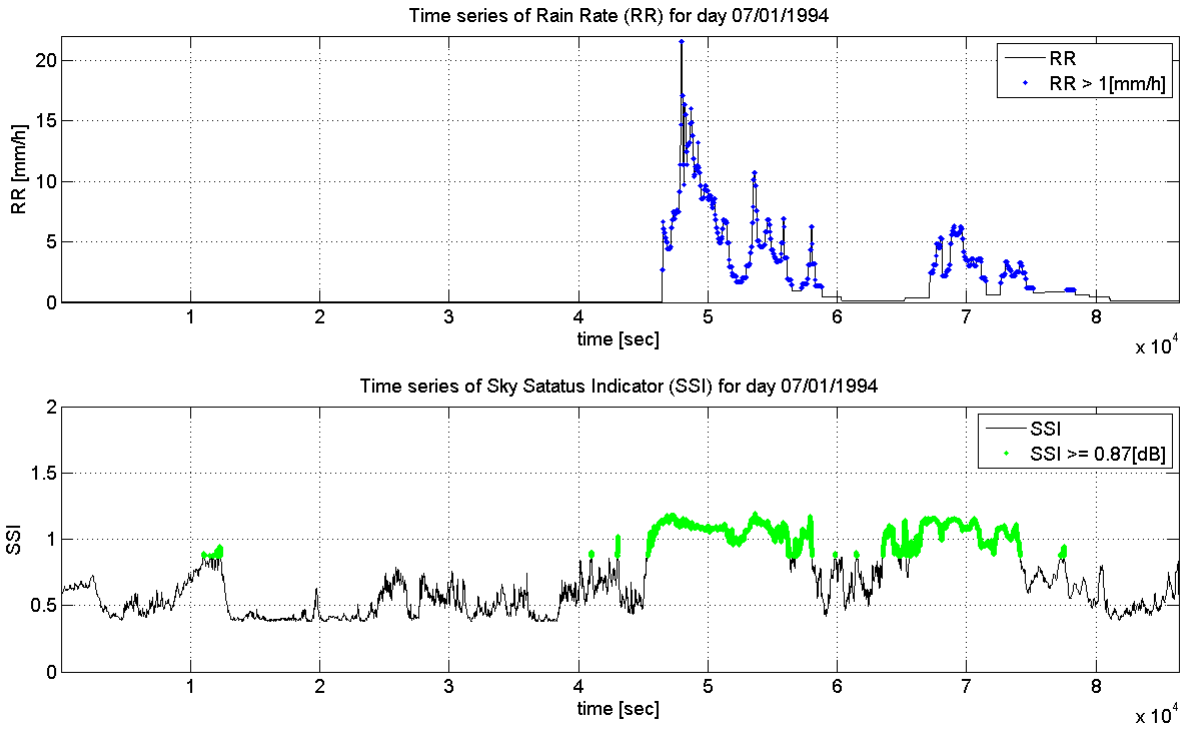

Figure 4.7: *An example of daily time series of Rain Rate (a) and Sky-Status Indicator (b) for 07/01/1994. In (a) the blue markers and in (b) the green markers identify the rainy samples in RR and SSI time series respectively.*

is evident in Tab. 4.2 where are reported the percentage of cloudy time $P_{L>0}$ in each year. The value calculated by the ITU-R model is compared with the measured yearly value of $P_{L>0}$. The averaged $P_{L>0}$ over the entire period of observation returns a value that is slightly larger than the ITU-R reference.

Table 4.2: *Percentage time of Liquid Water Content $P_{L>0}$ for 7 years (1994-2000) compared with ITUR reference value.*

Year	1994	1995	1996	1997	1998	1999	2000	1994/2000
$P_{L>0,Radiom}$ ($L>0$ mm)	55.55	49.22	52.54	51.01	49.75	58.68	53.01	52.82
$P_{L>0,ITUR}$ ($L>0$ mm)								48.86

4.4 Relationship between liquid water and water vapor content

Once the rain effects were properly removed, we focused on the Liquid Water and Water Vapor Contents. The objective of this part of the study is to observe the behaviour of Liquid Water and Water Vapor Content time series and to identify if there is a relationship between them. In case they cannot be considered disjoint, it is recommended to keep this connection during the synthesis of the two processes. Furthermore, we focused on the identification of a time frame, to be used as basic interval for the Liquid Water and Water Vapor time series generator. Therefore, we considered the possibility

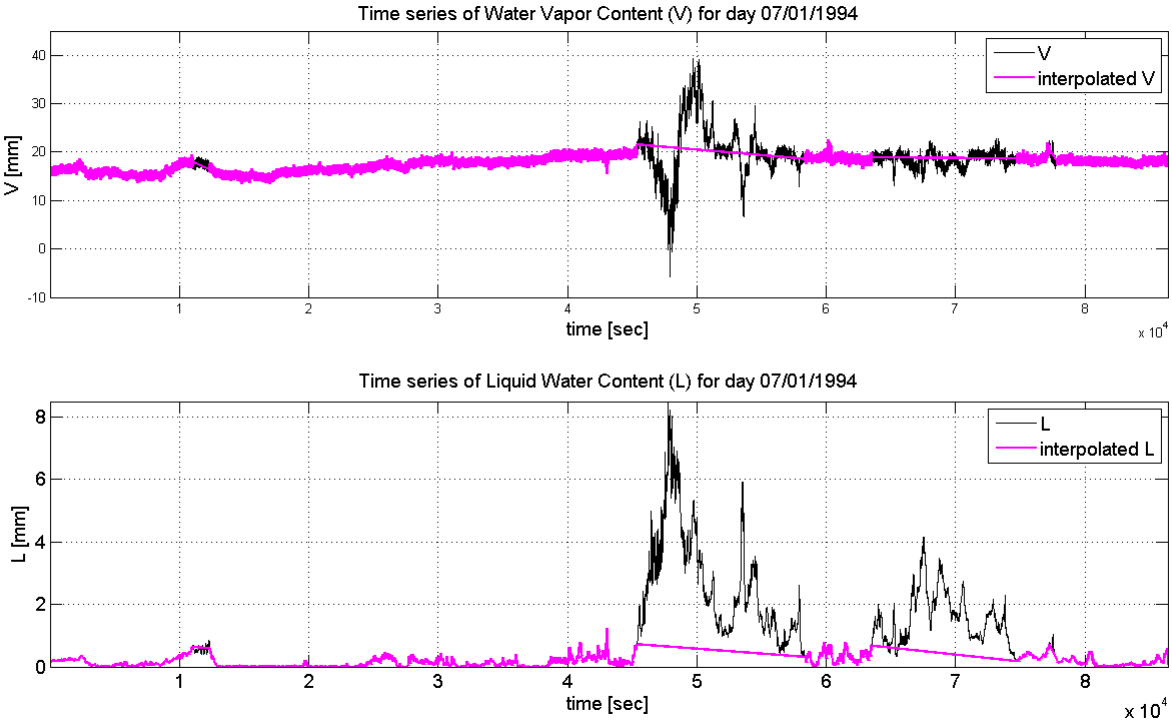

Figure 4.8: *An example of daily time series of Water Vapor (a) and Liquid Water (b) content for the 07/01/1994. The black curve represent the original values of V and L while in magenta are reported the interpolated values.*

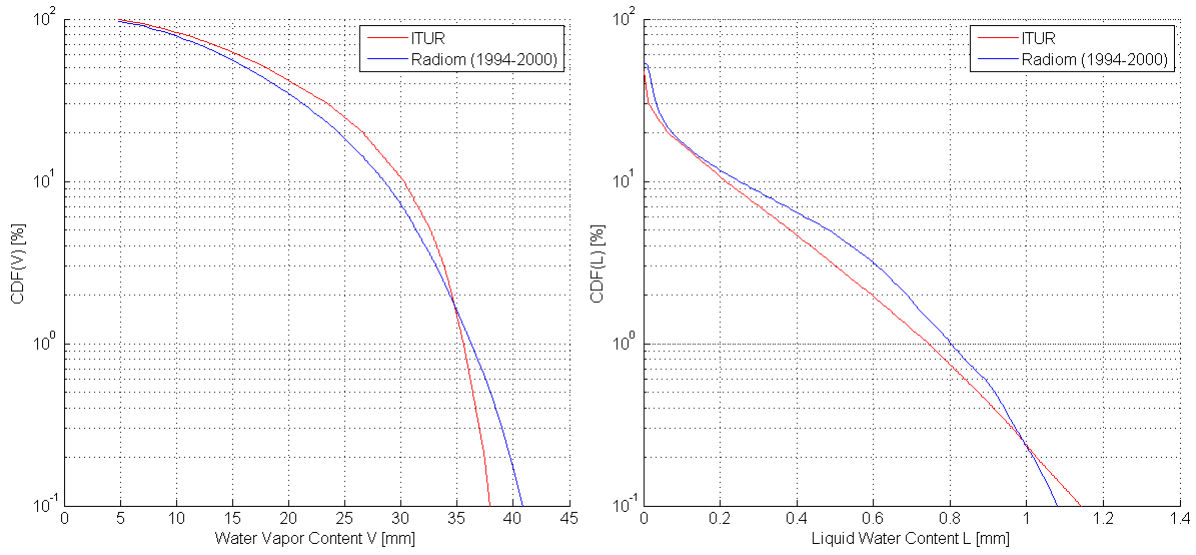

Figure 4.9: *Cumulative distribution function of Water Vapor Content (on the left) and Liquid Water Content (on the right) for the ITU-R models output (red line) and 7 years of radiometric measurements averaged over one minute (blue line).*

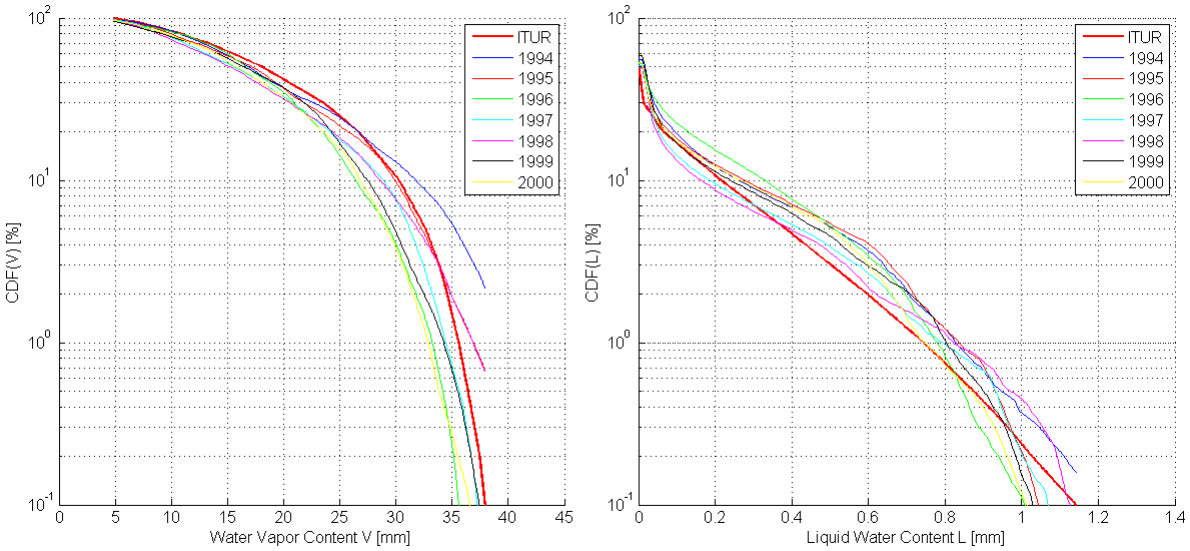

Figure 4.10: *Cumulative distribution function of single year of Water Vapor Content (on the left) and Liquid Water Content (on the right) for the ITU-R models output (red line) and 7 years of radiometric measurements averaged over one minute.*

of identifying a trend over the annual, seasonal and daily variation of time series in order to point out a possible common behaviour between these quantities.

For what concerns the behaviour of annual time series of ILWC and IWVC quantities, we were able to detect a significant annual trend of the daily average, minimum and maximum values of IWVC and of daily maximum value of ILWC. In Fig. 4.11 the trend of maximum (magenta markers), minimum (green markers) and averaged (blue markers) daily values of ILWC and IWVC for the year 1994 are reported. The higher values of ILWC and IWVC are experienced during summer: while the daily time series of IWVC have a marginal daily excursion, during summer the daily time series of ILWC observe the higher excursion between minimum and maximum values.

Furthermore, to highlight this tendency, we depicted the CDF of one minute averaged ILWC and IWVC values on a seasonal basis. In Fig. 4.12 it can be observed that the CDF curves of ILWC and IWVC show tendencies that vary noticeably from season to season. In Fig. 4.12 (a), winter (blue curves) and summer (red curves) CDF curves of IWVC are quite spaced one from the other, while spring (black curves) and autumn (green curves) are almost overlapped. In Fig. 4.12 (b), the winter and spring CDF of ILWC are almost overlapped in the lower range of ILWC (below 0.7 mm) while they diverge for higher values. In Fig. 4.12 (c), during summer the presence of clouds has a lower probability for ILWC values below 0.9 mm with respect to autumnal values, while after that threshold the trend inverts.

We focused on a possible synchronous variation on daily basis. We classified the daily time series according to the maximum daily values of ILWC and IWVC (L_{max} and V_{max}). In Tab. 4.3 and 4.4 are reported an example of the selected intervals of maximum values for ILWC and IWVC, where ten classes for each quantity are defined.

Then, we evaluate the percentage of the number of daily time series that satisfy simultaneously the conditions over ILWC and IWVC. In Tab. 4.5 and Fig. 4.13 we

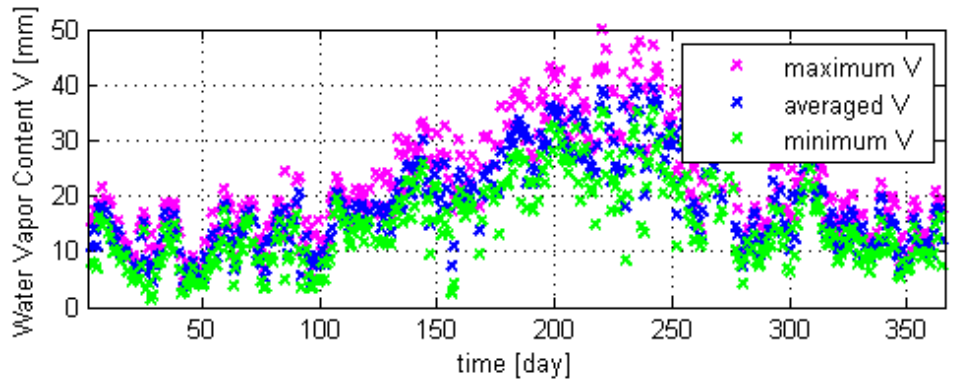

(a)

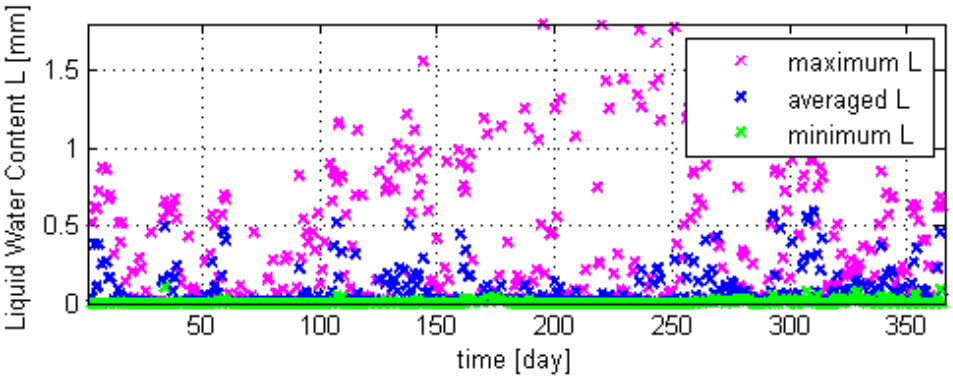

(b)

Figure 4.11: *An example of annual variation of daily minimum (green), averaged (blue) and maximum (magenta) values of Water Vapor Content (V) (a) and Liquid Water (L) (b) for the year 1994.*

Table 4.3: *An example of ten classes for the classification of daily time series of Liquid Water Content according to the maximum*

	L1	L2	L3	L4	L5	L6	L7	L8	L9	L10
L[mm]	L>1.4	1.2≤L<1.4	0.9≤L<1.2	0.6≤L<0.9	0.5≤L<0.6	0.3≤L<0.5	0.1≤L<0.3	0.05≤L<0.1	0.02≤L<0.05	0≤L<0.02

Table 4.4: *An example of ten classes for the classification of daily time series of Water Vapor Content according to the maximum*

	V1	V2	V3	V4	V5	V6	V7	V8	V9	V10
V [mm]	V>38	33≤V<38	27≤V<33	22≤V<27	19≤V<22	17≤V<19	14≤V<17	11≤V<14	8≤V<11	0≤V<8

shown the results obtained according to the classification proposed in Tab. 4.3 and 4.4. We found that, in the days where high values of L_{max} occur, there was a corresponding high value of V_{max}. In particular, for that classes which included the higher values of L_{max}, it was possible to identify a minimum value of V_{max} that was detectable for each class. Similarly, the days with low values of L_{max} are mainly interested by low values of V_{max}.

Therefore, considering the annual trends and the daily classification of Liquid Water and Water Vapor Content we recognized that these quantities could not be considered

Table 4.5: *Percentage probability [%] of database daily time series of ILWC and IWVC to simultaneously falls in a given class of ILWC and IWVC according to the classification proposed in Tab. 4.3 and 4.4*

	V>38	33≤V<38	27≤V<33	22≤V<27	19≤V<22	17≤V<19	14≤V<17	11≤V<14	8≤V<11	0≤V<8
L>1.4	0.8	0.8	0.6	0.1	0	0	0	0	0	0
1.2≤L<1.4	0.7	0.6	0.7	0.2	0	0	0	0	0	0
0.9≤L<1.2	0.6	2.6	4.0	1.8	0.4	0.1	0	0.1	0	0
0.6≤L<0.9	0.1	0.3	1.9	5.5	5.0	3.0	1.4	0.2	0	0
0.5≤L<0.6	0.1	0.3	0.3	0.6	0.5	1.2	3.0	0.8	0	0
0.3≤L<0.5	0.2	0.6	1.2	0.9	0.8	0.8	1.9	2.2	0.7	0.1
0.1≤L<0.3	0.4	1.2	2.3	2.1	1.4	1.4	2.5	2.6	1.7	0.5
0.05≤L<0.1	0.2	0.4	1.3	1.6	1.1	0.7	1.4	1.2	1.7	0.6
0.02≤L<0.05	0.1	0.4	2.2	2.2	1.7	1.1	1.4	1.6	1.3	0.9
0≤L<0.02	0	0.1	0.6	0.5	0.6	0.8	1.9	2.5	3.4	3.0

as completely independent. Thereby, this similarity is useful in the selection of the suitable time series of Liquid Water and Water Vapor Content for a simulator of total attenuation time series. As a matter of facts, it is not feasible to identify a general low to bound univocally a class of ILWC to a range of value of IWVC, but the synchronous variation of ILWC and IWVC during seasons and days suggests to maintain a daily synchronization. Therefore, we decide to consider the daily time frame of ILWC and IWVC as the basic time frame for the time series generator. Furthermore, during the cloud and water vapor time series generations we prefer to maintain a connection between ILWC and IWVC daily time series, instead of keeping separated the two synthesis procedures. The synchronous selection of daily time series of ILWC and IWVC would lead to a more realistic and reliable behaviour of the ILWC and IWVC synthesize time series.

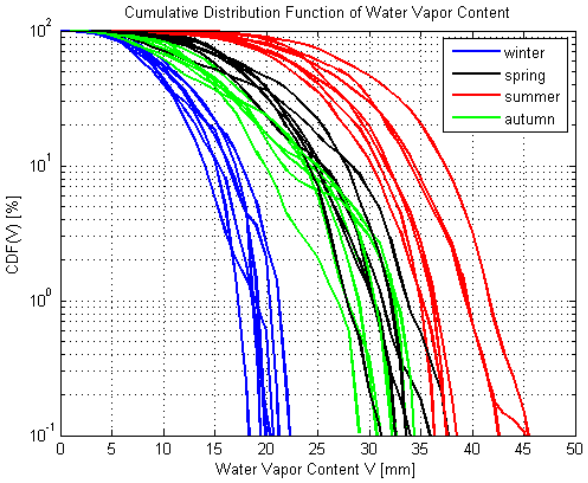

(a)

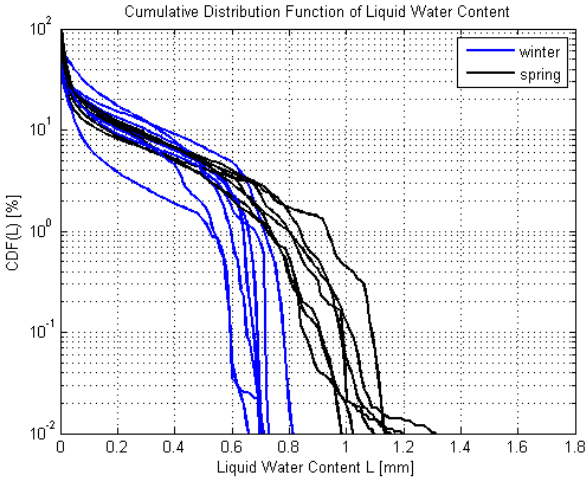

(b)

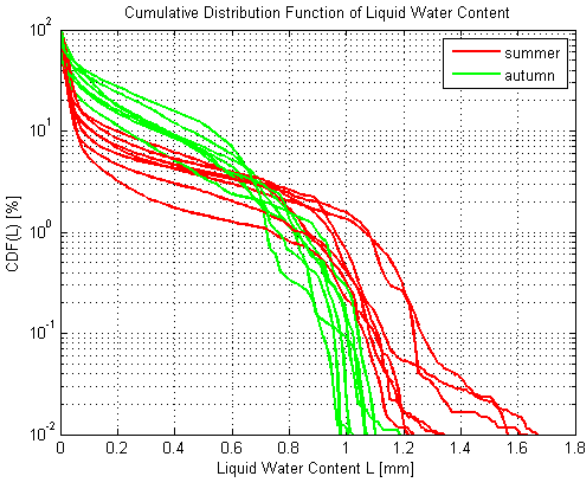

(c)

Figure 4.12: *Seasonal variation of CDF for minutes averaged value of Water Vapor (a) and Liquid Water Content for winter and spring (b), for summer and autumn (c) for the year 1994.*

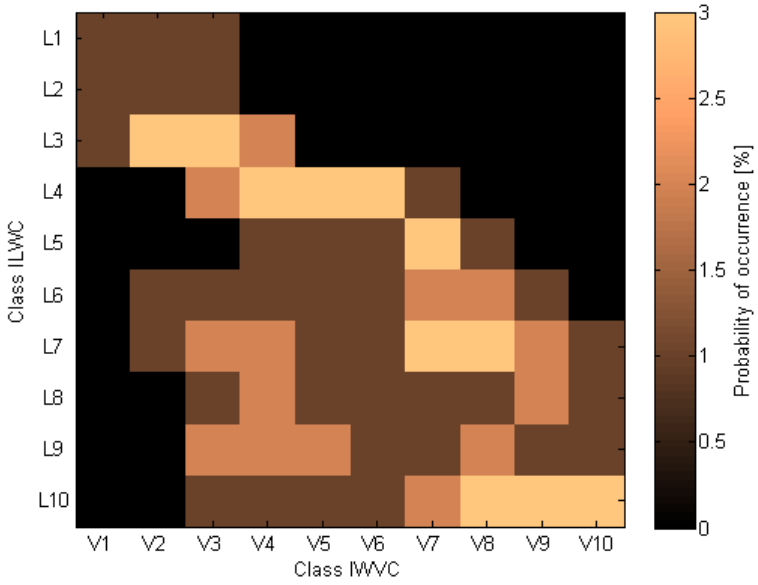

Figure 4.13: *Graphic representation of percentage probability [%] of database daily time series of ILWC and IWVC to simultaneously falls in a given class of ILWC and IWVC according to the classification proposed in Tab. 4.5.*

CHAPTER 5

Synthesis of liquid water and water vapor content time series

5.1 Introduction

In this chapter we focus on the core of Liquid Water and Water Vapor time series generation. As presented in the previous chapter, the original database of ILWC and IWVC measurements has been subdivided into fixed frames of daily time series with the purpose of maintaining the detected synchronous variation between these quantities. Furthermore, 24 hours length is sufficiently long to maintain the complete dynamic of an event of clouds and is adequately short to allow the flexible generation of several different synthetic time series of gasses and cloud components. We keep track of the date and timing of each time series, in order to be able to simultaneously select two "contemporary" (referring to the same day) time varying ILWC and IWVC processes.

An optimization procedure allows the selection of proper daily time series of ILWC and IWVC from the Radiometric Database (RADDB) to reproduce input statistics. The basic ideas behind this generator is that the database of 7 years of daily time series collected at Spino d'Adda has an adequate variability of events even to reproduce the long term statistics of ILWC and IWVC measured in a site with different latitude and longitude. Therefore, the input database is considered as neutral with respect to the site, and therefore the synchronous variation of ILWC and IWVC detected for Spino d'Adda is assumed as valid for other sites. For these reasons, when a new site is considered, the time series of ILWC and IWVC are scaled to better tune with the site-specific climatology, despite the trend of the ILWC and IWVC events is maintained almost unaltered.

Finally, after describing the time series synthesizer, the validation of the synthetic IWVC and ILWC time series is performed on statistical and on qualitative terms.

5.2 Structure of the time series generator

The generation of gasses and cloudy time series is a complex procedure that takes into account the long-term statistic of a given location and returns the time varying channel model of both ILWC and IWVC components. The objective of the time series generator is to reproduce the input statistic CDF function, called *objective function* (OBF), with a sequence of daily time series to build up a time series of a given time period (year or multi-year) length. The output is a *synthetic* time series of real measured data that tries to mimic the one really measured in a given location. In Fig. 5.1 a simple block scheme of the generation of the Liquid Water and Water Vapor Content is reported. The input OBFs, one for the Liquid Water and another one for the Water Vapor Content, can be provided in different ways (from measurement campaigns or from ITU-Recommendation models) and are assumed as targets in the time series generation. The synthesis of ILWC and IWVC time series is substantially performed with two parallel processes but the final solution is obtained choosing a subset of contemporary time series that satisfies the condition over ILWC and IWVC. Both time series of ILWC and IWVC are translated in attenuation quantities by multiplying for the mass absorption coefficients a_L and a_V expressed as a function of frequency and are scaled according to the selected elevation angle of the inclined satellite/earth path. The oxygen attenuation is considered a background effect with little temporal variations, therefore we assumed it as a constant.

The synthetic time series generation is achieved following three steps:

1. classification of input database of daily time series into classes: the classification of the RADDB into N classes is mandatory for the generation of a handy database for the selection of appropriate time series;

2. two "single variable optimizations" for ILWC and IWVC: two optimization are performed separately for the ILWC and IWVC quantities by reproducing the OBFs with the identification of the number of time series to be selected in each class of the input RADDB database;

3. "joint" selection of ILWC and IWVC time series: it ensures to extract from each class the number of daily time series evaluated by the single variable optimizations by selecting "contemporary" daily time series that satisfy both the condition of ILWC and IWVC (a procedure that preserves the RADDB synchronous variation).

5.2.1 Input database classification

The generation of daily time series and their classification for the input RADDB database is required only once for all. First, the time series of Liquid Water and Water Vapor are retrieved by radiometric measurements and the rainy periods are identified and removed with the procedure presented in section 4.3.2. Then, the ILWC and IWVC time series are subdivided into time frames of 24 hours. Once the entire database has been elaborated, the single time series are classified according to their maximum value of ILWC (L_{max}) and IWVC (V_{max}). We use the daily maximum of ILWC and IWVC to classify daily time series since it maintains the synchronous variation between ILWC and IWVC process shown in section 4.4. The interval's thresholds (L_j and V_i) are fixed

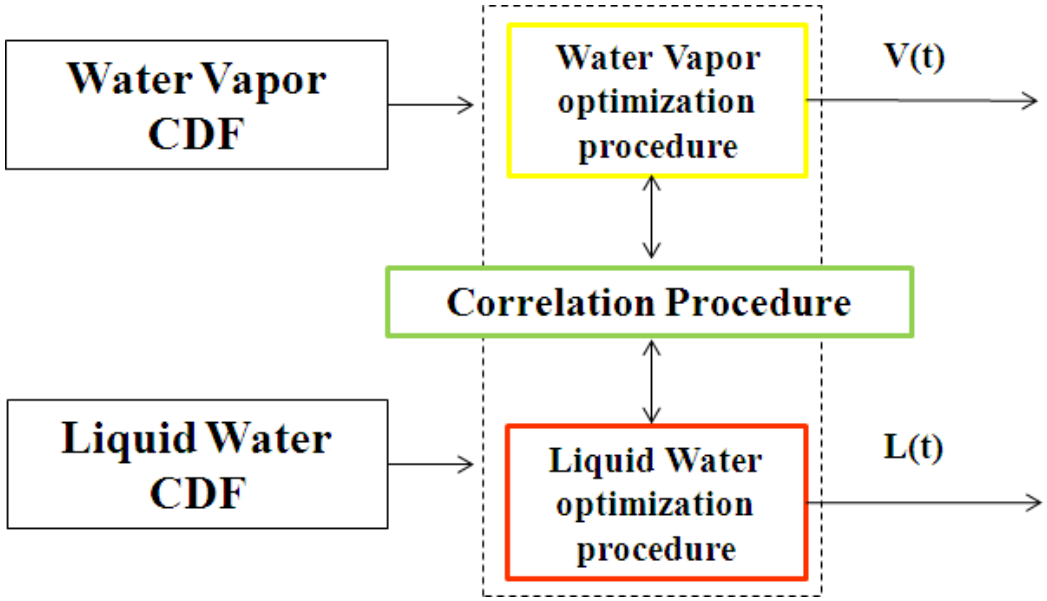

Figure 5.1: *General scheme of time series generator for clear-sky and cloudy attenuation components (Integrated Liquid Water and Water Vapor Content).*

once for all according to the distribution of the maximum values in the database (there must be a sufficient number of days within each class). The number of class for the ILWC and IWVC can be different according to the intra-class variability detected.

The assumed class thresholds and the number of classified time series for ILWC and IWVC are reported in Tab. 5.1 and Tab. 5.2, respectively. For ILWC we define 8 classes (from 0 to 1.8 mm) while for IWVC we considered 5 classes (from 0 to 50 mm). We observed that the database of Water Vapor can be characterize by a lower number of classes with respect to the Liquid Water. The number of classes cannot be arbitrarily increased in order to have a sufficient number of time series within each class. In Tab. 5.1 we observe that the time series with lower values of ILWC (class L_7 and L_8), represent almost one-third of the total. Fig. 5.2 shows the CDFs of each class. As clearly shown in these figures, the time series of each class cover a well defined interval of values that characterize that class.

The result of the classification is given in Fig. 5.3 and 5.4 where all the time series of the RADDB are reported according to the classification of Tab. 5.1 and Tab. 5.2, respectively. These figures show clearly that, while for IWVC the classification according to the maximum daily values corresponds also to a classification of the daily averaged values, for the ILWC time series it does not occur.

Finally, a classification of both ILWC and IWVC time series is performed to allow a "joint selection". Each daily time series is located into a grid of L_j and V_i intervals according to the daily L_{max} and V_{max} maximum. In each box of Tab. 5.3 we report the number of daily time series that fall into the intervals defined by L_j and V_i. The result of this coordinate classification is required to perform the joint optimization of ILWC and IWVC.

Table 5.1: *Eight classes thresholds L_j for the classification of daily time series of Integrated Liquid Water Content according to the maximum*

	L [mm]	N° daily time series
L_1	L>1.2	109
L_2	0.9≤L<1.2	236
L_3	0.6≤L<0.9	422
L_4	0.4≤L<0.6	289
L_5	0.2≤L<0.4	267
L_6	0.1≤L<0.2	247
L_7	0.05≤L<0.1	254
L_8	0≤L<0.05	632
TOT_L		2456

Table 5.2: *Five classes thresholds V_i for the classification of daily time series of Integrated Water Vapor Content according to the maximum*

	V [mm]	N° daily time series
V_1	V>38	77
V_2	27≤V<38	559
V_3	20≤V<27	543
V_4	11≤V<20	940
V_5	0≤V<11	337
TOT_V		2456

Table 5.3: *Number of daily time series of ILWC and IWVC that simultaneously falls in a given class of ILWC and IWVC according to the classification proposed in Tab. 5.1 and 5.2*

	L [mm]	V_1	V_2	V_3	V_4	V_5	TOT_L
V [mm]		V>38	27≤V<38	20≤V<27	11≤V<20	0≤V<11	
L_1	L>1.2	35	65	9	0	0	109
L_2	0.9≤L<1.2	14	166	49	7	0	236
L_3	0.6≤L<0.9	1	53	206	162	0	422
L_4	0.4≤L<0.6	5	35	39	202	8	289
L_5	0.2≤L<0.4	8	56	48	123	32	267
L_6	0.1≤L<0.2	7	56	44	106	34	247
L_7	0.05≤L<0.1	5	50	53	92	54	254
L_8	0≤L<0.05	2	78	95	248	209	632
TOT_V		77	559	543	940	337	2456

5.2.2 Scaling input liquid water and water vapor content database

As already stated, in the generation of synthetic water vapor and cloud time series, the RADDB collected at Spino d'Adda is used under the assumption that it is representative for the characterization of the synchronous variation of Liquid Water and Water Vapor

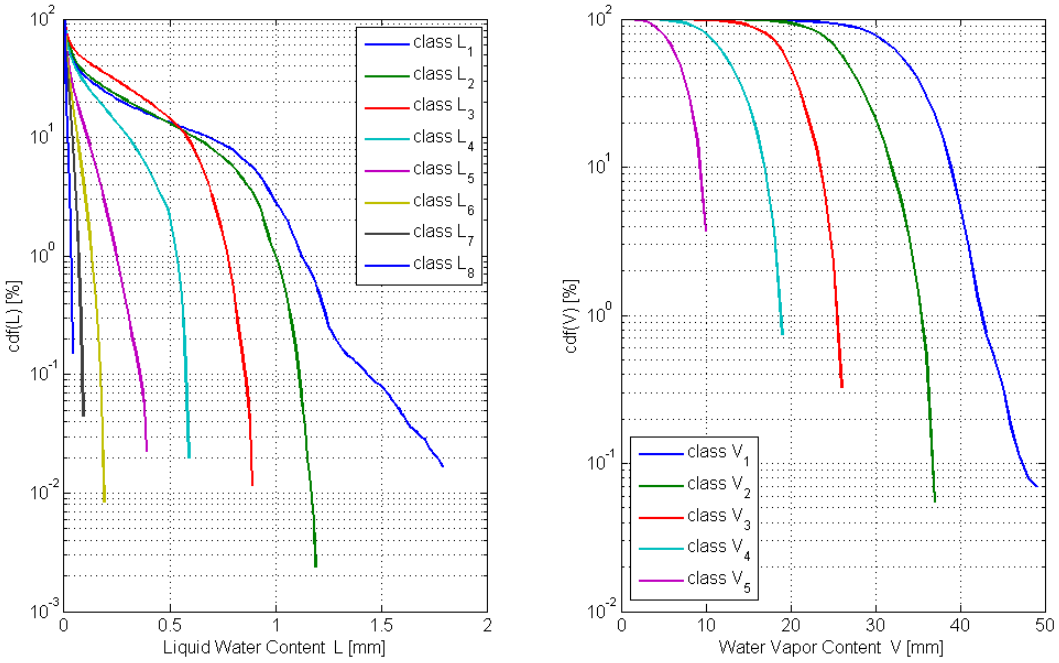

Figure 5.2: *Liquid Water Cumulative Distribution Function and Water Vapor Cumulative Distribution Function after the classification*

Content in any location. However, to adapt the range of values contained in the RADDB to the local climatology (represented by the objective function), we introduce a Scaling Factor SF to be applied to the entire database. The scaling procedure is adopted to the RADDB (Radiometric Database) only to ensure the presence in the database of daily time series with the required peak of ILWC and IWVC to correctly rebuilt the input OBF. After this elaboration, the hypothesis of synchronous variation of Liquid Water and Water Vapor Content is maintained unaltered. Indeed, the only modification is observed in the absolute values contained in the database but not in the "shape" of ILWC events and in the time series of IWVC associated at the same day.

The Scaling Factor SF is defined as:

$$SF_L = \frac{P(L)_{OBF}(p)}{P(L)_{RADDB}(p)} \tag{5.1}$$

$$SF_V = \frac{P(V)_{OBF}(p)}{P(V)_{RADDB}(p)} \tag{5.2}$$

where $P(L)_{OBF}$ and $P(V)_{OBF}$ are the OBF $P(L)_{RADDB}$ and $P(V)_{RADDB}$ are the CDF function of the input databases at probability value $p = 0.1\%$. The ILWC and IWVC time series in the database are scaled with SF_L and SF_V to ensure a better agreement with local climatology. We assumed the probability level $p = 0.1\%$ since, in case we consider as OBF the ITU-R models, the range of probability is comprised between 0.1 % and 99 % for both ILWC and IWVC and therefore it is most appropriate probability level to ensure the synthesis of higher ILWC and IWVC values. Furthermore, in case

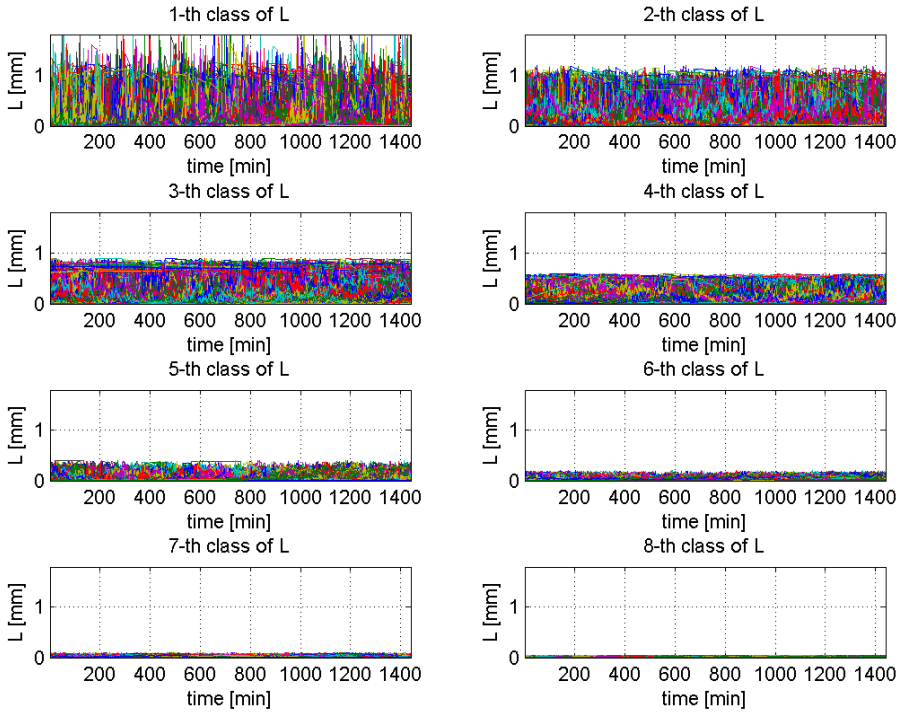

Figure 5.3: *Liquid Water time series classification according to the class thresholds reported in Tab. 5.1*

the OBF is derived from RAOBS database, we hardly can rely on values with probability below the $p = 0.1\%$ level, and therefore the scaling of whole RADDB database on this range of values could compromise all the synthesis. For this reason, we maintain the same threshold both for ILWC and for IWVC.

This procedure is applied to ILWC time series only if:

$$\frac{P(L)_{OBF}(p) - P(L)_{RADDB}(p)}{P(L)_{RADDB}(p)} > 10\% \tag{5.3}$$

and to IWVC time series only if:

$$\frac{P(V)_{OBF}(p) - P(V)_{RADDB}(p)}{P(V)_{RADDB}(p)} > 10\% \tag{5.4}$$

with $p = 0.1\%$. The effects of the scaling procedure are depicted in Fig. 5.5 for the city of Oslo. In red are reported the $P(L)_{RADDB}$ and $P(V)_{RADDB}$ CDFs calculated by the original RADDB and in black the OBFs of Oslo. For this location we evaluate the scaling factors are SF_L =1.3047 and SF_V =0.8554. After applying the Scaling Factors, the input RADDB is modified and the scaled CDFs are given by the blue curves.

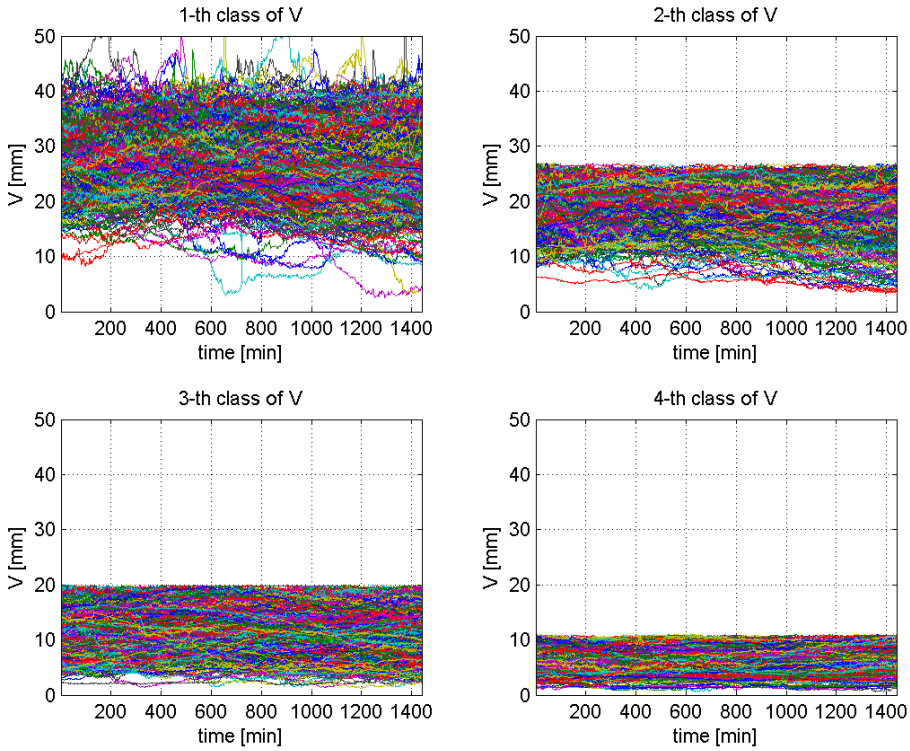

Figure 5.4: *Water Vapor time series classification according to the class thresholds reported in Tab. 5.2*

5.2.3 Single variable optimization procedure

The generation of time series of Liquid Water and Water Vapor is performed starting from two distinct optimizations carried out in parallel. As previously defined, the goal of the optimization procedure is to identify a proper number of time series to be selected from each class of the RADDB in order to reconstruct the OBF. In Fig. 5.6 we show a simple flow chart of the basic operations. Each optimization process takes as input the OBF and the RADDB with classified time series (M classes for the ILWC and N classes for IWVC database). If required, the scaling procedure is then applied. The algorithm derives a set of CDF curves, called *base functions* (BF), one for each j^{th} class of the ILWC database ($P(L)_j$) and for each i^{th} class of the IWVC database ($P(V)_i$). Finally, the "single variable optimization" procedure starts. The OBF and the BF are sampled in regular ILWC(IWVC) steps. The selected points of OBF are approximated with a curve (*result CDF* REF) build up by summing together all the BF appropriately weighted. Therefore, during the optimization procedure, the system tries to reproduce each single point of the OBF with a curve that derives from the combination of all the BF of the classes adequately weighted, so that each point of the result curve derives from the contribution of all the classes. As follows, the BF are summed up and weighted in order to obtain the same probability of the OBF for each abscissa value (IWVC and ILWC). In Fig. 5.7 an example of the contribution of each BF to the reconstruction of the input objective function is depicted. Each optimization returns as output a vector of weights that determines how much each class contributes to the reconstruction of the

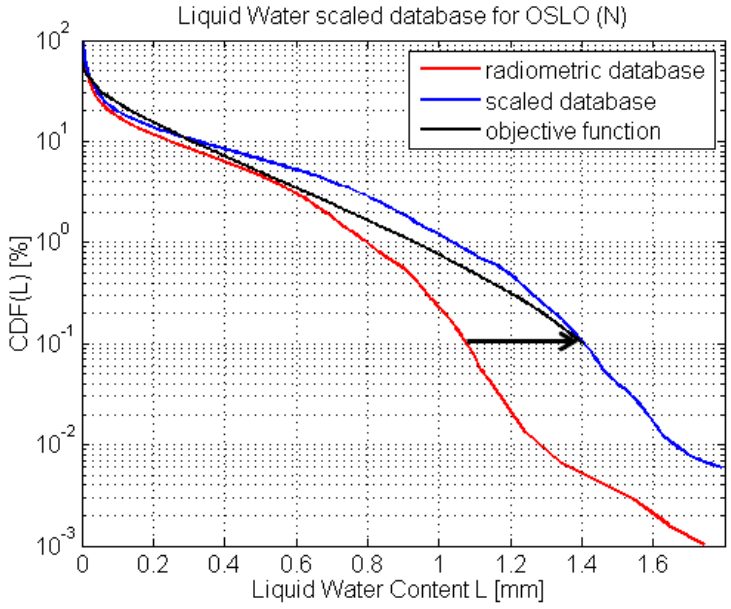

(a)

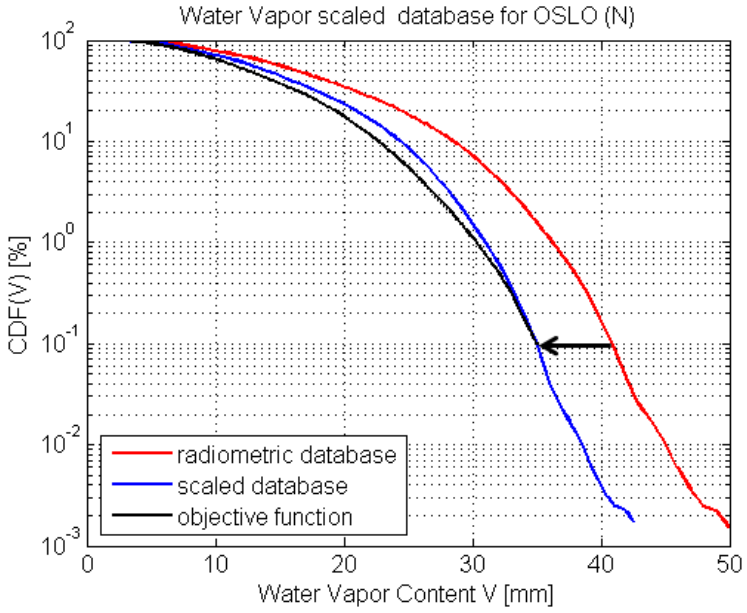

(b)

Figure 5.5: *An example of scaling of $P(L)_{RADDB}$ database (a) and of scaling of $P(V)_{RADDB}$ Database (b) for the city of OSLO (N)*

OBF.

Let us consider the optimization for the Liquid Water Content (the Water Vapor optimization requires an analogous procedure). Let's define the result function of ILWC

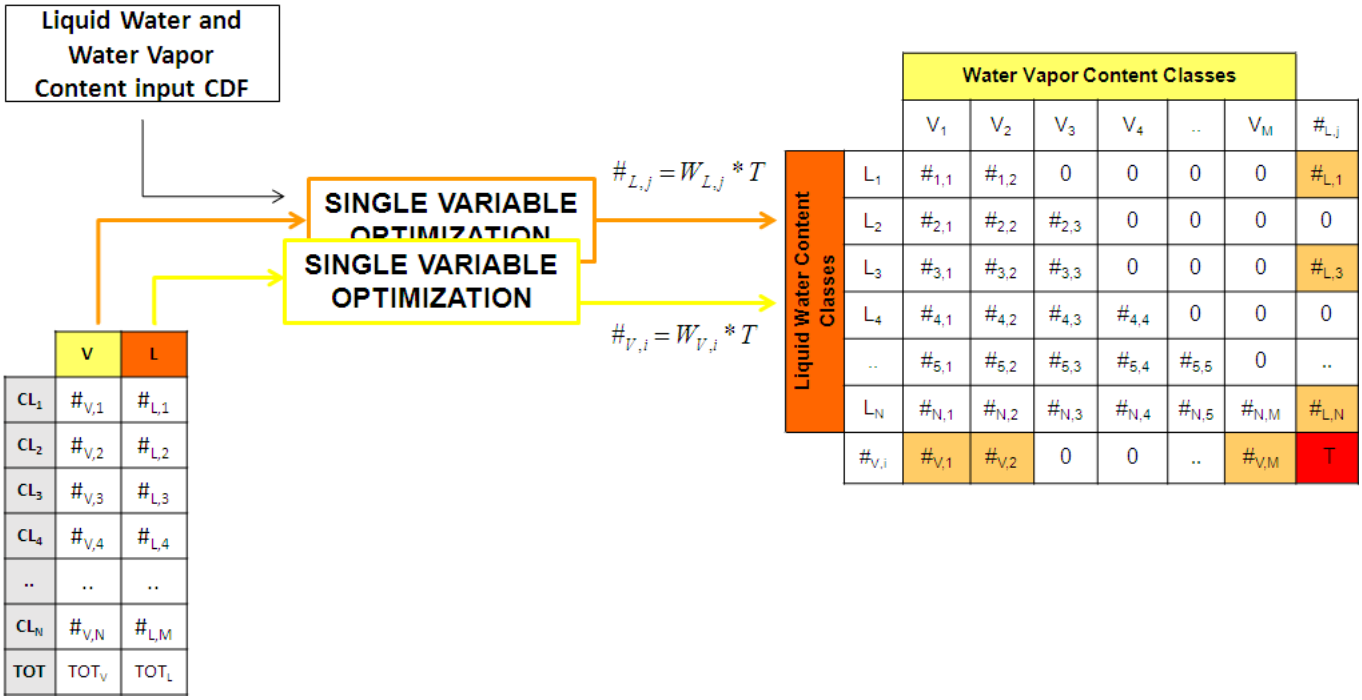

Figure 5.6: *Single variable optimization block scheme*

as the sum of the BF weighted by the coefficients W_j, as follow:

$$P(L)_{REF} = \sum_{j=1}^{M} W_j P(L)_j \tag{5.5}$$

Each weight is forced to be positive and minor than 1. The base function of each class is expressed in percentage probability, such that i.e. for the IWVC database the probability of having $V > 0$ mm is 100%.

A Mean Squared Error (MSE) optimization allows to minimize the distance between the OBF and the REF of ILWC. The distance, expressed as function of the weights W_j, is defined as follow:

$$d(W_j) = P(L)_{OBF} - P(L)_{REF} = P(L)_{OBF} - \sum_{j=1}^{M} W_j P(L)_j \tag{5.6}$$

assuming as a constraint that:

$$\sum_{j=1}^{M} W_j = 1 \tag{5.7}$$

Finally, the optimized set of weights is translated into a given number of daily time series to be selected from each class in order to obtain a time series of length T which reproduces the long term statistic OBF taken as input. So the number of selected days for the j^{th} class is defined as:

$$\#_{L,j} = W_j * T \tag{5.8}$$

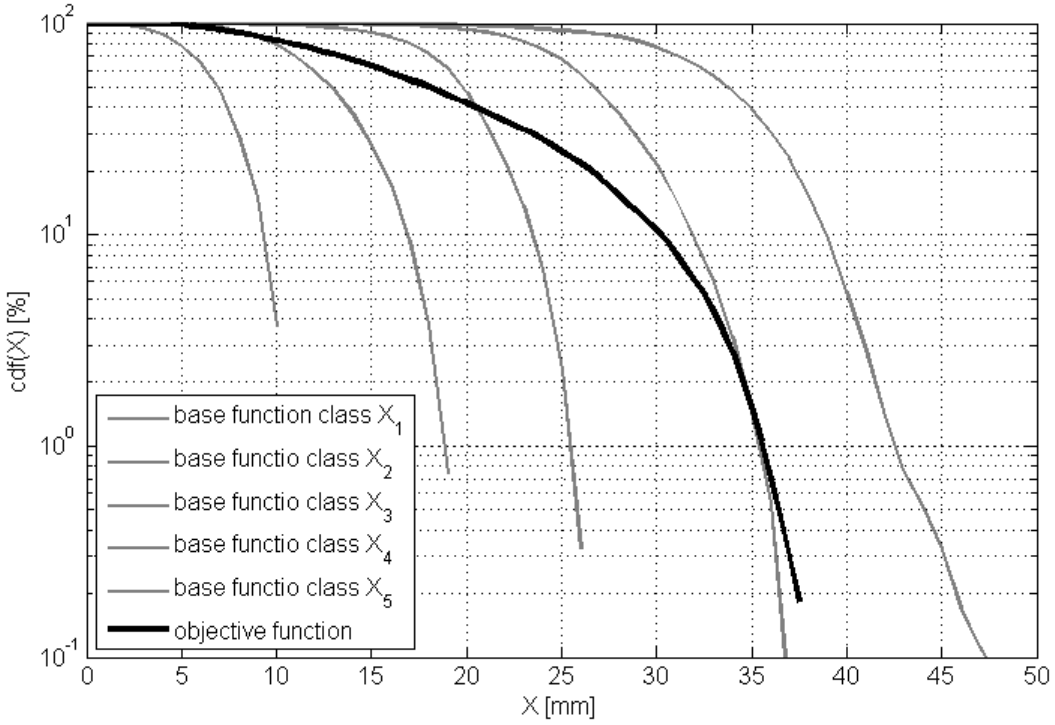

Figure 5.7: *Reconstruction of objective function by means of base function of variable X*

where T is the total number of days to be reproduced. The algorithm force the number of selected days to sum at T. Similarly, the single optimization procedure of IWVC returns a vector of $\#_{V,i}$ values which indicates the number of time series to be selected from the i^{th} class of the IWVC database. It is essential to underline that the two vectors $\#_{L,j}$ and $\#_{V,i}$ contain the solutions of two independent optimizations, therefore in Fig. 5.6 we highlight the solutions in the last column and row of the joint classification matrix. The vectors of weights represent the constraints, or requests, to be satisfied during the selection of a common solution for both Liquid and Water Vapor time series generation.

5.2.4 Joint solution

Once the single variable optimizations are completed, the simulator goes through a procedure to find a common solution for Liquid Water and Water Vapor Content. The aim is to select the time series of the same days that satisfy simultaneously the requests for the ILWC and IWVC time series generation. This procedure allows maintaining a kind of correlation between the ILWC and IWVC processes under the hypothesis that there is an assessed synchronous variation of the two quantities. Indeed, as it has been investigated in the previous chapter, we observed in Fig. 4.11 is a simultaneous fluctuation of ILWC and IWVC daily maxima during the year. Furthermore, in Tab. 4.5 the classification of daily time series according to the maximum daily L_{max} and V_{max} values preserve a sort of correlation between ILWC and IWVC. Additionally, an advantage of keeping related the ILWC and IWVC time series of the same days is the

enormous simplification of the problem of overlapping the two processes once the T daily time series have been selected.

The joint optimization takes in input the vectors of number of days to be selected $\#_{L,j}$ and $\#_{V,i}$ from each class of ILWC and IWVC and returns the number of elements to be selected in each cell of Tab. 5.3. The scheme procedure of the optimization is depicted in Fig. 5.8.

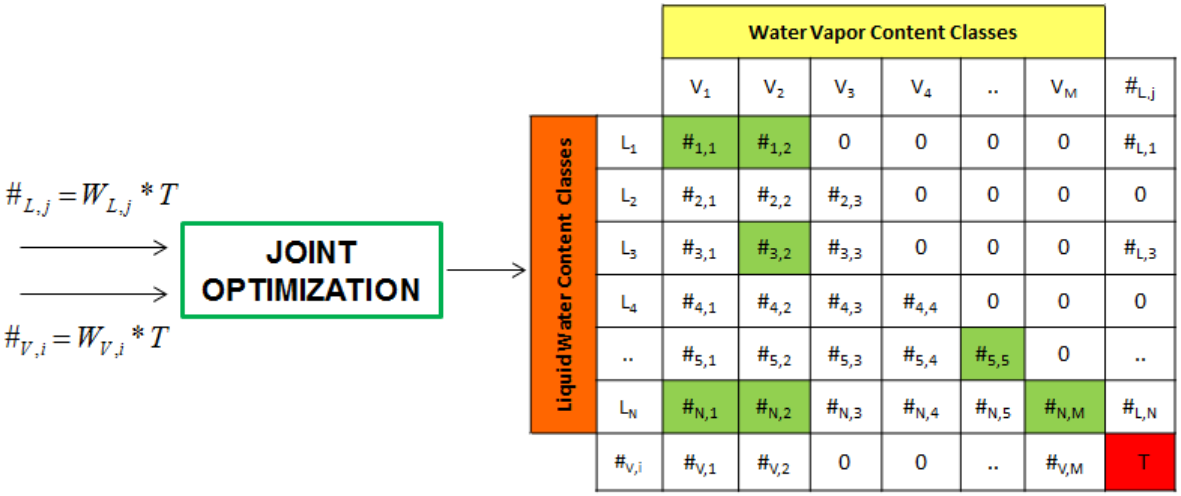

Figure 5.8: *Block scheme of joint optimization of ILWC and IWVC content*

Assuming in input $\#_{L,j}$ the required number of days for the j^{th} class of ILWC and $\#_{V,i}$ the required number of days for the i^{th} class of IWVC, the common solution of the optimization is a matrix of $K = M*N$ elements whose k^{th} element of $\#_{j,i}$ identifies the number of time series to be selected by the cell of coordinates (j,i). The cost function to be optimized is:

$$\sum_{k=1}^{K} \#_{j,i} = T \tag{5.9}$$

where T is the total number of daily time series to be selected. The $\#_{j,i}$ element is forced to be positive and at least equal to the number of available time series for the (j,i) cell. The optimization procedure is constrained by the following functions:

$$\begin{aligned} \sum_{j=1}^{M} \#_{j,i} &= \#_{V,i} \\ \sum_{i=1}^{N} \#_{j,i} &= \#_{L,j} \end{aligned} \tag{5.10}$$

so that the sum of the elements of each column and each row correspond to the request formulated by the single variable optimizations. In the event that, during the joint optimization, one of the constraints is violated and the optimizer cannot converge to a solution, the repetition of the time series during the selection is allowed.

Once the optimization is ended and we identify the vector of numbers $\#_{j,i}$, the time series of each k^{th} cell are randomly ordered and the first $\#_{j,i}$ time series are selected. The solutions obtained in the single variable optimization procedures is quite modified by the joint selection of time series from ILWC and IWVC classes. The differences from one simulation to the other one is introduced by the variability of the time series contained in the same class. An example of the effect of single variable optimization and time series joint selection is shown in Figs. 5.9 for ILWC (a) and IWVC (b), respectively. In these figures we report: in blue the input objective function of ILWC and IWVC ($P(L)_{OBF}$, $P(V)_{OBF}$), in red the result of the single variable optimization ($P(L)_{REF}$, $P(V)_{REF}$) and in green the curves obtained with the selected time series (*selected* CDF $P(L)_{sel}$ and $P(V)_{sel}$ curves).

Some additional considerations can be done: the variability among generated replicas of synthetic time series having as objective the reconstruction of the OBF, is directly dependent from the number of classes considered in the classification of the input databases. When we defined the number of classes, and consequently the number of thresholds L_j and V_j, we observed that by increasing these number we reduced intra class time series variability and therefore we obtained a better reconstruction of the OBF. On the other hand, as the number of daily time series in the database is fixed, by increasing the number of classes, we reduce the number of daily time series in each class. The primary consequence is that we increase the probability of selecting always the same time series, especially if the available time series in a class are less then the required one. A trade off between the observed error and the repetition of daily time series must be accounted. On the contrary, for a fixed number of classes, the way we select the thresholds of the classes does not really influence the error between the objective CDF and the replicas. For this reason we considered the same thresholds whichever the location.

5.2.5 Synthetic time series composition

Maintaining related the daily time series of Liquid Water and Water Vapor during the synthetic time series generation helps the overlapping of the two time varying process. The generation of the synthetic time series allows the reconstruction of period from one year till several years. We considered a basic length T of 365 days (single year). With this timing it is possible to appreciate the variability introduced by the time series generator in each replica. When a single year (or more) is assumed, a time ordering criterion is required. Indeed, as shown in the previous chapter, the yearly distribution of ILWC and IWVC respects a quite evident seasonal variation (Fig. 4.11) where the higher values of daily maximum L_{max} and V_{max} are distributed during summer. Therefore, a simple method to order the daily time series is introduced. We keep track of the original occurrence (the month of the measurement) of the daily time series and we order the selected daily time series accordingly. The time series that fall within the same month are ordered randomly in order to create a sort of variability in case of repetition from one replica to another.

We observed that the tendency of the time series generator is to selects almost one-fourth of the simulated period T from every season of the RADDB. Therefore, the resulting synthetic time series is composed by a sequence of daily time series with an intrinsic realistic seasonal variation. An estimate of this trend can be assessed by

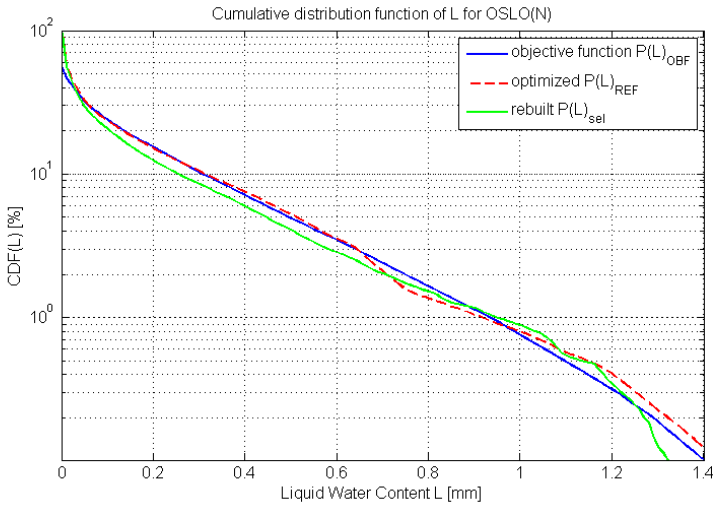

(a)

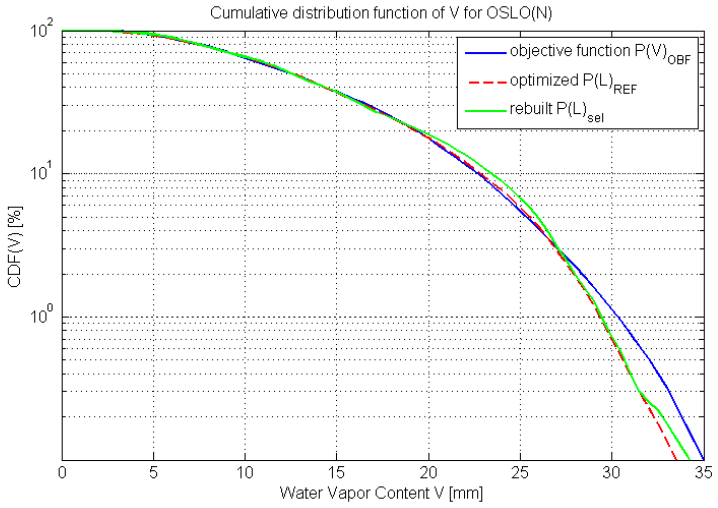

(b)

Figure 5.9: *An example of single optimization results ($P(L_{REF})$ curve, red line) and joint optimization results (selected CDF $P(L)_{sel}$ curves, green line) for ILWC (a) and IWVC (b) obtained taking in input the CDF provided by ITU-R model (blue curve) for Oslo(N) for a single year simulation (T=365 days).*

comparing the RAOBS measurements and the selected time series. The RAOBS experiments collects two measurements per day (12.00 and 00.00), excluding rainy periods. Therefore, we averaged the ILWC and IWVC quantities each minute and we ordered the selected time series taking into account the complete date to be more consistent with the measured data. The result of this comparison is reported in 5.10 where in red are depicted the radiometric measurements generated by the optimizer and in blue the RAOBS measurements for the city of Hemsby-In-Norfolk (UK).

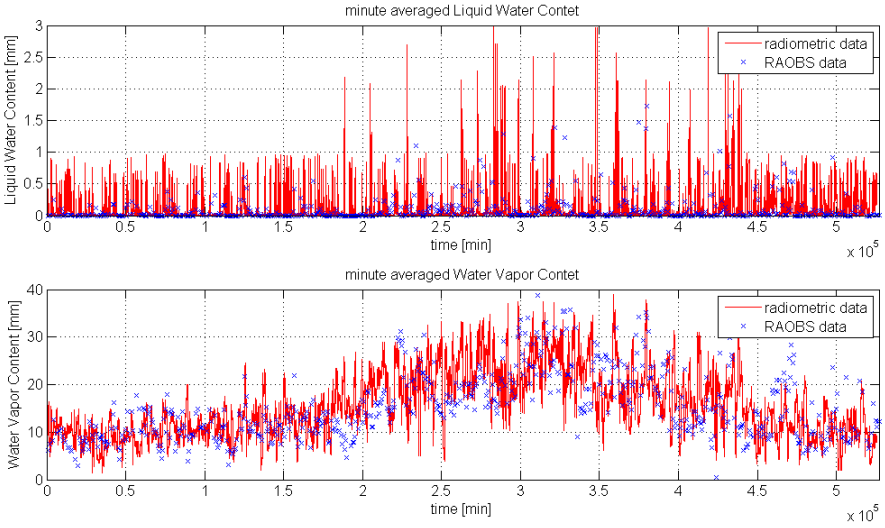

Figure 5.10: *Comparison of synthetic time series of minute averaged ILWC and IWVC samples obtained by radiometric measurements (red line) and yearly RAOBS measurements (blue markers) for Liquid Water (a) and Water Vapor (b) content for the city of Hemsby-In-Norfolk (UK)*

5.3 Dynamic channel validation

The objective of this section is to present the procedure adopted for the validation of the time varying channel model of Liquid Water and Water Vapor Content. In the past some validation procedure have been used to compare, on statistical term, the reliability of the retrieved ILWC and IWVC quantities with concurrent measurements of other instruments: the validation of radiometric measurements with radiosounding [58] [43], the comparison with both radiosounding and forecasts [59] or the assessment with sensors [47]. Several study was performed for the validation of IWVC quantities with GPS receiver [60]. The main objective of all the studies was to assess the accuracy of the retrieval method and of the calibration procedure.

On a long term analysis the synthetic time series of ILWC and IWVC must generate statistics that approaches the input OBF functions. However, a better knowledge of the dynamics of cloud events and the distribution of ILWC and IWVC values within the synthetic time series can be useful for better investigate the physical basis of our new approach. The reproduction of a realistic behaviour of the synthetic time series is not forced during the daily time series selection, therefore we can only verify if the algorithm respect in a broad sense the intra annual ILWC and IWVC variation. This validation can be done only in a qualitative way, since we do not have a database with a sufficient number of measurements (RAOBS collects only two measurements per day in non rainy condition) to characterize in detail the seasonal variation of ILWC and IWVC.

Therefore, the validation procedure focuses on two main aspects:

- First order statistic validation: we evaluate the ability in the reconstruction of the OBF statistics through the generation of several replicas of the synthetic time series. We consider the discrepancy between the OBF and a long-term statistic

obtained by ten years of synthetic time series and the analysis of the statistic variation within the ten replicas (inter replicas validation);

- Seasonal and Classification validation: this qualitative analysis allows to assess the seasonal variations of ILWC and IWVC in the generated annual replicas to ensure an intra annual dynamics of these values and examines if the ILWC and IWVC samples selected for the synthetic time series follow the ILWC and IWVC of the specific location evaluated trough RAOBS data.

For the validating procedure we make use of radiosounding measurements RAOBS (FERAS database) collected in Europe for a period of 10 years (1980-1989). The sites examined in the validation are the ones reported in Tab. 5.4. We generate for each site 10 replicas of one year length of synthetic time series assuming as OBF the CDF of Liquid Water and Water Vapor derived from RAOBS.

Table 5.4: *List of selected sites for FERAS measurements considered for the test of ILWC and IWVC quantities*

Station Code	City	Country	Latitude (°)	Longitude (°)	n° available samples
02836	Sodankyla	FI	67.22	26.39	4012
02963	Jokioinen	FI	60.49	23.30	4525
03496	Hemsby-In-Norfolk	UK	52.41	1.41	6190
10384	Berlin(Templehof Airport) (Us)	DL	52.29	13.25	2787
16080	Milano (Linate Airport)	IT	45.39	9.49	4966
16429	Trapani (Birgi Airport)	IT	37.55	12.30	4288
03026	Stornoway	UK	58.13	-6.59	4764

5.3.1 First order statistic validation

In this paragraph we exploit a well know procedure [43] adopted for the validation of first order statistics. As discussed so far, the generator returns a synthetic time series that differs each time the simulation is performed. This difference is introduced by the variability of the time series pertaining to the same class that are randomly chosen during the joint selection procedure. Therefore, even if the input statistic is fixed, the generated time series can slightly differs one from another. An example of this variability is shown in Figs. 5.11 where in blue is depicted the OBF, in black the 10 replicas of synthetic time series and in red the long term solution obtained by considering all the replicas. As shown in these figures, the aggregated CDF converge to the objective function.

In this section we want to evaluate the ability of the synthetic time series generator in reproducing the input OBF function, i.e. how much the long term statistic obtained by all replicas converges to the OBF. Furthermore, we compare the size of the inter-replicas variability that is automatically introduced by the synthesizer with the one assessed for the 7 years of RADDB in Spino d'Adda to assess if it is equivalent.

Long-term statistic validation

The performance of the time series generator is assessed by measuring the *discrepancy* ϵ, i.e. the difference of ILWC and IWVC values between the OBF and the long-term statistic obtained by putting together ten years of synthetic replicas, evaluated at

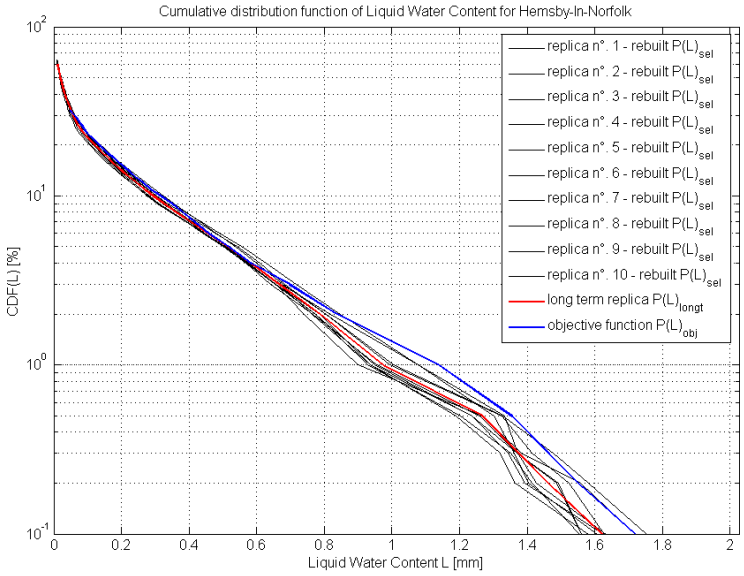

(a)

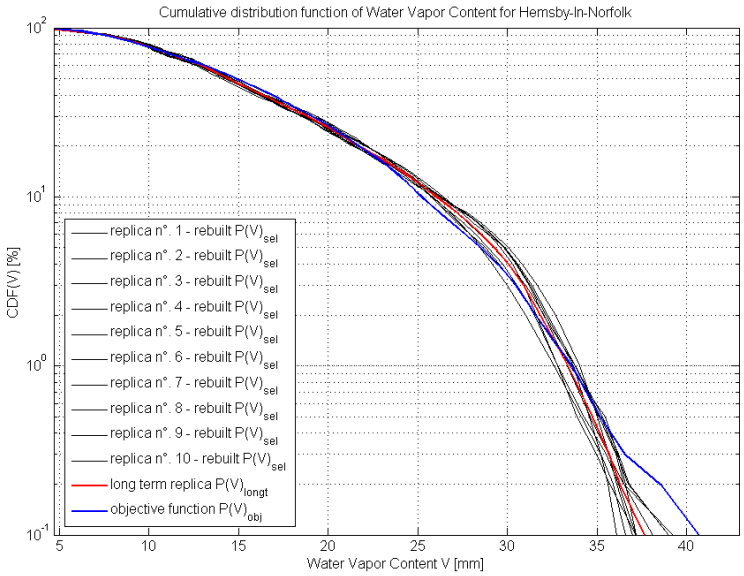

(b)

Figure 5.11: *Experimental OBF (blue line), 10 years of synthetic CDF (black lines) and long term CDF (red line) of Liquid Water (a) and Water Vapor (b) content for Hemsby-In-Norfolk (UK).*

the same probability levels. For this analysis we assume a vector of time percentages P=[0.1, 0.2, 0.3, 0.5, 1, 2, 3, 5, 10, 20, 30, 40, 50, 60, 70, 80, 90 100] [%] where, i.e. the 0.1% of time corresponds to less than 9 hours.

The discrepancy ϵ_{mm} [mm] at probability p is given by:

$$\begin{aligned} \epsilon_{L,mm}(p) &= L_{longt}(p) - L_{OBF}(p) \quad [mm] \\ \epsilon_{V,mm}(p) &= V_{longt}(p) - V_{OBF}(p) \quad [mm] \end{aligned} \tag{5.11}$$

where L_{longt} and V_{longt} are the synthetic long-term function obtained by putting together ten years of synthetic replicas and L_{OBF} and V_{OBF} are the OBF function. The entity of this difference can be better appreciated by evaluating the percentage discrepancy ϵ_P where the distance between the objective and the selected CDF functions for the same probability is weighted by the absolute value of L and V assumed in the OBF functions:

$$\begin{aligned} \epsilon_{L,P}(p) &= 100\frac{L_{longt}(p) - L_{OBF}(p)}{L_{OBF}(p)} \quad [\%] \\ \epsilon_{V,P}(p) &= 100\frac{V_{longt}(p) - V_{OBF}(p)}{L_{OBF}(p)} \quad [\%] \end{aligned} \tag{5.12}$$

An example of the measured ϵ_{mm} and ϵ_P for the scenario depicted in Figs. 5.11 are shown in Fig. 5.12 and 5.13. In red is reported the discrepancy between the OBF and the long-term time series L_{longt} and V_{longt}. The absolute value of discrepancy for different probability levels are reported in Tab. 5.5 and in Tab. 5.6.

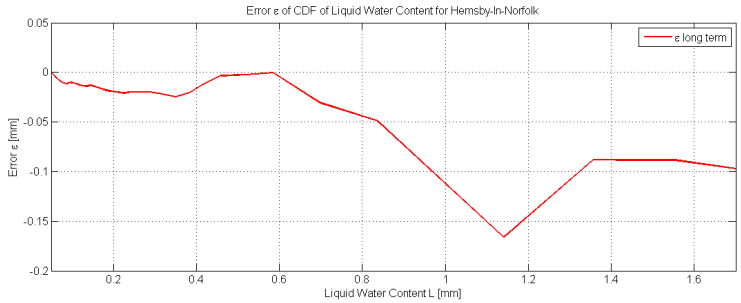

(a)

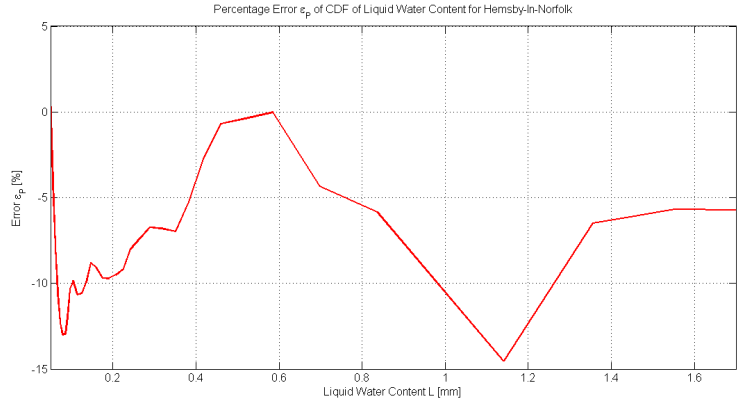

(b)

Figure 5.12: *Discrepancy $\epsilon_{L,mm}$ (a) and $\epsilon_{L,P}$ (b) referred to CDF functions depicted in Fig. 5.11 (a)*

In Tab. 5.7 and 5.8 we report the absolute value of discrepancy factor ϵ_{mm} and ϵ_P averaged over probability levels for all sites reported in Tab. 5.4. For all the considered sites, this discrepancy is below 11% for ILWC and 8 % for IWVC.

Inter replicas validation

The inter replicas variability introduced in the generation of each synthetic replica can be evaluated in terms of discrepancy between each replica and the long-term statistic obtained through 10 years of synthetic time series. Therefore, we evaluate how much

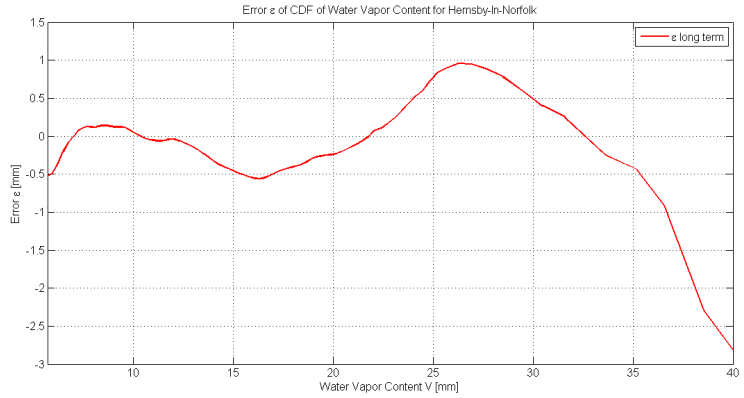

(a)

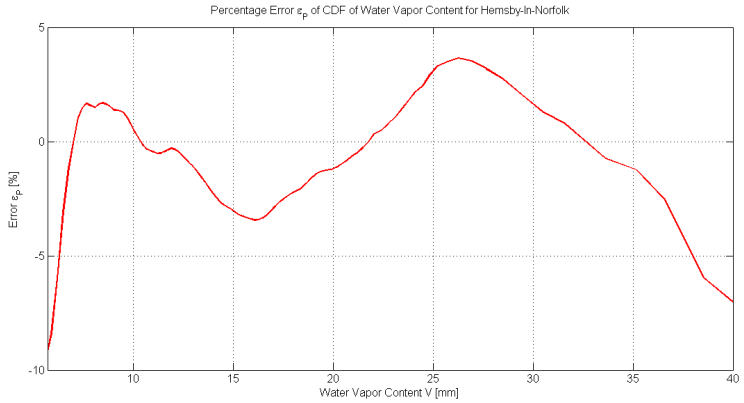

(b)

Figure 5.13: *Discrepancy $\epsilon_{V,mm}$ (a) and $\epsilon_{V,P}$ (b) referred to CDF functions depicted in Fig. 5.11 (b)*

Table 5.5: *Absolute value of discrepancy of ILWC for selected probability levels for Hemsby-In-Norfolk (UK).*

probability p	$\epsilon_{L,mm}(p)$ [mm]	$\epsilon_{L,P}(p)$ [%]
0.1	0.1047	6.0873
0.2	0.0947	6.0999
0.3	0.0908	6.2042
0.5	0.0877	6.4658
1.0	0.1655	14.5008
2.0	0.0507	6.0555
3.0	0.0342	4.8968
5.0	0.0170	3.2719
10.0	0.0230	7.2315
20.0	0.0139	10.2192
	$\epsilon_{L,mm}$ [mm]	$\epsilon_{L,P}$ [%]
	0.0625	7.1887

the CDF of each generate time series varies from the long term statistic. We defined a root mean square of discrepancy as the most significant figure of merit to evaluate the variability introduced among all synthetic replicas.

Table 5.6: *Absolute value of discrepancy of IWVC for selected probability levels for Hemsby-In-Norfolk (UK).*

probability p	$\epsilon_{V,mm}(p)$ [mm]	$\epsilon_{V,P}(p)$ [%]
0.1	3.0559	7.5080
0.3	0.9091	2.4859
1.0	0.3951	1.1750
3.0	0.5219	1.7117
10.0	0.8425	3.3380
30.0	0.3200	1.6750
50.0	0.4386	2.9440
70.0	0.2652	2.3708
90.0	0.1582	2.0658
	$\epsilon_{V,mm}$ [mm]	$\epsilon_{V,P}$ [%]
	0.7108	2.6266

Table 5.7: *Absolute value of discrepancy of ILWC averaged over probability levels for all sites collected in Tab. 5.4 over 10 replicas of 1 year length each.*

Site	$\epsilon_{L,mm}$ [mm]	$\epsilon_{L,P}$ [%]
Sodankyla	0.0600	9.2876
Jokioinen	0.0800	8.6485
Hemsby-In-Norfolk	0.0625	7.1887
Berlin(Templehof Airport)	0.0710	9.0244
Milano (Linate Airport)	0.0492	8.9984
Trapani (Birgi Airport)	0.0546	11.2415
Stornoway	0.0630	7.4935

Table 5.8: *Absolute value of discrepancy of IWVC averaged over probability levels for all sites collected in Tab. 5.4 over 10 replicas of 1 year length each.*

Site	$\epsilon_{V,mm}$ [mm]	$\epsilon_{V,P}$ [%]
Sodankyla	0.6306	7.5579
Jokioinen	0.8717	7.9077
Hemsby-In-Norfolk	0.7108	2.6266
Berlin(Templehof Airport)	0.5232	2.8321
Milano (Linate Airport)	0.6498	2.9831
Trapani (Birgi Airport)	1.1251	3.4225
Stornoway	0.4284	2.0019

Assuming $\epsilon_L(i,p)$ the ILWC discrepancy for the i^{th} of N synthetic replicas at the p^{th} of M probability level and $T(i)$ the length of the i^{th} synthetic replica, we can evaluate the root mean square error of the p^{th} probability level as:

$$rms_{\epsilon_L}(p) = \sqrt{\frac{\sum_{i=1}^{N} \epsilon_L^2(i,p)T(i)}{\sum_{i=1}^{N} T(i)}} \tag{5.13}$$

Assuming that the length of all the replicas is equal, we simply obtain an averaged value of the absolute values of $\epsilon_L(i,p)$ at the same probability level. The total discrepancy $rms_{\epsilon_{L,TOT}}$ is evaluated considering all N replicas at all M probability level. Assuming $T(p)$ as the sum of the length of all synthetic replicas available at the probability p, the

root mean square discrepancy is expressed as:

$$rms_{\epsilon_{L,TOT}} = \sqrt{\frac{\sum_{p=1}^{M} \epsilon_L^2(p) T(p)}{\sum_{p=1}^{M} T(p)}} \tag{5.14}$$

that is simply translated into an averaged values of rms_{ϵ_L} when the length of all the replicas is equal.

An analogous procedure is performed for the evaluation of the IWVC discrepancy. The values of rms discrepancy for Hemsby-In-Norfolk for a subset of probability levels for the 10 replicas and the total rms are reported in Tab. 5.9 and 5.10. From Tab. 5.9 and 5.10 it appears that the percentage $rms_{\epsilon_L}(p)$ and $rms_{\epsilon_V}(p)$ have low values for all the considered probability levels, and it is confirmed also from the total errors: we evaluate about 4.5 $\%$ of error for ILWC and 1.5 $\%$ of error for IWVC. The analysis was carried out for all the sites listed in Tab. 5.4 and the results are reported in 5.11 and 5.12.

Table 5.9: *Inter-replicas variability of ILWC for selected probability levels for Hemsby-In-Norfolk (UK) over 10 replicas of 1 year length each.*

probability p	$rms_{\epsilon_L}(p)$ [mm]	$rms_{\epsilon_L}(p)$ [%]
0.1	0.0496	3.0625
0.2	0.0641	4.3633
0.3	0.0274	2.0061
0.5	0.0457	3.5680
1.0	0.0461	4.8153
2.0	0.0256	3.2303
3.0	0.0156	2.3341
5.0	0.0162	3.1265
10.0	0.0131	4.4293
20.0	0.0091	7.4503
	$rms_{\epsilon_{L,TOT}}$ [mm]	$rms_{\epsilon_{L,TOT}}$ [%]
	0.0229	4.5198

Table 5.10: *Inter-replicas variability of IWVC for selected probability levels for Hemsby-In-Norfolk (UK) over 10 replicas of 1 year length each.*

probability p	$rms_{\epsilon_V}(p)$ [mm]	$rms_{\epsilon_V}(p)$ [%]
0.1	0.8563	2.3009
0.3	0.3702	1.0364
1.0	0.3983	1.1915
3.0	0.4271	1.3805
10.0	0.2262	0.8678
30.0	0.2490	1.3222
50.0	0.1747	1.2088
70.0	0.2640	2.3780
90.0	0.1266	1.6242
	$rms_{\epsilon_{V,TOT}}$ [mm]	$rms_{\epsilon_{V,TOT}}$ [%]
	0.3137	1.3527

To evaluate the reliability of the inter-replicas variability we assume as term of comparison the inter-year variability detected for the RADDB for Spino d'Adda. We expect

to estimate a inter-replicas variability that does not exceed the inter-annual variability detected in RADDB. The total year to year variability of ILWC and IWVC obtained for this database is 10 % and 5.0%, respectively as shown in Tab. 5.13. Assuming the RADDB inter annual variability as representative for the European region, the results of Tab. 5.11 and Tab. 5.12 highlight that all the assessed inter-relicas variabilities are acceptable. Indeed, all considered sites shown a $rms_{\epsilon_{L,TOT}}$ minor than 7 % and $rms_{\epsilon_{V,TOT}}$ minor than 2 %. In particular for Milano (Linate) we obtain a $rms_{\epsilon_{L,TOT}}$ = 5% and $rms_{\epsilon_{V,TOT}}$=1%.

Table 5.11: *Total variability of ILWC for all sites over 10 replicas of 1 year length*

Site	$rms_{\epsilon_{L,TOT}}$ [mm]	$rms_{\epsilon_{L,TOT}}$ [%]
Sodankyla	0.0230	4.9187
Jokioinen	0.0277	5.2936
Hemsby-In-Norfolk	0.0229	4.5198
Berlin(Templehof Airport)	0.0184	3.6275
Milano (Linate Airport)	0.0225	4.8341
Trapani (Birgi Airport)	0.0319	7.0937
Stornoway	0.0241	4.3286

Table 5.12: *Total variability of IWVC for all sites over 10 replicas of 1 year length*

Site	$rms_{\epsilon_{V,TOT}}$ [mm]	$rms_{\epsilon_{V,TOT}}$ [%]
Sodankyla	0.2277	1.2766
Jokioinen	0.3782	1.5824
Hemsby-In-Norfolk	0.3137	1.3527
Berlin(Templehof Airport)	0.3211	1.2053
Milano (Linate Airport)	0.1840	1.0017
Trapani (Birgi Airport)	0.3810	1.3376
Stornoway	0.3275	1.4088

Table 5.13: *Total variability derived from RADDB.*

$rms_{\epsilon_{L,TOT}}$ [mm]	$rms_{\epsilon_{L,TOT}}$ [%]
0.0296	9.8607
$rms_{\epsilon_{V,TOT}}$ [mm]	$rms_{\epsilon_{V,TOT}}$ [%]
1.4051	5.2025

5.3.2 Intra annual validation

In this section we perform a qualitative analysis of the behaviour of ILWC and IWVC obtained through the time series synthesis. The validation of the first order statistic gives a performance indicator of the ability of the time series synthesizer in the reconstruction of an OBF. This parameter is essential to provide a global evaluation of the system. However, it does not guarantee to maintain the realistic site-dependent characterization of the ILWC and IWVC dynamics observed in RAOBS or radiometric local measurements. There are two main aspects in the generation of a synthetic time series that are crucial for the representation of the climatology of a given site: the variation of ILWC and IWVC during the year (if seasonal behaviour are somehow respected) and

the estimate of the site-specific joint variation of ILWC and IWVC. It is important to specify that during the synthesis we do not care of any of these aspects, however we are interested in assessing the realistic behaviour of ILWC and IWVC synthetic time series.

These validations are qualitative analysis and are performed to give a better ideas of the physical tendency of the generated time series on short-time basis. These validations required the use of additional ILWC and IWVC measurements collected in the specific site. Unfortunately, we do not have additional measurements of local ILWC and IWVC daily time series measured by radiometer to be compared with the synthetic one, therefore we assumes as reference the measurements performed during RAOBS campaigns.

5.3.2.1 Seasonal variation

The basic idea of this analysis is to verify the cyclic variation of ILWC and IWVC assumed within the yearly synthetic time series. As assessed in section 4.4, the higher daily peaks of ILWC and IWVC daily time series are experienced during summer. The 10 years of measurements collected in each site by RAOBS prove this tendency. What we try to assess is if the intra-annual variation of ILWC and IWVC values after the ordering of daily time series respects the tendency detected in the experimental one.

For this analysis we take the minute-averaged values of ILWC and IWVC of the synthetic time series ordered according to procedure presented in section 5.2.5. On the contrary, for RAOBS measurements we consider one year of data collected every 12 hours (in absence of rain). Even if the time sampling is different, in Fig. 5.14, 5.15 and 5.16 we observe a good agreement in the behaviour of maximum and minimum values experienced by ILWC and IWVC. In particular the seasonal variation is quite evident for both the time varying process for all locations.

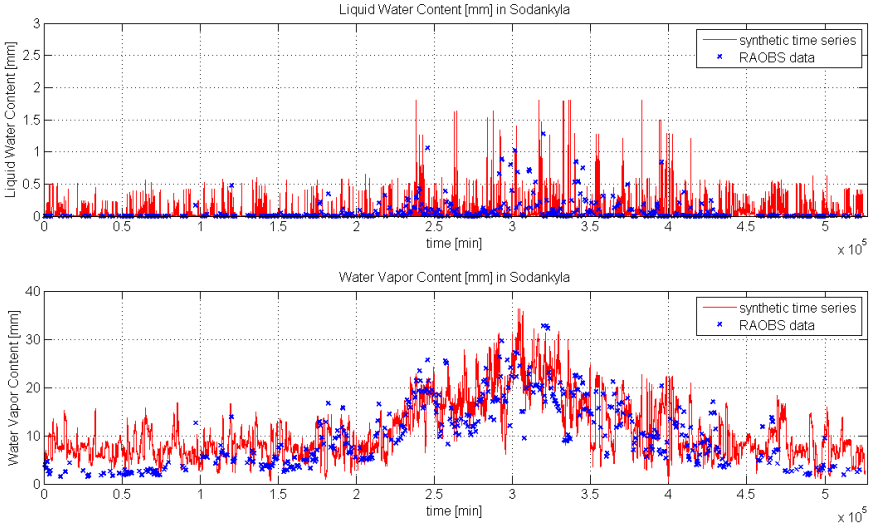

Figure 5.14: *Comparison of synthetic time series of minute averaged ILWC and IWVC samples obtained by radiometric measurements (red line) and one year (1985) RAOBS measurements (blue markers) for Liquid Water and Water Vapor content for city of Sodankyla (FI).*

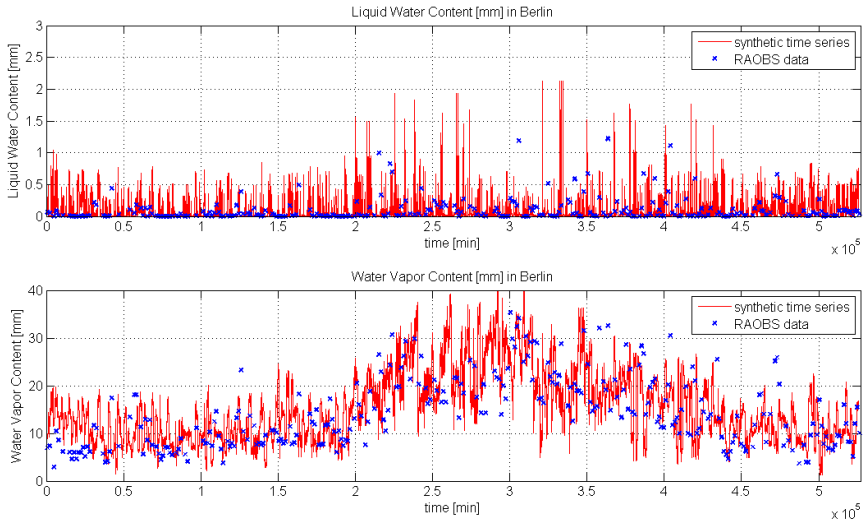

Figure 5.15: *Comparison of synthetic time series of minute averaged ILWC and IWVC samples obtained by radiometric measurements (red line) and one year (1980) RAOBS measurements (blue markers) for Liquid Water and Water Vapor content for city of Berlin (DL).*

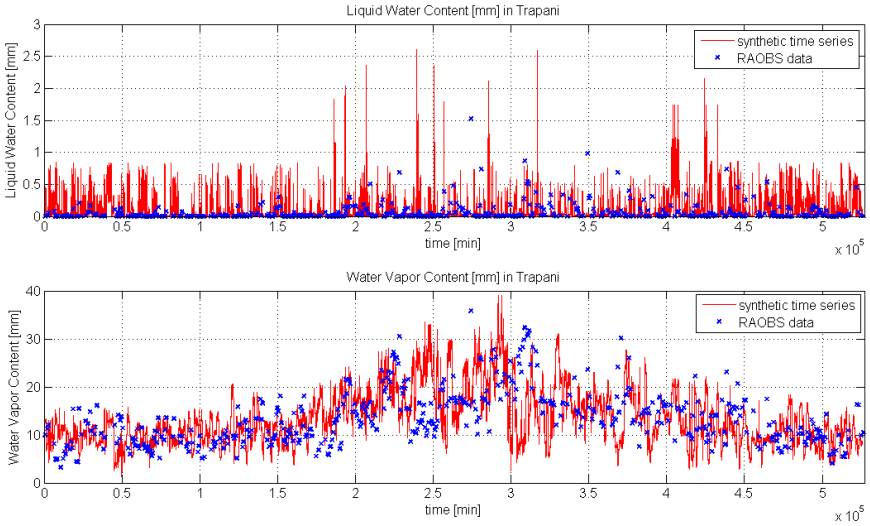

Figure 5.16: *Comparison of synthetic time series of minute averaged ILWC and IWVC samples obtained by radiometric measurements (red line) and one year (1982) RAOBS measurements (blue markers) for Liquid Water and Water Vapor content for city of Trapani (IT) (c).*

5.3.2.2 Classification validation

During the synthesis of a time series for a specific location we extract a sub-set of daily time series from the RADDB collected in Spino d'Adda. The main hypothesis behind this procedure is that the synchronous variation of ILWC and IWVC detected in Spino d'Adda can be assumed as effective for every simulated site. Making use of RAOBS measurements, we are able to verify if the hypothesis of ILWC and IWVC dependency is valid for location other that Spino d'Adda. Therefore, we want to verify if the daily time series selected during synthesis maintain the site dependent variation between ILWC and IWVC detected by RAOBS.

We start classifying the Liquid Water and Water Vapor content evaluated in each RAOBS measurements according to the thresholds reported in Tab. 5.1 and 5.2. We observe that, as shown in Tab. 5.3 for all the sites there is the tendency of having no low values of IWVC simultaneously with high values of ILWC and viceversa. However, the distribution of values in the box of the grid is quite similar from site to site. This results are shown in Fig. 5.17.

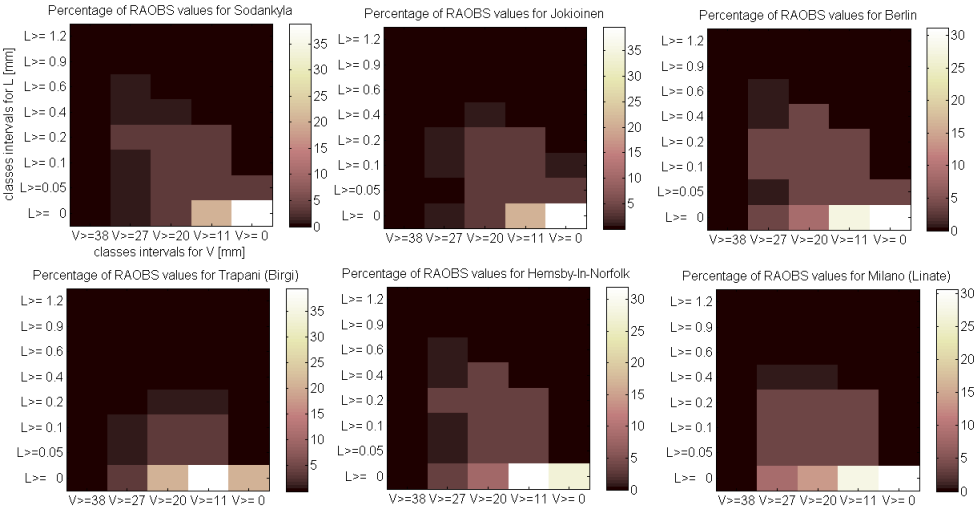

Figure 5.17: *Probability of classified RAOBS values for 10 years of measurements for 6 sites [Sodankyla, Jokioinen, Hemsby-In-Norfolk, Berlin(Templehof Airport), Trapani (Birgi Airport) and Stornoway]*

Once the synthesis of a time series is performed, we classify each sample of the selected daily time series (not only the daily peak) in order to verify if the selected daily time series maintain the site specific joint variation highlight in Fig. 5.17. We performs this analysis for different sites simulating for 5 synthetic replicas of one year length. The results are shown in Fig. 5.18, 5.19, 5.20, 5.21, 5.22, 5.23 and 5.24. In each figure the first subfigure is referred to RAOBS measurements, while the other are referred to synthetic time series. We observe that, in the synthetic time series generation the site specific classification of ILWC and IWVC observed in the RAOBS measurements is quite respected.

Furthermore, the number of samples that follow in each class of ILWC or IWVC classification, i.e. the sum of samples in each row and column of the grid, respect the weights identified during the single variable optimization for ILWC and IWVC. This constraint was not imposed during the optimization procedure. It is important to underline that, for the radiometric database, the classification of daily time series is performed on the daily peak (L_{max} and V_{max}), therefore we cannot a priori guarantee that all the ILWC and IWVC samples in the daily time series maintain the assumed classification.

After these two qualitative analysis, we can assert that, even if the input RADDB is site specific, the generated synthetic time series reproduce not only the site-specific classification of ILWC and IWVC samples, but also the realistic behaviour of ILWC and IWVC detected trough RAOBS data.

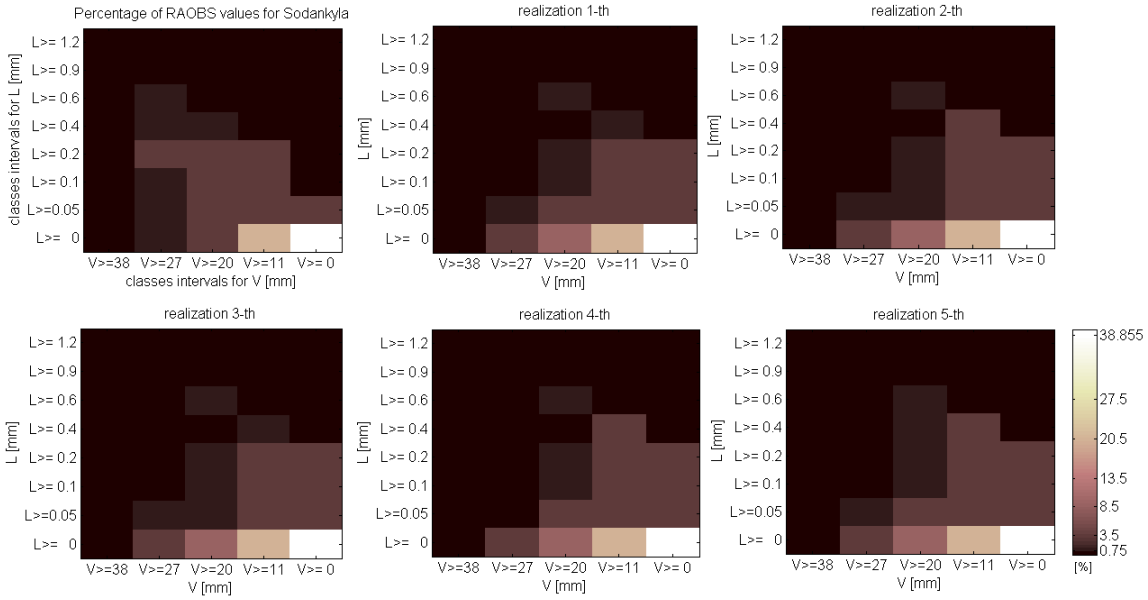

Figure 5.18: *Probability of classified RAOBS values for 10 years of measurements for Sodankyla and corresponding classification of 5 generated time series replicas*

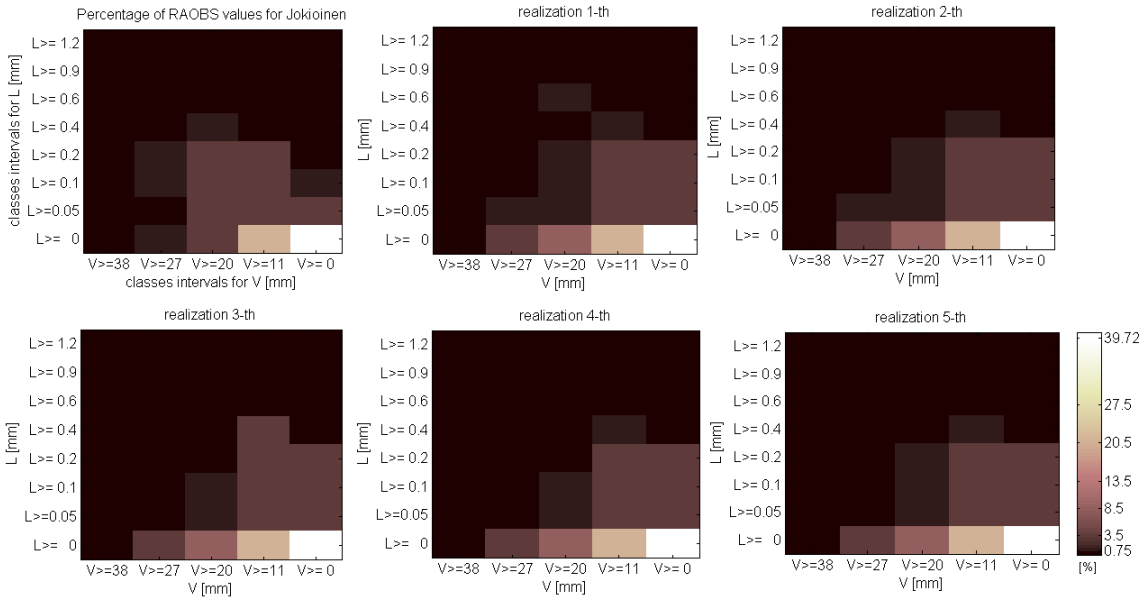

Figure 5.19: *Probability of classified RAOBS values for 10 years of measurements for Jokioinen and corresponding classification of 5 generated time series replicas*

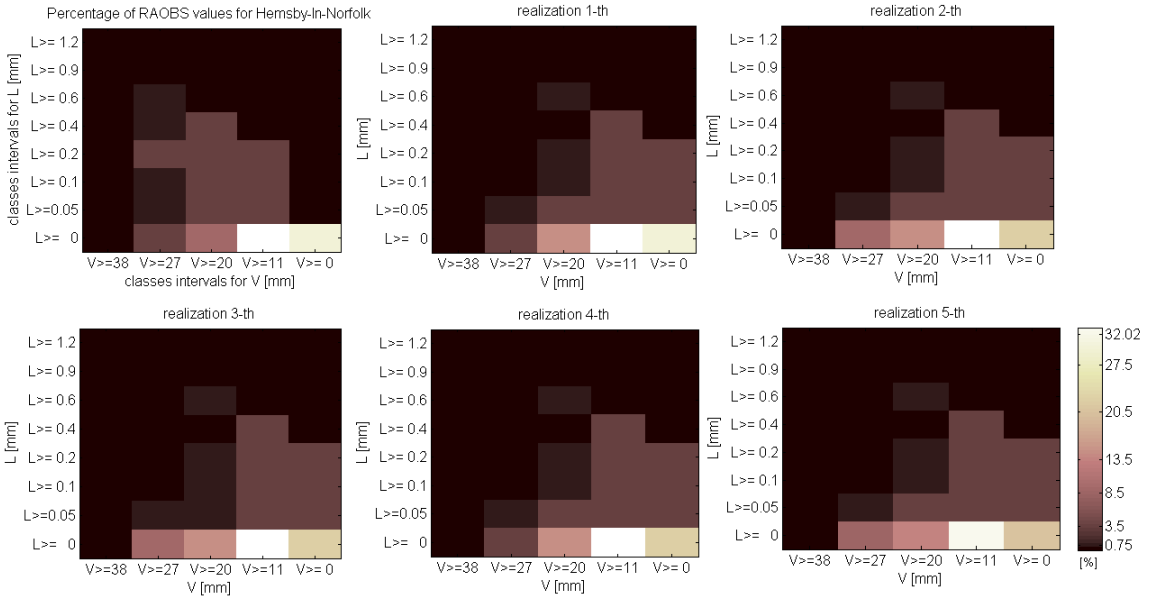

Figure 5.20: *Probability of classified RAOBS values for 10 years of measurements for Hemsby-In-Norfolk and corresponding classification of 5 generated time series replicas*

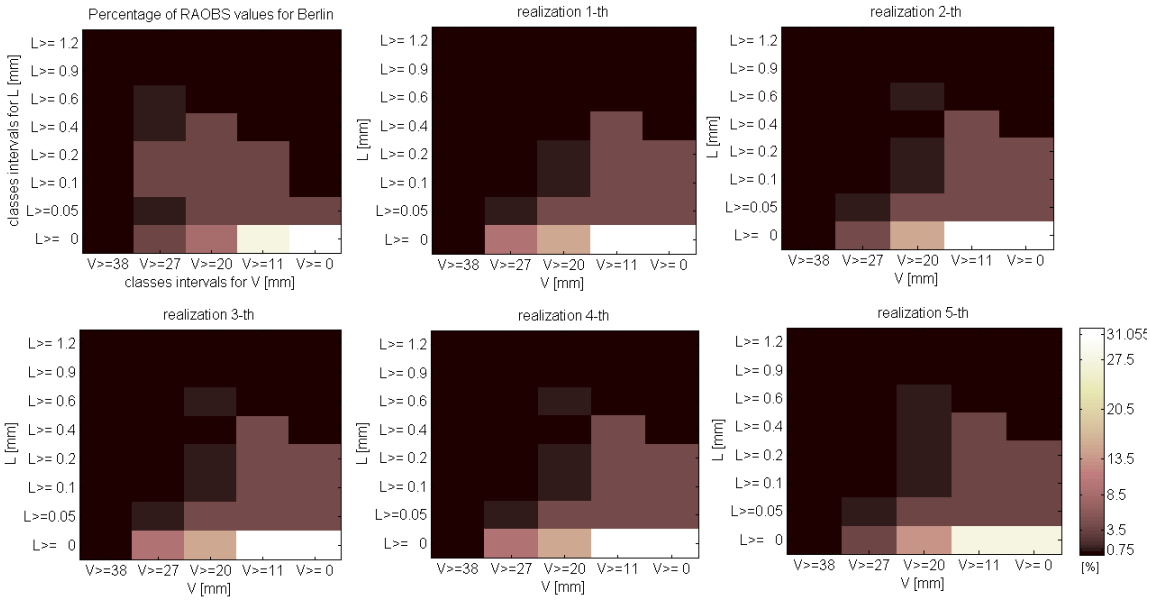

Figure 5.21: *Probability of classified RAOBS values for 10 years of measurements for Berlin(Templehof Airport) and corresponding classification of 5 generated time series replicas*

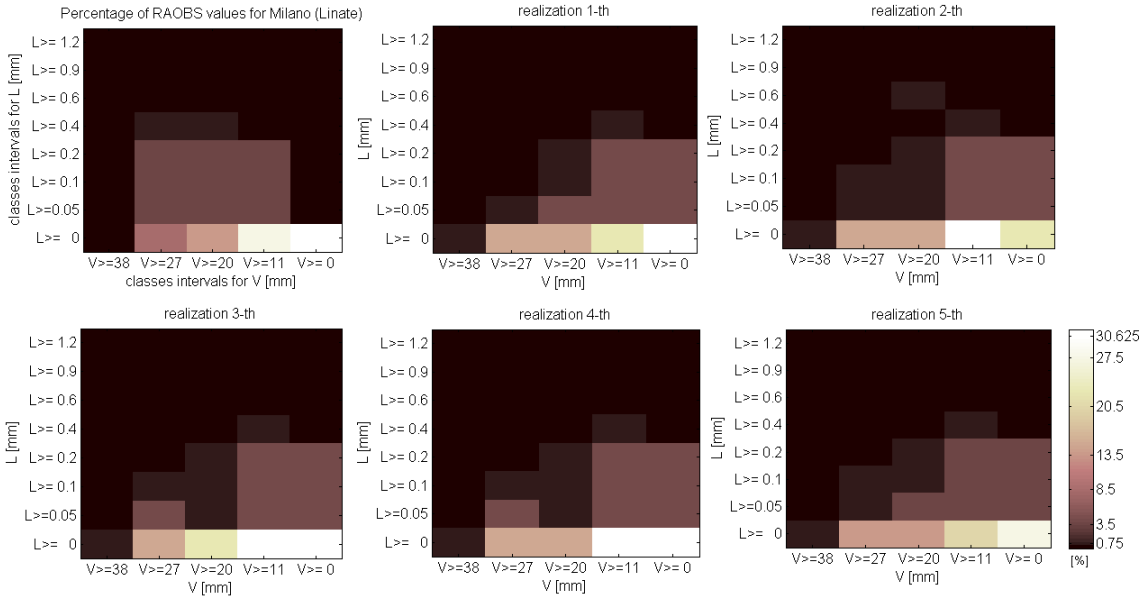

Figure 5.22: *Probability of classified RAOBS values for 10 years of measurements for Milano (Linate Airport) and corresponding classification of 5 generated time series replicas*

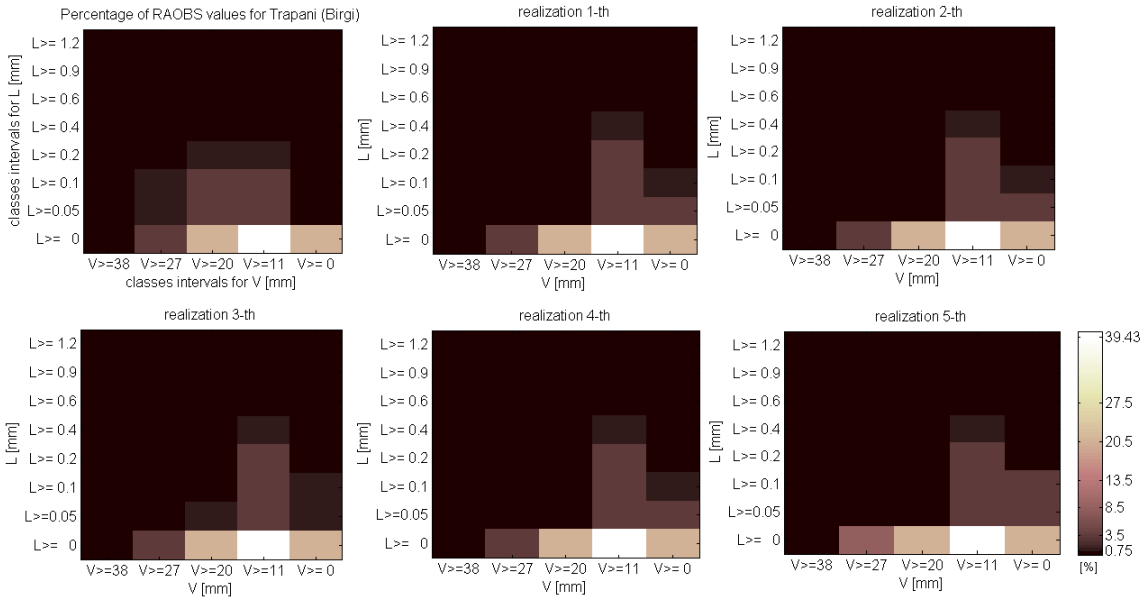

Figure 5.23: *Probability of classified RAOBS values for 10 years of measurements for Trapani (Birgi Airport) and corresponding classification of 5 generated time series replicas*

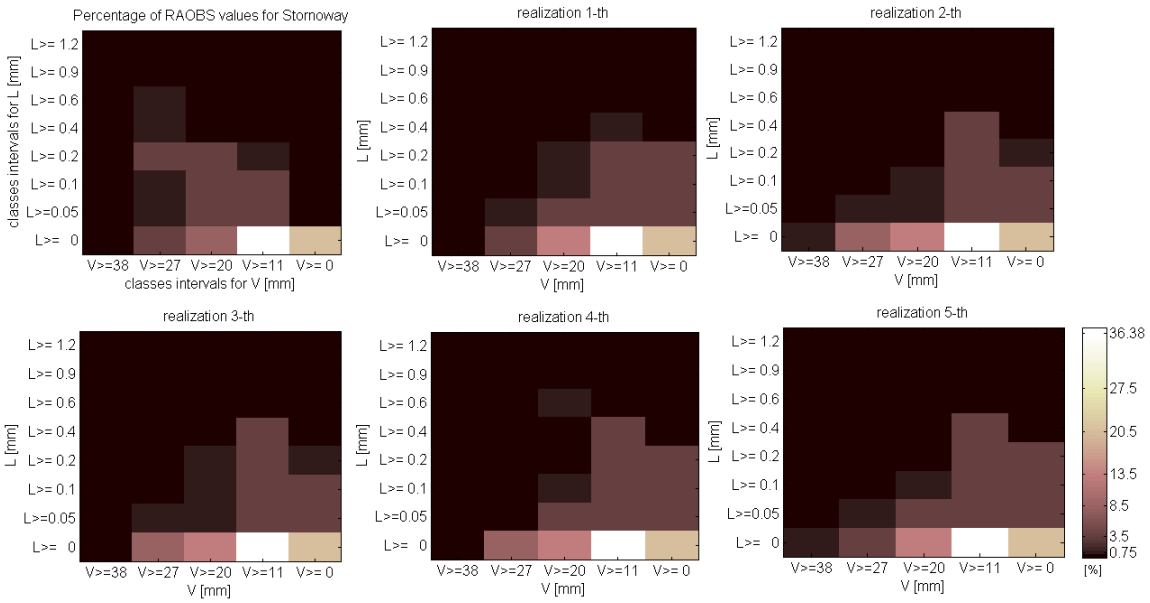

Figure 5.24: *Probability of classified RAOBS values for 10 years of measurements for Stornoway and corresponding classification of 5 generated time series replicas*

CHAPTER 6

Synthesis of rain attenuation time series

6.1 Introduction

In this chapter we analyse the procedure for the synthesis of rain attenuation time series by means of a Rain Time Series Generator (RTSG). This synthesizer is able to reproduce the statistics of rain attenuation of a site (measured or derived from ITU-R model) by selecting a sub-set of measured time series of "rain attenuation" events from an available database. This database is constituted by rain attenuation events measured in Spino D'Adda during the ITALSAT experiment (ITALSAT Database ITDB). The main assumption is that the database is representative for the generation of synthetic time series of rain attenuation in any location. The time series of each event in the database is catalogued in accordance with its maximum attenuation values. The attenuation events are scaled to be adapted to the simulated satellite system frequency and elevation angle. The validation of the synthetic time series is performed for the first and second order statistics making use of a Database of measurements (DBSG5 of ITU-R) that collects experimental measurements for radio-link with frequency between 6 and 35 GHz and elevation angle between 6° and 83°. Furthermore, we include in the validation the site of Spino D'Adda with the beacon measurements at 39.6 and 49.5 GHz and elevation angle at 37.7°. The validation underlines the ability of the RTSG in replicating the input statistic of different sites.

Since the RTSG has been tested with a database of measurements with a frequency range up to 50 GHz, we assume that is valid for frequencies between 5 GHz and 50 GHz and elevation angles between 5° and 90°.

6.2 Rain events database

The goal of the rain attenuation time series generator (RTSG) is to select a sub set of rainy attenuation time series from the input database of events that reproduce the long-term statistic of a given location.

The input rain attenuation database (ITDB) is composed of events of rain attenuation extracted by beacon receiver measurements collected from the Italian satellite ITALSAT with a 3.5 m antenna in Spino d'Adda. Seven years of data (from 1994 till 2000) have been collected at 18.7, 39.6 and 49.5 GHz at an elevation angle of 37.7°. Beacon measurements were collected with 1 second sampling rate. An example of the measured rain attenuation at three different frequencies is reported in Fig. 6.1. In the ITDB database we include only measurements at 18.7 GHz for a total of about 2800 events of a total duration of about 2700 hours. The beacon receiver measurements are filtered with a low pass filter (5^{th} order Butterworth filter with cut-off frequency of 0.025 Hz) to remove scintillation effects. Then, to extract attenuation due to rain, the "zero-dB level" is identified for each event by making use of a radiometer co-located in Spino D'Adda that collects measurements of brightness temperature at 23.8 and 31.6 GHz. As shown in Fig. 6.2, when a rainy event is detected, the contribution of clear-sky components (oxygen, water vapor and liquid water) identified by the zero-dB level is subtracted to the total attenuation to derive the rain attenuation only.

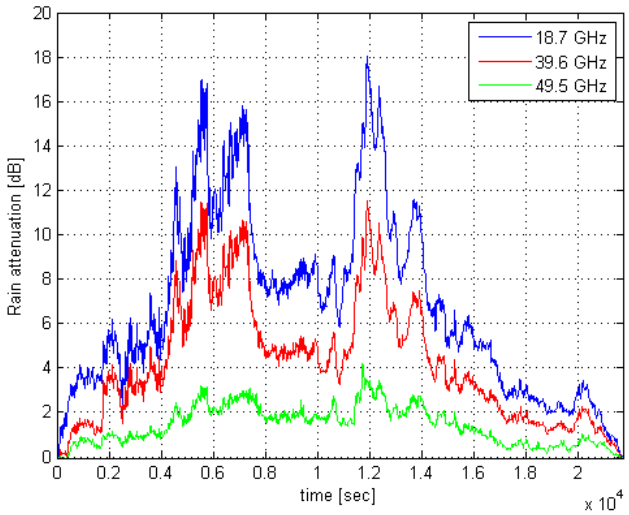

Figure 6.1: *Example of rainy event attenuation measured at 18.7(green line), 39.6(red line) and 49.5 GHz(blue line) by beacon receiver located at Spino D'Adda (09/06/1994)*

In the ITDB are collected few rain events which contain short non rainy intervals (less that 5 minutes) of negative values of rain attenuation, due to the interpolation performed in the zero-dB level procedure. To avoid negative values of rain attenuation, these samples are assumed as 0. An example of this correction is shown in Fig. 6.3.

To allow the selection of time series the entire database is subdivided in 10 classes. This procedure is performed by choosing 10 thresholds of attenuation which ensure a sufficient high number of elements in each class. Each event is classified according to its maximum value $A_{R,max}$. The generation of this classification is performed once for

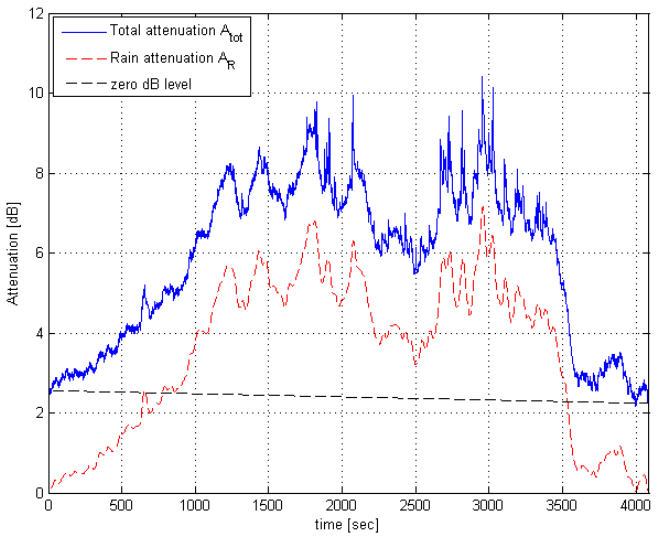

Figure 6.2: *Identification of "zero-dB level" (black dashed line) with radiometric measurement and extrapolation of rain attenuation (red dashed line) from beacon total attenuation measurement (blue line)*

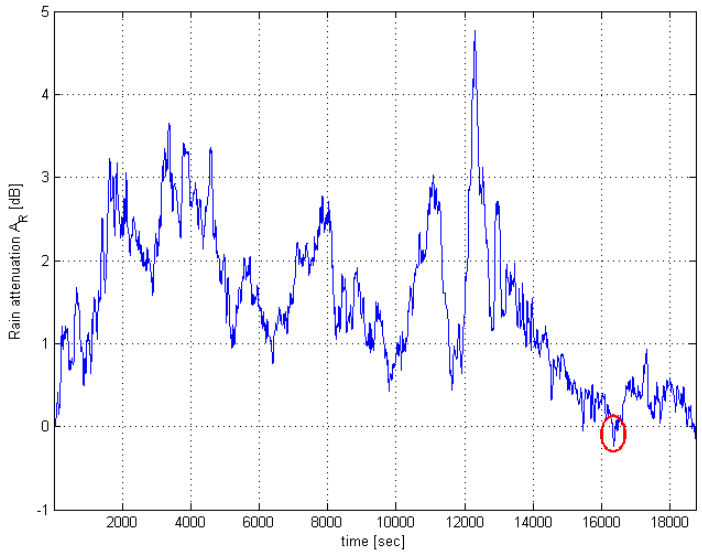

Figure 6.3: *Rain event with an interval of negative attenuation values*

all and it is independent on the simulated site. The selected class thresholds and the number of events for each class adopted for the RTSG in this thesis are reported in Tab. 6.1.

6.2.1 Rain event scaling procedure

The ITDB is assumed as input for the synthesis of rain attenuation time series at any site for middle latitude region. However, for the synthesis we can consider satcom sys-

Table 6.1: *Classification of time series of event of rain attenuation according to the maximum according to R_i classes for ITDB with rain attenuation measure at f=18.8 GHz*

	$A_R[dB]$	N° of events
R_1	22.49≤A_R<38	11
R_2	13.30≤A_R<7.87	50
R_3	7.87≤A_R<13.30	71
R_4	4.66≤A_R<7.87	170
R_5	2.76≤A_R<4.66	298
R_6	1.63≤A_R<2.76	408
R_7	0.97≤A_R<1.63	512
R_8	0.57≤A_R<0.97	578
R_9	0.34≤A_R<0.57	529
R_{10}	0≤A_R<0.34	157
TOT		2784

tems with different working frequencies (between 5 and 50 GHz) and elevation angles (between 5° and 90°). In some case, especially when we simulate satellite system with high frequency and low elevation angle, we need to scale the ITDB database in order to adapt the time series to the simulated link parameters. The scaling procedure would not be necessary since the database collects an exhaustive number of events with high variability of values. However, for satcom systems that require higher value of attenuation, above 40 dB, this procedure is mandatory and therefore it is applied to all possible scenario. The scaling procedure is obtained by multiplying each event of ITDB with a scaling factor F that is dependent on the transmitting system frequency, the elevation angle and the local rain height. Therefore, we can derive this quantity as [61]:

$$F = \frac{H_{r,1} - h_1}{H_{r,ref} - h_{ref}} \frac{\sin(\theta_{ref})}{\sin(\theta_1)} (\frac{f_1}{f_{ref}})^{1.72} \tag{6.1}$$

with H_r rain height (km), h is the height a.m.s.l. [km], θ is the elevation angle [rad] and f is the frequency [GHz] and the subscripts 1 and ref stand for the link 1 (the one we want to simulate) and the reference site of Spino D'Adda, respectively. The exponential formulation is derived from experimental measurements performed in Canada in the 1974 [61]. Since we observed that this empirical formulation come out from measurements campaign in the range of 11-18 GHz. To allow the application of this formulation up to 50 GHz, we tested it on the ITALSAT database at 18.7 in reproducing events at 39.6 and 49.5 GHz and we observed excellent results.

The scaling procedure is performed during the optimization procedure not only for scaling the ITDB but also to downscale the input CDF or rain attenuation. An example of the effect of scaling procedure is reported in Fig. 6.4. In the figure, the rain attenuation event extracted from the ITDB database is depicted in blue and in green the same event scaled for a satellite link at at f=49.5 GHz and θ=37.7°. In figure 6.5 we report an example of the downscaling of a rain attenuation CDF measured in Hemsby (UK) for a satellite link at f=49.5 GHz and θ=37.7°.

The scaling procedure of ITALSAT database has the only objective to guarantee the

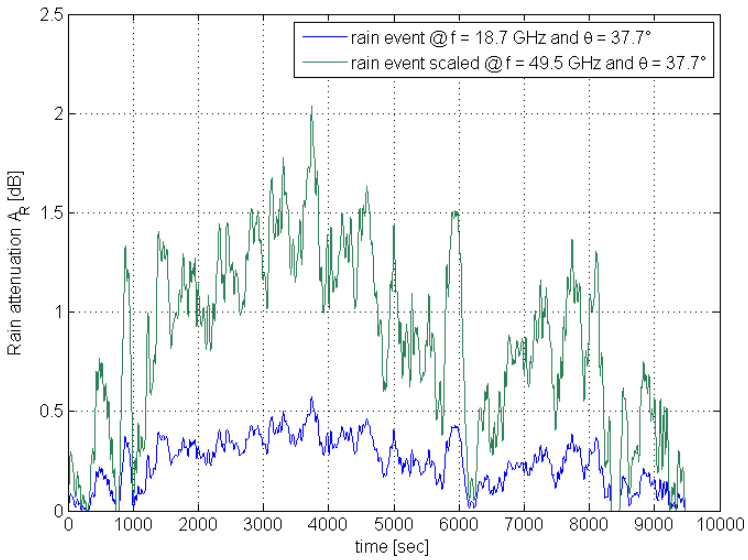

Figure 6.4: *Example of scaling procedure for the rain event collected at f=18.7 GHz and θ=37.7° and scaled to adapt for a system at f=49.5 GHz and θ=37.7°.*

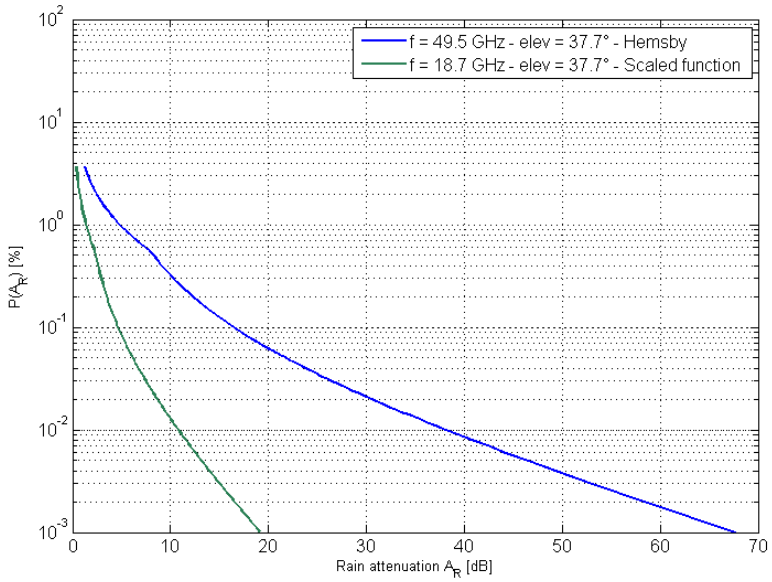

Figure 6.5: *Example of downscaling procedure for the CDF function of Hemsby at f=49.5 GHz and θ=37.7° provided by ITUR model (blue curve) with respect to the reference site of Spino D'Adda at f=18.7 GHz and θ=37.7° (green curve).*

presence of rain events with attenuation peak that cover the rain attenuation range required by the OBF. Therefore, a different formulation for scaling could be adopted to guarantee the proper generation of higher peak of rain attenuation without any implication on the performance of the model.

6.3 Structure of the time series generator

The objective of the Rainy attenuation Time Series Generator RTSG is to generate a synthetic time series of rain attenuation events to reproduce the long-term statistic of rain attenuation taken in input. The RTSG model returns an array of rain attenuation events to be properly ordered and space with no-rain period to generate a synthetic time series of rain attenuation. This procedure takes place during the composition of total attenuation time series. The algorithm return the percentage of time series to be extracted from each class of the ITDB. The identification of the number of rainy seconds to be selected from the i^{th} class is performed in an optimization procedure whose general block scheme is depicted in Fig. 6.6.

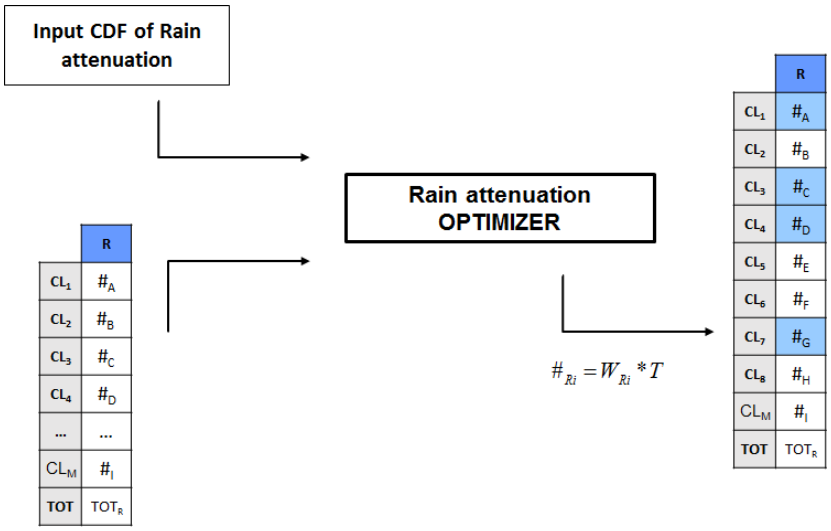

Figure 6.6: *Block scheme of rain optimization procedure.*

The system takes in input the predicted long-term statistic of rain attenuation for a specific site ('objective cdf' function (OBF)) calculated through prediction model such as ITU-R model [19] CDF or EXCELL model [62] [63]. Otherwise, the objective function can be derived by real measured data when available. The algorithm takes also in input the classified events of ITDB database and the CDF functions derived from the elements of each class (base function BF).

Then, the optimization defines how many seconds of rain attenuation must be selected from each class. In the optimization procedure we reconstruct the OBF with a function (result CDF) obtained by summing up the base functions after being adequately weighted for a set of coefficients $W_{R,i}$, one for each class. The weights $W_{R,i}$ represent how much the events collected in the i^{th} class contribute to the reconstruction of the OBF. Finally, the weights returned by the optimization are translated into number of second $\#_{R,i}$ to be selected by the i^{th} class for a total number of seconds T.

The RTSG is an improved version of the experimental measurement base model EMB presented in [64]. We mainly modified the optimization procedure including a new cost function and a different optimization constraint which takes into consideration the radio link elevation angle to provide a more accurate probability of rain on the link. In the EMB model each base function was forced to match the OBF only in the

attenuation range of its pertinence. Therefore, the attenuation range of the OBF was subdivided into 10 intervals corresponding to the peaks of the 10 classes and the i^{th} base function was force to match the OBF at the 1/4 of the attenuation interval [64]. The resulting cost function was defined over a set of 10 attenuation values. On the contrary, in RTSG model the cost function is calculated considering the entire OBF attenuation interval and not a subset of points. Furthermore, all the base functions contribute to the generation of the result CDF. For the optimization procedure we assume a Mean Squared Error MSE algorithm that allows to minimize the distance between the OBF and the result CDF by adjusting the vector of weights $W_{R,i}$. As in the generation of synthetic ILWC and IWVC time series, the distance is expressed as function of the weights:

$$d(W_{R,i}) = P(A_R)_{OBF} - P(A_R)_{REF} \tag{6.2}$$

where $P(A_R)_{OBF}$ is the OBF and $P(A_R)_{REF}$ is the result CDF, defined as:

$$P(A_R)_{REF} = \sum_{i=1}^{M} W_{R,i} P(A_R)_i \tag{6.3}$$

where $P(A_R)_i$ is the base function of the i^{th} of M class.

Differently from EMB model, in the RTSG the optimization is constrained so that the sum of weights must be equal to the probability of having rain for a Satcom system on an inclined path. This constraint ensure that the rainy events selected by ITDB do not overtake the percentage of rain time estimated for the radio link. For an inclined path the percentage of rainy time change with the elevation angle, therefore a new procedure that takes into account this effected is introduced. This constraint is expressed as:

$$\sum_{i=1}^{M} W_{R,i} = P_{0,\theta} = P_0 + \Delta P \tag{6.4}$$

where:

- $P_{0,\theta}$ is the percentage of rain time for the inclined path;
- θ is the elevation angle;
- $P_0 = P(R > 0)$ is the percentage of time with rain rate R>0 mm/h evaluated for the zenith path;
- ΔP is the difference due to the inclined path.

The probability of rain P_0 can be approximated as $P_0(Lat, Lon)$ derived from Recommendation ITU-R P.837 [50]. To quantify the difference of probability ΔP of rain time induced by the inclined path we make two assumptions: we assumed that all rain events detected within an year are all of equal length and that the velocity of cloud is equal to the annual average wind speed derived at 700 hPa isobar extracted from the European Center for Medium-range Weather Forecast ECMWF ERA-40 meteorological database [65] (v = 8.87 [m/s]) that we assume as constant.

Let's defined the time probability of rain as:

$$P_0 = 100 * \frac{N t_0}{T_0} \tag{6.5}$$

where N is the number of rain events, t_0 the time each rain event last over the antenna pointed towards the zenith and T_0 the total number of hours within the year. Then we calculate the increment of the rainy time for each rain event due to the inclined path. For the inclined path shown in Fig. 6.7, the time t_0 [h] that a rain event is seen from the beacon antenna is increased of a Δt defined as:

$$\Delta t = \frac{L_{path}}{v} \tag{6.6}$$

with v the wind velocity and L_{path} the horizontal projection length of the inclined path. This length is given by:

$$L_{path} = \frac{H_r}{\tan(\theta)} \tag{6.7}$$

with H_r the rain height [km].

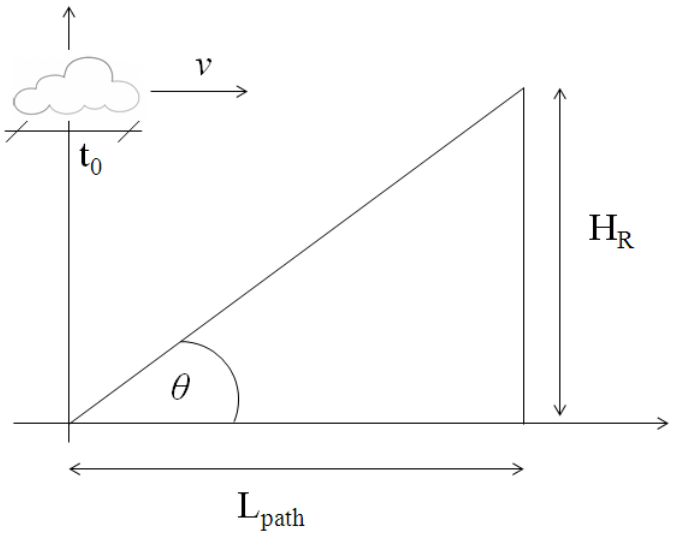

Figure 6.7: *Schematic presentation of an Earth-space path giving the parameters to be used to evaluate the P_0 increment.*

The probability of rain time $P_{0,\theta}$ is therefore defined as:

$$P_{0,\theta} = 100 * (t_0 + \Delta t)\frac{N}{T_0} = P_0(1 + \frac{\Delta t}{t_0}) \tag{6.8}$$

We assume that all rain events have a duration of 1 hour since we observed that the average length of a rain attenuation events collected in the ITDB is about 1 hour. The $P_{0,\theta}$ can be rewrite as follows:

$$P_{0,\theta} = P_0(1 + \frac{H_r}{\tan(\theta)v}) \tag{6.9}$$

The P_0 quantities must be specified as input to the optimization procedure.

Then, once the optimization procedure is completed, the set of weights is translated into the number of seconds to be selected from each class. The number of selected seconds for the i^{th} class is defined as:

$$\#_{R,i} = W_{R,i} * T \tag{6.10}$$

where T is the total number of second within year.

Finally, the rain attenuation events are selected randomly in each class of ITDB database. The random selection allows the RTSG to generate, for the same simulation setup and therefore, for the same optimized set of weights, different replicas of synthetic time series. An example of synthetic CDF functions for the frequency at 20 and 50 GHz ad elevation angle θ=37.7 $^\circ$ is depicted in Fig. 6.8. For each OBF (red curves) we have simulated 3 replicas one year long (blue curves). All the replicas are quite coincident for probability levels above 0.1 % while become dissimilar for lower probabilities, as expected.

Moreover, despite the negative values in the time series have been set to zero, these samples are included into the calculation of rainy seconds selected from each class. However, their percentage is reasonably small, i.e. for the satcom system in Fig. 6.8 (a) we have a P_0=3.51% and a $P_{0,\theta}$= 3.8123% with included $P(A_R = 0)$=0.11 % that is sufficiently lower than the ΔP = 0.3023 %.

6.4 Rainy time series validation

The testing of the rain attenuation time series generation is performed with respect to first order statistics (rain attenuation CDF) and second order statistics (fade duration and fade slope) in agreement with Recommendation ITU-R 311-14 [66]. The goal of the validation is to evaluate the ability of the RTSG model to generate the OBF used as input to the model and then to investigate in detail the dynamic behaviour of the time varying channel (second order statistic validation).

The test is carried out making use of a set of experimental data collected by the Study Group 3 into the ITU-R concerning the tropospheric propagation (DBSG5 database [67]). This database collects several worldwide experimental measurements to support the evaluation of prediction methods and time series synthesizers. In particular for our validation we consider for DBSG5 [66]:

- Slant path annual rain attenuation and rain rate statistics
- Slant path fade duration statistics
- Slant path fade slope statistics

This database collects measurements for experiments with radio-link with elevation angle from 6° till 83° and frequency up to 35 GHz. To enlarge the validation of the model to a range of frequency up to 50 GHz we consider the measurements of rain attenuation collected during ITALSAT experiment at 39.6 and 49.5 GHz at 37.7° of elevation angle. From this database we extrapolate the information of fade slope and fade duration.

As term of comparison for the RTSG performance, we test the tropospheric time series synthesizer described in Recommendation ITU-R 1853-0 [68], here called ITU-R model. This model, presented in section 3.4.1, generates a time series of rain attenuation and scintillation for terrestrial and Earth-space paths. For both RTSG and ITU-R synthesizers we generate a time series of one year length.

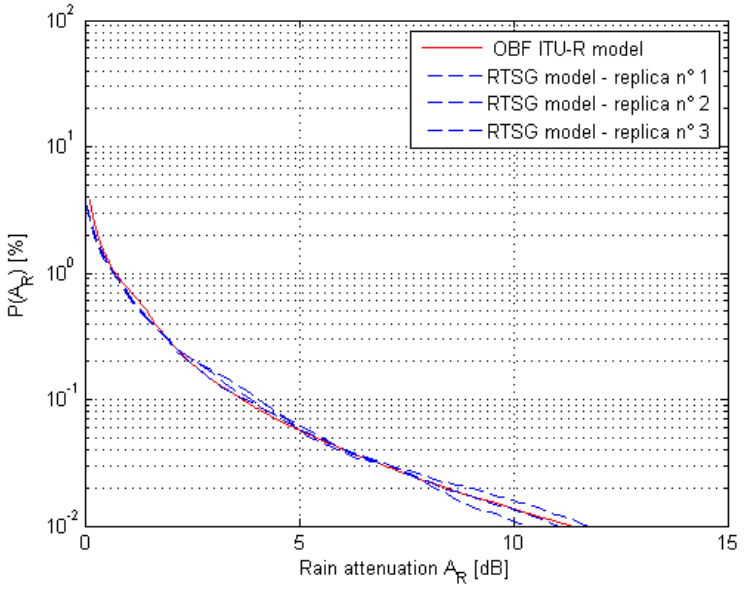

(a)

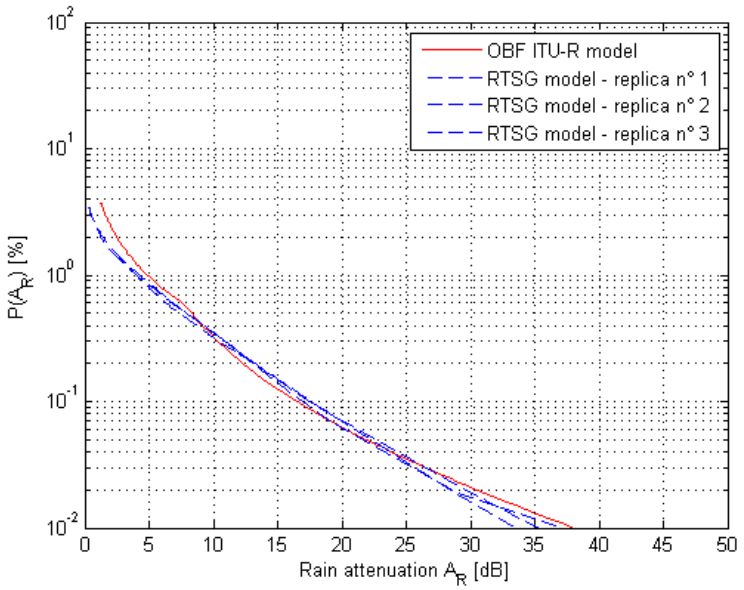

(b)

Figure 6.8: *Simulation results for Hembsy (UK) for two simulated f=20 GHz (a) and f=50 GHz (b) and elevation angle θ=37.7 °.*

6.4.1 First order statistic validation

In the first order statistic validation we investigate the comparison of the rain attenuation generated by the RTSG and ITU-R models with the measured data provided by the DBSG5 database. The figure of merit for this assessment, reported in [66], is the ratio of predicted and measured attenuation values made for fixed probability levels, i.e. for each percentage of time P we considered. The resulting formula is:

$$\epsilon(P) = \begin{cases} 100(\frac{A_{m,i}(P)}{10})^{0.2} \ln(\frac{A_{p,i}(P)}{A_{m,i}(P)}), & A_{m,i} < 10 \text{ dB} \\ 100 \ln(\frac{A_{p,i}(P)}{A_{m,i}(P)}), & A_{m,i} \geq 10 \text{ dB} \end{cases} \tag{6.11}$$

where $A_{p,i}$ is the predicted attenuation [dB] and $A_{m,i}$ is the measured attenuation [dB] for the i^{th} radio link. The natural logarithm of the ratio used as test variable is weighted for the lower values of A_m (minor than 10 dB) in order to reduce the negative effects introduced by measurements inaccuracies and contribution of attenuation of sources other than rain.

Both the measured and synthetic CDF are evaluated for fixed probability level as 'standard' vector suggested by ITU-R P = [0.01 0.02 0.03 0.05 0.1 0.2 0.3 0.5 1.0 %]. We select from the DBSG5 database 48 sites for a total of 136 experiment with a duration of minimum 263 days (the majority have 1 year length) for a total of almost 190 years. The considered experimental frequencies are between 6.2 and 34.5 GHz and the elevation angles range between 6.5° and 72.8°. A complete list of experiment information setup is reported in Tab.6.2 and in Tab. 6.3.

Table 6.2: *Main DBSG5 database information for first order statistic analysis.*

System information	
Frequency range	6.2-34.5 GHz
Elevation angle range	6.5-72.8°
Absolute latitude range	0-90°
Probability range	0.001-1 %
Number experiments	136
Total time	187.5 years

Table 6.3: *List of sites collected in DBSG5 database and considered for the first order statistic validation*

SITE	LAT(°N)	LONG (°E)	FREQ (GHz)	ELEV(°)	PERIOD (days)
WALTHAM	42.4	288.7	11.7	24	365x2
WALTHAM	42.4	288.7	19	35.5	365
WALTHAM	42.4	288.7	19	38.5	365
WALTHAM	42.4	288.7	28.6	38.5	365
HOLMDEL	40.4	285.9	11.7	27	365x2
HOLMDEL	40.4	285.9	19	18.5	700
HOLMDEL	40.4	285.9	19	38.6	365x2
HOLMDEL	40.4	285.9	28.6	38.6	365
CLARKSBURG	39.2	282.7	19	21	365
CLARKSBURG	39.2	282.7	19	41	365
CLARKSBURG	39.2	282.7	19	43.5	780
CLARKSBURG	39.2	282.7	28.6	21	365
CLARKSBURG	39.2	282.7	28.6	41	365
CLARKSBURG	39.2	282.7	28.6	43.5	780
GREENBELT	38.5	283	11.7	29	365x3
WALLOPS IS	37.8	284.5	28.6	41.6	365
WALLOPS IS	37.8	284.5	28.6	44.5	365x2
BLACKSBURGn1	37.2	279.5	11.7	33	334+365

BLACKSBURG$n1$	37.2	279.5	11.6	10.7	365x3
BLACKSBURG$n1$	37.2	279.5	28.6	45	334
BLACKSBURG$n1$	37.2	279.5	28.6	46	365
AUSTIN	30.4	262.3	11.7	50	365x3
AUSTIN	30.4	262.3	19	52	701
AUSTIN	30.4	262.3	28.6	52	670
BLACKSBURG$n2$	37.2	279.5	11.6	10.7	365
BLACKSBURG$n3$	37.2	279.5	12.5	14	365
BLACKSBURG$n3$	37.2	279.5	19.77	14	365
BLACKSBURG$n3$	37.2	279.5	29.66	14	365
ALBERTSLUND	55.68	12.36	14.5	26.5	365
ALBERTSLUND	55.68	12.36	11.8	26.5	365+366
MARTLESHAM	52.1	1.3	11.8	29.9	365x5
NEDERHORST	52.2	5.1	11.6	30	365+366
SLOUGH	51.5	359.5	11.6	29.5	1096
LEEHEIM	49.9	8.3	11.8	32.9	355+356+343
LEEHEIM	49.9	8.3	11.6	32.9	356
GOMETZ	48.7	2.1	11.6	32	365
GOMETZ	48.7	2.1	11.6	33.6	365
GOMETZ	48.7	2.1	11.8	33.6	365
GOMETZ	48.7	2.1	14.5	33.6	365
MUNICH	48.2	11.6	11.6	29	365
LARIO	46.2	9.4	11.6	32	340x4+341
LARIO	46.2	9.4	17.8	32	340x3
SPINO D'ADDA	45.4	9.5	11.6	32	360+359x3
FUCINO	42	13.6	11.6	33.3	359x7+360x2
SODANKYLA	67.4	26.6	11.6	13.2	366+365
SODANKYLA	67.4	26.6	11.6	12.5	365+304
KIRKKONUMMI	60.2	24.4	11.8	20.6	731
STOCKHOLM	59.3	18.1	14.5	22.4	365
STOCKHOLM	59.3	18.1	11.8	22.4	365x2
LUSTBUEHEL	47.1	15.5	11.6	35.2	365x3
BERN	47	7.5	11.6	36	365+366
SPINO D'ADDA	45.4	9.5	18.68	37.7	365
DUBNA	56.7	37.33	11.5	12	365x3
MIEDZESZYN	52.5	21.18	11.5	23	365x3
MIEDZESZYN	52.25	21	12.5	20.52	366
LOUVAIN-LA-NEUVE	50.67	4.62	12.501	27.8	357
LOUVAIN-LA-NEUVE	50.67	4.62	29.656	27.8	280
AVEIRO	40.65	351.1	12.501	40	275
AVEIRO	40.65	351.1	19.77	40	262
SPARSHOLT	51.8	358.61	12.5	29.2	329
SPARSHOLT	51.8	358.61	19.77	29.2	329
SPARSHOLT	51.8	358.61	20.7	28	365x2
CHILTON	51.5667	358.72	29.656	28.56	363
CHILBOLTON	51.13	358.57	20.7	28	365x2
DUNDEE	56.45	357.02	20.7	23.29	365
WAKKANAI	45.4	141.7	12.1	29.1	365
WAKKANAI	45.4	141.7	19.5	37	365
SENDAI	38.2	140.5	19.5	45	366
KASHIMA	35.6	140.7	11.5	47	730

KASHIMA	35.6	140.7	34.5	47	365
KASHIMA	35.6	140.7	11.7	37	943
YOKOHAMA	35.2	139.4	19.5	48	731
YOKOSUKA	35.1	139.4	19.5	48	731
YAMAGAWA	31.2	130.6	12.1	47.3	366
YAMAGAWA	31.2	130.6	19.5	53	365
KLANG	3.1	101.4	11.8	45	731
YAMAGUCHI	34.1	131.6	11.5	6.5	365
NEYAGAWA	35.75	135.64	19.45	49.5	7305
NEYAGAWA	35.75	135.64	11.84	41.5	6575
EAR	-0.2	100.32	14.47	39.3	1096
EAR	-0.2	100.32	12.4	39.3	1096
BEIJING	39.6	116.2	11.5	20.5	425
UNITECH LAE	-6.45	147	12.69	72.8	$360x2$
SURABAYA	-7.15	122.44	11.198	14.1	361
SURABAYA	-7.15	122.44	11.198	20.2	356+364
TOWNSVILLE	-19.3332	144.7567	11.198	45.3	365

The testing of RTSG model is carried out by comparing the CDF derived from synthetic time series of RTSG and ITU-R model. Both models take in input the measured rain attenuation CDF reported in DBSG5 and return the synthesize CDF calculated from synthetic time series of rain attenuation. They also require in input the probability of rain time P_0 provided by [50].

To evaluate the performance of RTSG and ITU-R model in each experiment three quantities are defined as dependent from the considered probability level [28]: an average, root mean square (RMSE) and sigma error. Assuming $\epsilon_{A_R}(i, P)$ the error in the i^{th} of N experiments evaluated for the P^{th} of M probability level and assuming $T(i)$ as the duration of the i^{th} experiment, we can evaluate the mean error the root mean square error and the sigma error of the P^{th} probability level as:

$$< \epsilon_{A_R}(P) >= \frac{\sum_{i=1}^{N} \epsilon_{A_R}(i, P)T(i)}{\sum_{i=1}^{N} T(i)} \tag{6.12}$$

$$rms_{\epsilon_{A_R}}(P) = \sqrt{\frac{\sum_{i=1}^{N} \epsilon_{A_R}^2(i, P)T(i)}{\sum_{i=1}^{N} T(i)}} \tag{6.13}$$

$$\sigma_{\epsilon_{A_R}}(P) = \sqrt{(rms_{\epsilon_{A_R}}(P))^2 - < \epsilon_{A_R}(P) >^2} \tag{6.14}$$

The total error is evaluated considering all N experiments at all M probability levels. Assuming $T(P)$ as the sum of the duration of all experiments available at the probability P, the total mean, root mean square and sigma error are expressed as:

$$< \epsilon_{TOT,A_R} >= \frac{\sum_{P=1}^{M} \epsilon_{A_R}(P)T(P)}{\sum_{p=1}^{M} T(P)} \tag{6.15}$$

$$rms_{\epsilon_{TOT,A_R}} = \sqrt{\frac{\sum_{P=1}^{M} \epsilon_{A_R}^2(P)T(P)}{\sum_{p=1}^{M} T(P)}} \tag{6.16}$$

$$\sigma_{\epsilon_{TOT,A_R}} = \sqrt{(rms_{\epsilon_{A_R}})^2 - < \epsilon_{A_R} >^2} \tag{6.17}$$

In Tab. 6.4 are reported the errors of RTSG and ITU-R for different probability levels. The RTSG is more effective in reproducing the attenuation values for higher probability levels. Tab. 6.5 summarizes the overall performance of both models and highlight the ability of RTSG model in reproducing the OBF received in input with a RMSE of about 15 % with respect to a RMSE of about 27 % reported for the ITU-R model. These RMSE are acceptable if we consider that the year-to-year variability of rain attenuation is around 20-30 %.

Table 6.4: *Average errors for RTSG and ITU-R models for different probability levels for DBSG5 database*

Probability [%]	System	$< \epsilon_{A_R} >$ [%]	$rms_{\epsilon_{A_R}}$ [%]	$\sigma_{\epsilon_{A_R}}$ [%]
0.001	RTSG	-16.2	30.3	25.6
	ITU-R	-19.9	55.0	51.2
0.002	RTSG	-22.8	40.0	32.8
	ITU-R	-7.9	47.0	46.4
0.003	RTSG	-23.0	35.4	26.9
	ITU-R	-7.9	51.3	50.7
0.005	RTSG	-12.1	27.5	24.7
	ITU-R	-6.2	44.0	43.5
0.01	RTSG	-8.0	19.9	18.3
	ITU-R	4.6	36.2	35.9
0.02	RTSG	-3.2	13.7	13.3
	ITU-R	3.6	29.0	28.7
0.03	RTSG	-0.3	11.0	11.0
	ITU-R	2.2	24.9	24.8
0.05	RTSG	2.5	8.8	8.4
	ITU-R	0.9	20.4	20.4
0.1	RTSG	3.7	10.7	10.0
	ITU-R	-0.8	17.6	17.6
0.2	RTSG	3.4	8.6	7.9
	ITU-R	-4.7	15.9	15.2
0.3	RTSG	1.2	6.6	6.5
	ITU-R	-8.2	17.1	15.0
0.5	RTSG	0.2	8.9	8.9
	ITU-R	-12.5	18.9	14.1
1.0	RTSG	-4.7	17.9	17.2
	ITU-R	-21.4	28.2	18.3

Finally, the database of rain attenuation at 49.5 GHz at Spino D'Adda for 7 years (1994-2000) is assumed as input CDF for RTSG and ITU-R model. We perform the simulation considering the CDF of each single year. We observed from Tab. 6.6 and 6.7 that RTSG model is effective also for the synthesis of time series at frequency between

Table 6.5: *Total errors for RTSG and ITU-R models for DBSG5 database*

System	$< \epsilon_{TOT,A_R} > [\%]$	$rms_{\epsilon_{TOT,A_R}} [\%]$	$\sigma_{\epsilon_{TOT,A_R}} [\%]$
RTSG	-1.9	15.3	15.1
ITU-R	-3.7	26.8	26.6

40 and 50 GHz (total RMSE of 18 %), while ITU-R model is affected by an higher RMSE (about 45%).

Table 6.6: *Average errors for RTSG and ITU-R models for a subset of probability levels for database at 49.5 GHz*

Probability [%]	System	$< \epsilon_{A_R} > [\%]$	$rms_{\epsilon_{A_R}} [\%]$	$\sigma_{\epsilon_{A_R}} [\%]$
0.01	RTSG	31.5	37.9	21.2
	ITU-R	32.4	58.5	48.7
0.03	RTSG	5.5	10.0	8.3
	ITU-R	1.7	38.9	38.8
0.05	RTSG	4.1	12.1	11.4
	ITU-R	-11.7	34.0	31.9
0.1	RTSG	5.7	12.7	11.3
	ITU-R	-24.0	31.3	20.0
0.3	RTSG	7.6	14.2	12.0
	ITU-R	-42.3	45.1	15.5
0.5	RTSG	8.5	13.5	10.5
	ITU-R	-48.2	50.1	13.6
1.0	RTSG	8.5	17.6	15.4
	ITU-R	-50.3	51.7	12.0

Table 6.7: *Total errors for RTSG and ITU-R models for database at 49.5 GHz*

System	$< \epsilon_{A_R} > [\%]$	$rms_{\epsilon_{A_R}} [\%]$	$\sigma_{\epsilon_{A_R}} [\%]$
RTSG	9.7	17.8	15.0
ITU-R	-18.7	44.8	40.7

6.4.2 Fade duration validation

The Fade Duration FD is the time interval between two crossings above the same attenuation threshold (fade threshold) [69]. An example of the fade duration is reported in Fig. 6.9. It is an important parameter to be considered during the design of satellite system since:

- it gives the number and the duration of the outages and therefore the system unavailability;
- it gives information about the statistical duration of an event that can be useful for operators to allocate resources among users;

- it can be useful for the determination of the proper forward error correction code and modulation.

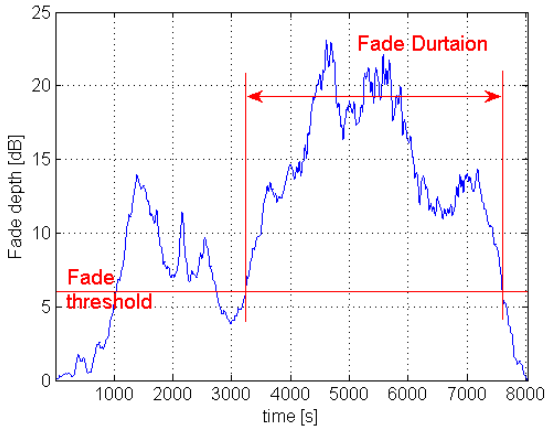

Figure 6.9: *An example of fade duration for a rainy event.*

There are two different formulations for the FD:

1. $P(d > D|a > A)$ is the probability of occurrence of fades of duration d longer than D [s], given that the attenuation a is grater than A [dB];
2. $F(d > D|a > A)$ is the cumulative exceedance probability due to fade of duration d longer than D [s], given that the attenuation a is grater than A [dB];

Fade duration statistics are evaluated from the obtained time series according to:

$$F(A/D) = \frac{N_S(D)}{N_{TOT}} \tag{6.18}$$

where $N_S(D)$ is the total time the attenuation A [dB] is exceeded composed of intervals longer than D [s] and N_{TOT} the total time the attenuation A is exceeded. The figure of merit for fade duration analysis reported in the last Recommendation ITU-R 311-14 [66] is:

$$\epsilon_{FD}(D, A) = \ln(\frac{100 - F_p(d > D|a > A)}{100 - F_m(d > D|a > A)}) \tag{6.19}$$

where F_p is the predicted and F_m is the measured probability of fade duration computed for the considered experimental radio link.

For this analysis we consider the DBSG5 database of fade duration statistics that collects 66 experiments from 41 sites. The main information of the database are reported in Tab. 6.8 while the list of considered sites with the principal information for each experiment are reported in Tab. 6.9. In the database, the CDF of durations are stored for values of durations D = [6, 10, 18, 60, 180, 600, 1800, 3600] [s] and thresholds of attenuation A =[3, 5, 6, 10, 15, 20, 25] [dB].

Table 6.9: *List of sites collected in DBSG5 database and considered for the first order statistic validation*

SITE	LAT(°N)	LONG (°E)	FREQ (GHz)	ELEV(°)	PERIOD (days)
LAKE COWICHAN	48.8	235.96	13.0	33.0	1071
CLARKSBURG CMST1	39.2	282.7	19.0	21.0	365x2
CLARKSBURG CMST2	39.2	282.7	19.0	41.0	365x2
CLARKSBURG CMST1	39.2	282.7	28.6	21.0	730
CLARKSBURG CMST2	39.2	282.7	28.6	41.0	365
MELVILLE SASK.	50.6	257.0	13.0	31.0	922
THUNDER BAY ONT.	48.4	270.6	13.0	30.0	467
OTTAWA ONT.	45.4	284.1	13.0	26.0	613
MILL VILLAGE NS	44.5	295.5	13.0	20.0	1793
ALLAN PARK ONT.	44.2	279.1	13.0	29.0	628
MANAUS	-3.13	299.98	12.0	83.08	655
RIO DE JANEIRO	-22.92	316.5	12.0	53.87	517+359
BELEM	-1.45	311.52	12.0	70.53	623
PONTA DAS LAGES	-3.1	300.1	12.0	82.97	333
BRASILIA	-15.8	312.17	12.0	62.88	331
LEEHEIM	49.9	8.4	11.4	33.0	1520
LEEHEIM OTS	49.9	8.4	11.6	32.9	1054
LARIO SIRIO	46.2	9.0	11.6	32.0	1362
SPINO DADDA SIRIO	45.4	9.5	11.6	32.0	1359
FUCINO	42.0	13.6	11.4	42.0	1520
FUCINO SIRIO	42.0	13.6	11.6	33.3	1436
FUCINO OTS	42.0	13.6	11.8	42.0	1096
STOCKHOLM	59.3	18.1	11.4	21.0	2555
STOCKHOLM OTS	59.3	18.1	11.8	22.4	0365
LUSTBUEHEL OTS	47.1	15.5	11.6	35.2	1461
LEUK	46.3	7.6	11.4	35.0	730
MILANO	45.5	9.4	11.4	37.0	730
MILO	38.0	12.6	11.4	46.0	730
MILO OTS	38.0	12.6	11.8	48.0	1461
PORTO	41.2	-8.6	11.4	40.0	1095
VILLAFRANCA	40.5	356.0	11.8	41.0	731
GRAZ	47.1	15.5	11.4	37.0	2196
DUBLIN OTS	53.4	353.7	11.8	27.0	1096
EUT#1 OLYMPUS	51.45	-5.49	12.5	26.74	213+314+ 358+910
EUT#2 OLYMPUS	51.45	-5.49	19.7	26.74	215x2+304+ 306+357x2+ 900+903
EUT#3 OLYMPUS	51.45	-5.49	29.6	26.74	216+319+ 327+ 80+615
Albertslund#1 OLYMPUS	55.68	12.36	19.77	20.7	350+353+ 346
MARUGAME	34.3	133.7	11.9	6.0	365
MARUGAME	34.3	133.7	11.9	15.0	365
MARUGAME	34.3	133.7	11.9	45.0	365
DARWIN#1	-12.0	130.0	11.1	60.0	458
DARWIN#1	-12.0	130.0	14.2	60.0	458
INNISFAIL	-17.0	146.0	11.1	45.0	539
CLAYTON	-37.0	9.0	11.1	45.0	354

CLAYTON	-37.0	9.0	14.2	45.0	936
CLAYTON	-37.0	9.0	11.1	15.0	354
JAMES COOK	-19.33	146.75	11.1	45.3	365

Fig. 6.10 shows the result of the measured and predicted fade duration CDF (for both RTSG and ITU-R model) for a single site (EUT#2 OLYMPUS) at frequency 19.7 GHz and elevation angle 26.7° for the attenuation thresholds of 3,6,10 and 15 dB and durations D from 1 to 3600 s.

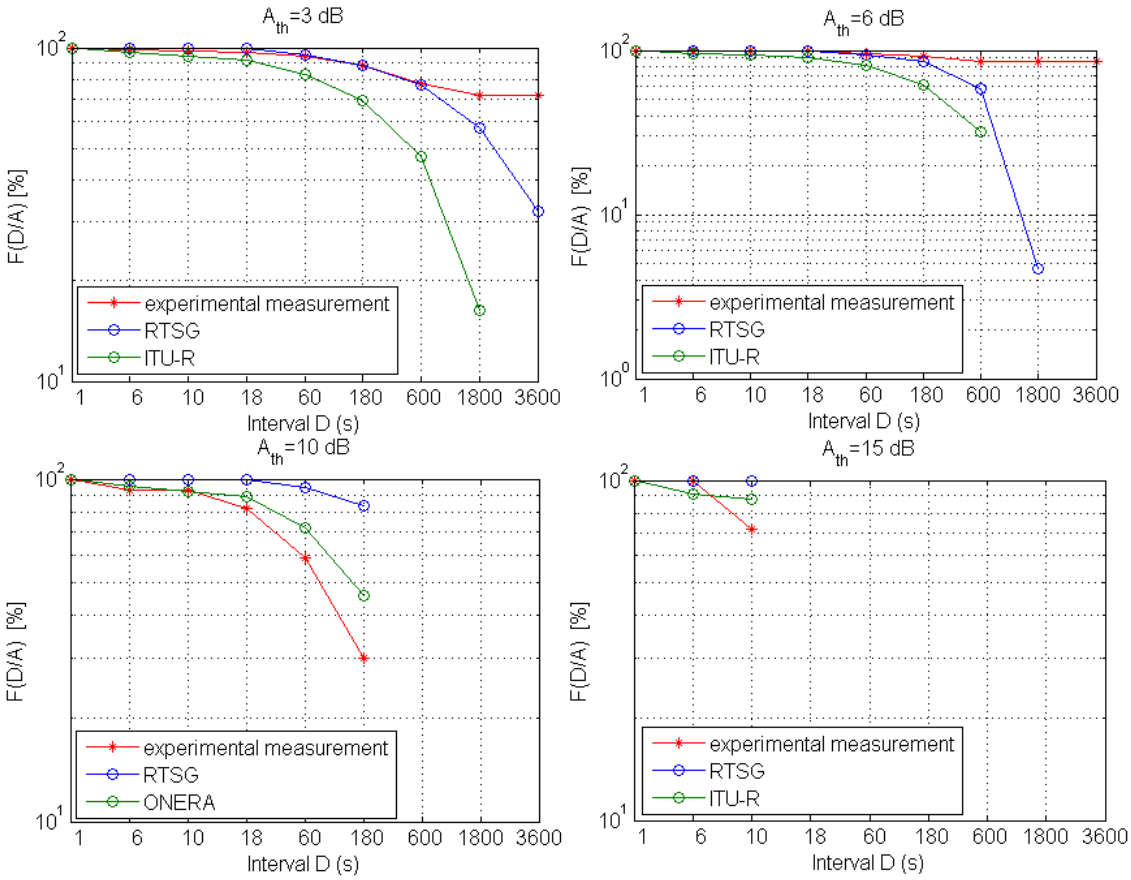

Figure 6.10: *Fade duration CDF for a single site (EUT#2 OLYMPUS) at frequency 19.7 GHz and elevation angle 26.7° for 4 thresholds of attenuation [3,6,10 and 15 dB].*

Tab. 6.10 gives the RMSE $rms_{\epsilon_{TOT,FD}}$ error for different thresholds of attenuation A and duration D averaged over all sites. The RTSG model suffer for a strong overestimation of FD for duration up to 60 s, this error is slightly decreasing with the increment of A thresholds. This is probably due to the fact that RTSG model do not include the synthesis of scintillations. According to [64] and [70], FD is mainly influenced by slow fluctuation (rain events above 60 s) and fast fluctuation (tropospheric turbulence below 60 s). This hypothesis is confirmed when the error of FD is evaluated for duration higher than 60 s: the performance of RTSG and ITU-R models are almost comparable.

Tab.6.11, 6.12 and 6.13 report the mean $< \epsilon_{TOT,FD} >$, RMSE $rms_{\epsilon_{TOT,FD}}$ and sigma $\sigma_{\epsilon_{TOT,FD}}$ errors evaluated at fixed values of duration and averaged over attenuation thresholds and sites. The RTSG average error over attenuation thresholds exhibit

Table 6.8: *Main DBSG5 database information for fade duration analysis*

System information	
Frequency range	11.1-29.7 GHz
Elevation angle range	6.0-83°
Absolute latitude range	0-90°
Number experiments	66
Total time	125.6 years

Table 6.10: *Fade duration $rms_{\epsilon_{FD}}$ error for different duration D and attenuation thresholds A for RTSG and ITU-R models*

		duration D [s]							
		6	10	18	60	180	600	1800	3600
3 [dB]	RTSG	4.786	3.567	2.323	1.085	0.801	0.547	0.592	0.595
	ITU-R	1.213	0.921	1.400	1.401	0.706	0.667	0.739	0.682
5 [dB]	RTSG	4.515	3.599	2.554	1.282	0.696	0.635	0.947	1.201
	ITU-R	1.349	1.141	1.118	1.253	0.975	0.898	0.997	1.240
6 [dB]	RTSG	4.155	3.286	2.079	1.044	0.771	0.679	1.077	1.016
	ITU-R	1.449	1.201	1.479	1.511	0.978	0.836	1.080	1.044
10 [dB]	RTSG	4.286	4.056	2.182	1.260	0.973	0.565	0.256	0.288
	ITU-R	1.286	1.166	1.316	1.458	0.898	0.540	0.219	0.327
15 [dB]	RTSG	4.394	3.267	2.504	1.314	1.264	0.626	0.237	0.025
	ITU-R	1.755	1.575	1.514	1.680	1.656	0.732	0.237	0.117
20 [dB]	RTSG	3.524	3.543	3.164	1.128	1.184	0.777	-	0.211
	ITU-R	2.014	2.027	2.124	1.716	1.71	4 0.744	-	0.211
25 [dB]	RTSG	3.181	2.584	2.009	1.496	1.864	1.784	-	-
	ITU-R	2.321	2.204	2.095	2.076	2.051	1.798	-	-

an overestimation of FD for values below 60 s. Furthermore, in Tab. 6.14 and Tab. 6.15 the total $\epsilon_{TOT,FD}$ error averaged over attenuation, duration and sites are reported.

Table 6.11: *Mean fade duration $< \epsilon_{TOT,FD} >$ error for different duration D averaged attenuation thresholds A for RTSG and ITU-R models*

	duration D [s]							
	6	10	18	60	180	600	1800	3600
RTSG	-3.580	-2.827	-1.794	-0.140	0.006	0.128	0.276	0.377
ITU-R	0.758	0.680	0.885	1.075	0.735	0.486	0.488	0.542

Finally, the fade duration statistic is validated with the use of ITALSAT measurements collected for 7 years in Spino D'Adda at 39.6 and 49.5 GHz at 37.7°. This database is taken into account to assess RTSG model ability for the synthesis of time series at frequency between 40 and 50 GHz. Fig. 6.11 shows clearly that the FD statistic of the ITDB at 18.7 GHz, that is used as input to RTSG model, is different from the one obtained at 39.6 and 49.5 GHz. Therefore the validation of the model through

Table 6.12: *RMSE fade duration $rms_{\epsilon_{TOT,FD}}$ error for different duration D averaged attenuation thresholds A for RTSG and ITU-R models*

	duration D [s]							
	6	10	18	60	180	600	1800	3600
RTSG	4.314	3.489	2.379	1.200	1.034	0.740	0.827	0.864
ITU-R	1.538	1.479	1.513	1.519	1.224	0.839	0.881	0.911

Table 6.13: *Sigma fade duration $\sigma_{\epsilon_{TOT,FD}}$ error for different duration D averaged attenuation thresholds A for RTSG and ITU-R models*

	duration D [s]							
	6	10	18	60	180	600	1800	3600
RTSG	2.407	2.045	1.562	1.192	1.034	0.729	0.779	0.777
ITU-R	1.338	1.314	1.228	1.074	0.979	0.683	0.733	0.732

Table 6.14: *Fade duration total error $\epsilon_{TOT,FD}$ averaged over duration D and attenuation thresholds A for RTSG and ITU-R models for duration grater than 6 s*

	$< \epsilon_{TOT,FD} >$	$rms_{\epsilon_{TOT,FD}}$	$\sigma_{\epsilon_{TOT,FD}}$
RTSG	-0.9442	1.8558	1.3156
ITU-R	0.7062	1.2381	1.0101

Table 6.15: *Fade duration total error $\epsilon_{TOT,FD}$ averaged over duration D and attenuation thresholds A for RTSG and ITU-R models for duration grater than 60 s*

	$< \epsilon_{TOT,FD} >$	$rms_{\epsilon_{TOT,FD}}$	$\sigma_{\epsilon_{TOT,FD}}$
RTSG	0.12955	0.9328	0.90214
ITU-R	0.66531	1.0748	0.84024

these two databases is quite significant.

Fig. 6.12 shows the results of the measured and predicted fade duration CDF of a single year (2000) for a Spino D'Adda at frequency 49.5 GHz for the attenuation thresholds of 3,6,10 and 20 dB and durations D from 1 to 3600 s. In Tab. 6.16, 6.17 and 6.18 the mean, RMSE and sigma error of FD for different duration averaging over attenuation thresholds are reported. In these cases the FD statistics of RTSG show small error also for lower durations (below 60 s) since the database at 39.6 and 49.5 GHz was previously filtered to remove scintillations. On the contrary ITU-R model below 60 s shows increased error since the generated time series include scintillation.

Finally the overall performance are shown in Tab. 6.19 and 6.20. These results evidence an higher ability of RTSG model in reproducing FD statistics also for satcom systems transmitting at frequency ranges between 40 and 50 GHz. The input database was filtered to remove scintillation effects, therefore the RTSG model shows good results also for duration shorter than 60 seconds. On the contrary, for this range of duration, ITU-R model that takes into account scintillation shows worst performance.

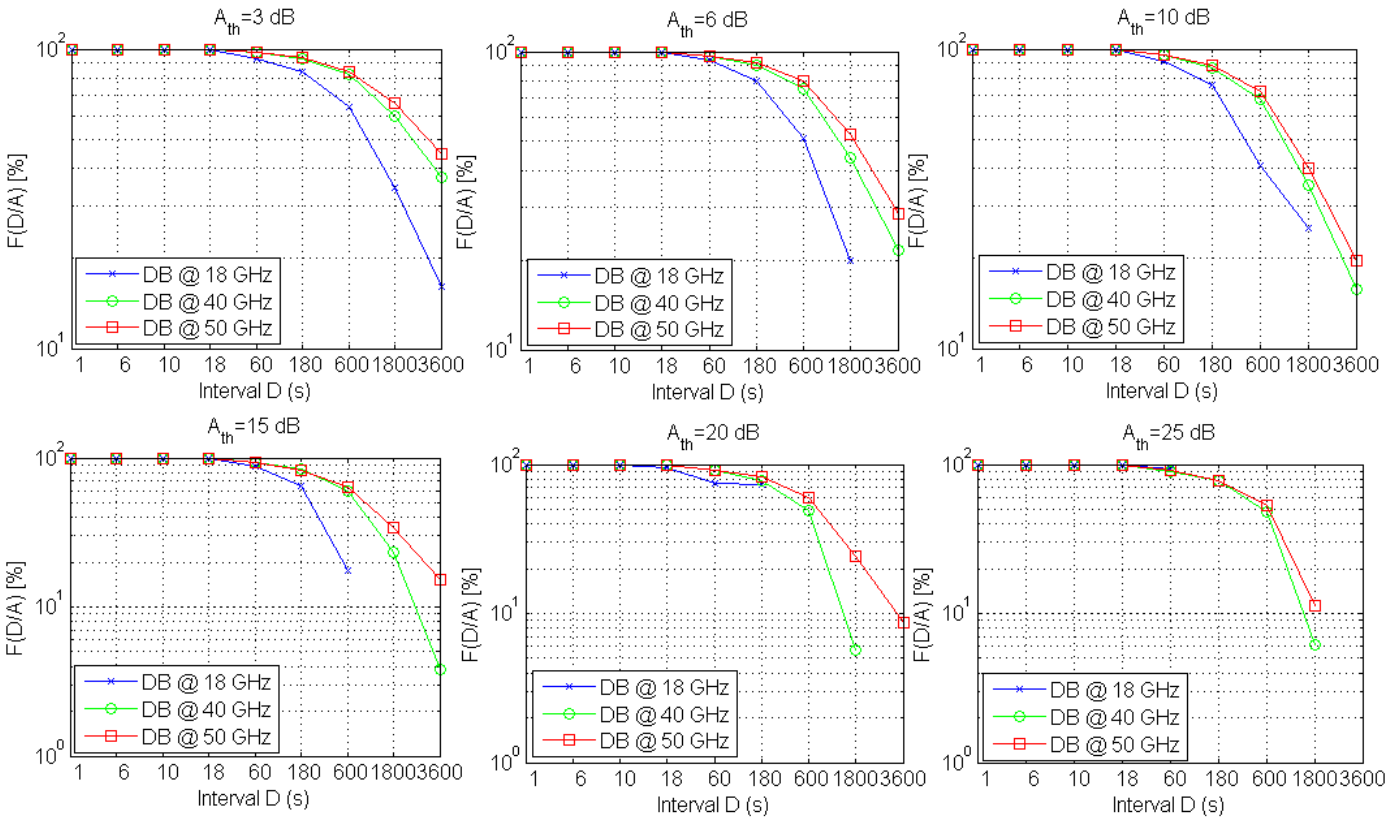

Figure 6.11: *Fade duration CDF for a Spino D'Adda at frequency 18.7, 39.6 and 49.5 GHz for 6 thresholds of attenuation [3, 6, 10, 15, 20 and 25 dB].*

Table 6.16: *Mean fade duration $< \epsilon_{TOT,FD} >$ error for different duration D averaged attenuation thresholds A for RTSG and ITU-R models*

		duration D [s]							
		6	10	18	60	180	600	1800	3600
39.6 GHz	RTSG	0.173	0.312	0.294	0.192	0.122	0.034	-0.090	-0.101
	ITU-R	5.059	3.982	2.743	1.283	0.927	0.604	0.403	0.244
49.5 GHz	RTSG	0.287	0.312	0.349	0.290	0.109	-0.003	-0.082	-0.089
	ITU-R	5.165	4.020	2.796	1.404	0.980	0.719	0.413	0.278

6.4.3 Fade slope validation

The Fade Slope FS is defined as the rate of change of attenuation with time. In the design of PIMT it is important to know the maximum FS of the receiver signal for the characterization of the control loop (minimum required tracking speed) and to allow short term prediction of propagation conditions [69]. Fig. 6.13 shows a simple representation of FS evaluation for a rain attenuation event.

The FS for a given link (fixed elevation angle) is dependent from the type of rain (widespread or convective rain), wind speed, path length trough rain and attenuation level. It has been proved that it is independent, for a given attenuation level, from the

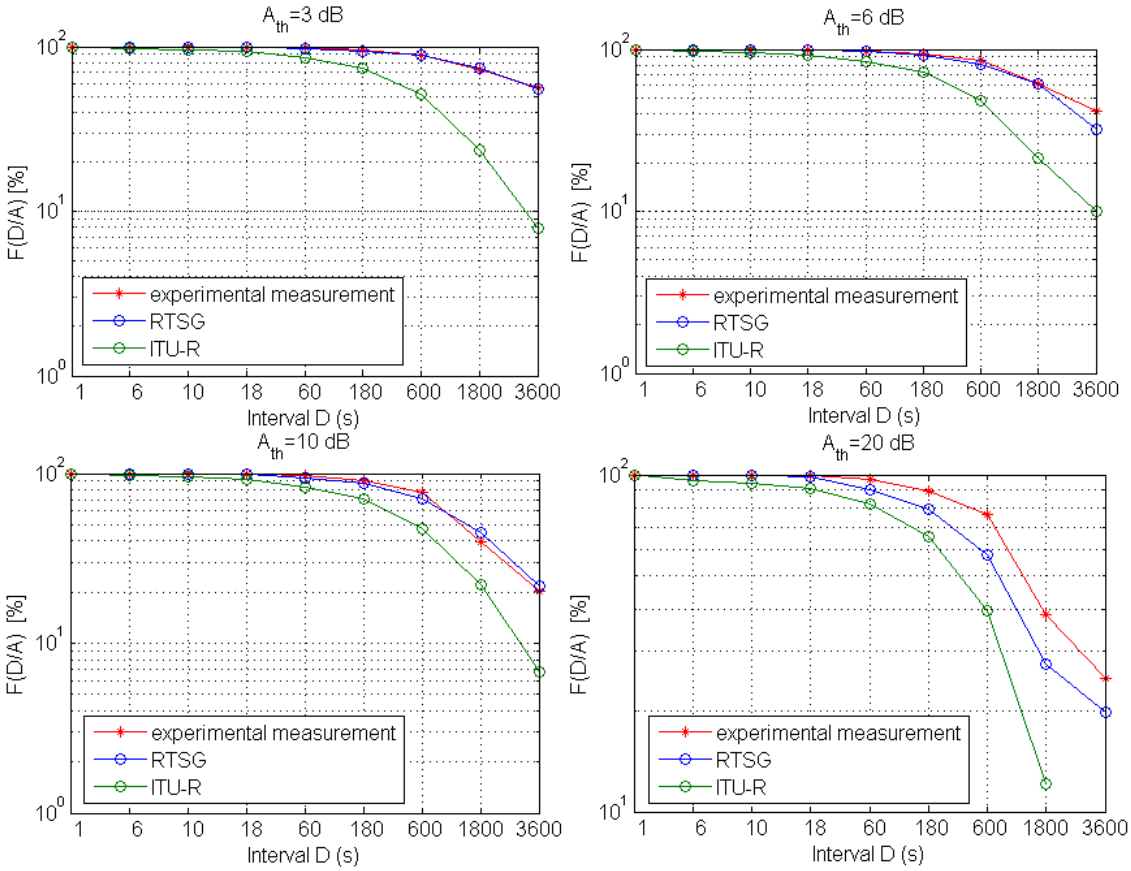

Figure 6.12: *Fade duration CDF for a Spino D'Adda at frequency 49.5 GHz and elevation angle 37.7° for 4 thresholds of attenuation [3,6,10 and 20 dB].*

Table 6.17: *RMSE fade duration $rms_{\epsilon_{TOT,FD}}$ error for different duration D averaged attenuation thresholds A for RTSG and ITU-R models*

		duration D [s]							
		6	10	18	60	180	600	1800	3600
39.6 GHz	RTSG	0.821	0.836	0.746	0.524	0.457	0.324	0.214	0.162
	ITU-R	5.124	4.048	2.827	1.379	1.032	0.721	0.453	0.279
49.5 GHz	RTSG	0.898	0.968	0.842	0.673	0.486	0.340	0.221	0.194
	ITU-R	5.236	4.116	2.901	1.529	1.103	0.815	0.504	0.330

frequency [71].

The FS statistic is evaluated as the probability P($|\zeta|/A$) of a fade slope ζ to be exceeded at a given attenuation threshold A. The error is calculated as function of threshold ζ and A as:

$$\epsilon_{FS}(\zeta, A) = 2\left(\frac{P_p(|\zeta|/A) - P_m(|\zeta|/A)}{P_p(|\zeta|/A) + P_m(|\zeta|/A)}\right) \tag{6.20}$$

where P_p is the predicted exceedance probability and P_m is the measured exceedance probability considered for the experimental radio link. The mean, RMSE and sigma

Table 6.18: *Sigma fade duration $\sigma_{\epsilon_{TOT,FD}}$ error for different duration D averaged attenuation thresholds A for RTSG and ITU-R models*

		duration D [s]							
		6	10	18	60	180	600	1800	3600
39.6 GHz	RTSG	0.802	0.775	0.686	0.488	0.441	0.322	0.194	0.126
	ITU-R	0.809	0.726	0.684	0.505	0.454	0.395	0.206	0.135
49.5 GHz	RTSG	0.851	0.916	0.766	0.607	0.474	0.340	0.205	0.172
	ITU-R	0.857	0.884	0.775	0.605	0.505	0.384	0.290	0.177

Table 6.19: *Fade duration total error $\epsilon_{TOT,FD}$ averaged over duration D and attenuation thresholds A for RTSG and ITU-R models for duration grater than 6 s*

		$< \epsilon_{FD} >$	$rms_{\epsilon_{FD}}$	$\sigma_{\epsilon_{FD}}$
39.6 GHz	RTSG	0.1170	0.5105	0.4792
	ITU-R	1.9056	1.9829	0.4893
49.5 GHz	RTSG	0.1466	0.5777	0.5414
	ITU-R	1.9719	2.0667	0.5596

Table 6.20: *Fade duration total error $\epsilon_{TOT,FD}$ averaged over duration D and attenuation thresholds A for RTSG and ITU-R models for duration grater than 60 s*

		$< \epsilon_{TOT,FD} >$	$rms_{\epsilon_{TOT,FD}}$	$\sigma_{\epsilon_{TOT,FD}}$
39.6 GHz	RTSG	0.0314	0.3362	0.3142
	ITU-R	0.6922	0.7728	0.3390
49.5 GHz	RTSG	0.0450	0.3828	0.3596
	ITU-R	0.7588	0.8562	0.3922

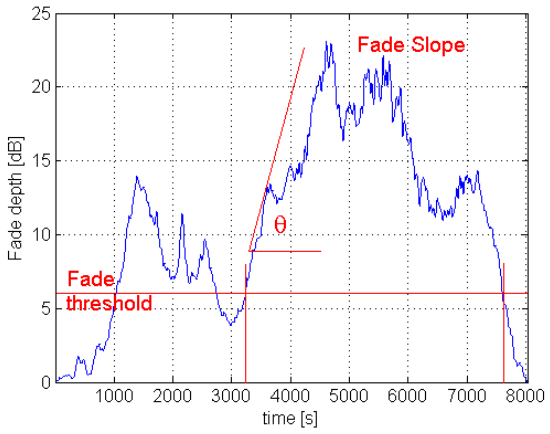

Figure 6.13: *An example of fade slope for a rainy event.*

error are evaluated to assess the model ability in reproducing FS. The analysis is performed for fixed value of fade slope ζ = [0.001, 0.002, 0.003, 0.005, 0.01, 0.02, 0.03, 0.05, 0.1,0.2, 0.3, 0.5, 1, 2, 3, 5] [dB/s] and thresholds of attenuation A = [1, 3, 5, 10, 15, 20, 25] [dB] as recommended in [66].

For our analysis, unfortunately we do not have available measurements of fade slope statistics, with the exception of ITALSAT measurements. The fade slope statistics for the ITALSAT database at 18.7, 39.6 and 49.5 GHz for a subset of attenuation thresholds in Fig.6.14 are reported. The figure shows a similarity between the statistics measured at different frequency, since the FS is independent from the system frequency [71]. The rain events are filtered with a low-pass filter (cutoff frequency of 0.025 Hz) to remove scintillation. The FS statistic is calculated assuming a window size of 2 s.

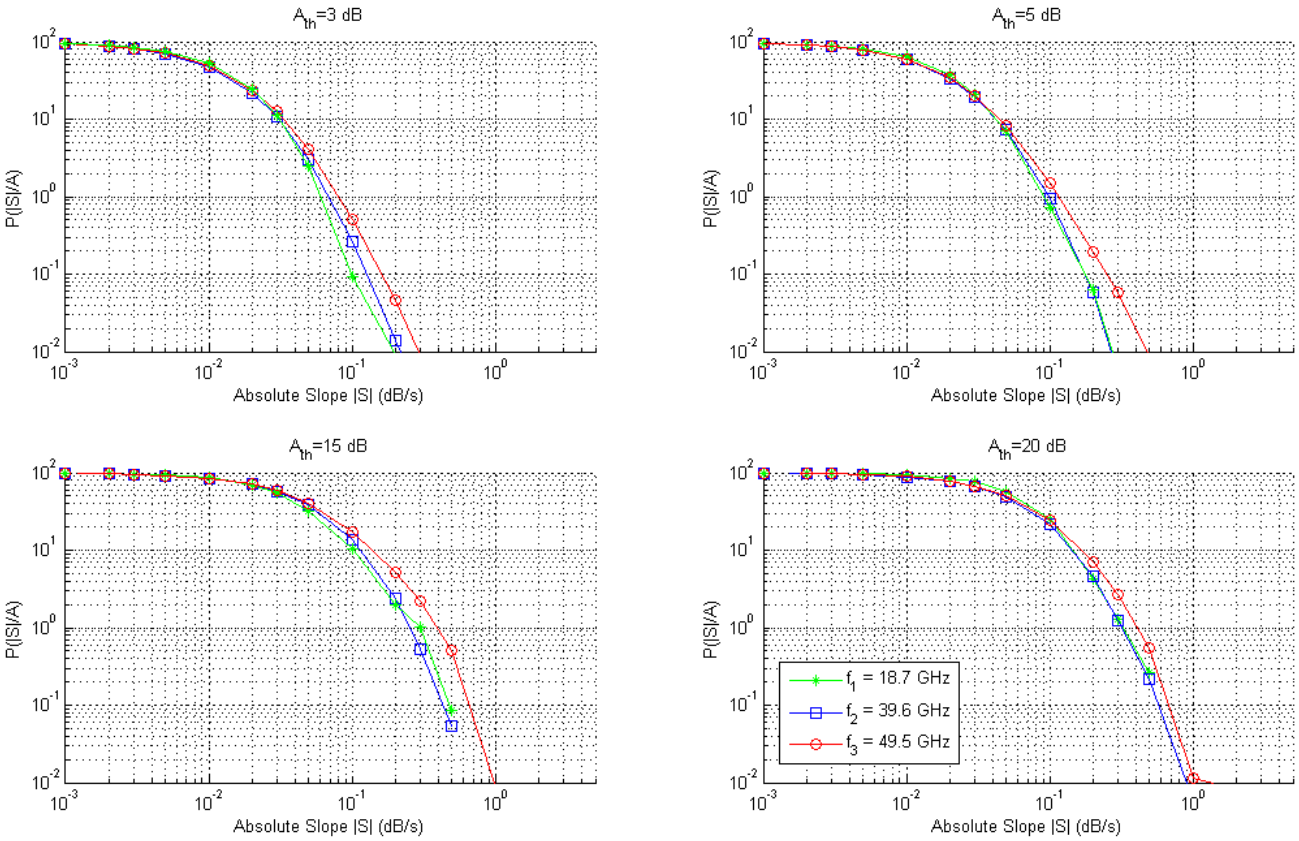

Figure 6.14: *Fade Slope CDF for a Spino D'Adda at 18.7, 39.6 and 49.5 GHz and elevation angle 37.7° for 4 thresholds of attenuation [3,5,15 and 20 dB].*

For each frequency (39.6 and 49.5 GHz), we evaluate 7 years of CDFs of rain attenuation and FS. The ITU-R and RTSG model are compared for the prediction of FS statistics taking as input the CDFs of rain attenuation. We expect to have a better performance for the RTSG model, since it uses as input the ITDB database (collected at 18.7 GHz) to generate the synthetic time series. The synthetic time series of attenuation of ITU-R model are filtered with a low-pass filter (cutoff frequency of 0.025 Hz) to remove scintillation. In Tab. 6.21, 6.22 and 6.23 we report the mean, RMSE and sigma error of FS analysis averaged over attenuation thresholds for different slope ζ for the database at 39.6 GHz. The summarize results for all frequencies are reported in Tab. 6.24. All tables show good performance for RTSG model as expected.

Table 6.21: *Mean fade slope $< \epsilon_{TOT,FS} >$ error for different slope ζ and averaged attenuation thresholds A for RTSG and ITU-R models for database at 39.6 GHz*

	slope ζ [dB/s]							
	0.001	0.003	0.010	0.030	0.100	0.300	1.000	3.000
RTSG	0.206	0.385	0.305	0.308	0.384	0.285	0.311	0.157
ITU-R	-0.381	0.278	0.309	-0.414	-0.760	-0.014	0.465	-0.385

Table 6.22: *RMSE fade slope $rms_{\epsilon_{TOT,FS}}$ for different slope ζ and averaged attenuation thresholds A for RTSG and ITU-R models for database at 39.6 GHz*

	slope ζ [dB/s]							
	0.001	0.003	0.010	0.030	0.100	0.300	1.000	3.000
RTSG	0.439	0.533	0.633	0.812	0.673	0.455	0.491	0.787
ITU-R	1.096	1.072	0.998	1.102	1.326	0.973	0.820	1.161

Table 6.23: *Sigma fade slope $\sigma_{\epsilon_{TOT,FS}}$ error for different slope ζ averaged attenuation thresholds A for RTSG and ITU-R models for database at 39.6 GHz*

	slope ζ [dB/s]							
	0.001	0.003	0.010	0.030	0.100	0.300	1.000	3.000
RTSG	0.388	0.368	0.554	0.752	0.552	0.355	0.380	0.771
ITU-R	1.027	1.035	0.949	1.021	1.086	0.973	0.676	1.096

Table 6.24: *Fade slope total error $\epsilon_{TOT,FS}$ averaged over slope ζ and attenuation thresholds A for RTSG and ITU-R models*

		$< \epsilon_{FS} >$	$rms_{\epsilon_{FS}}$	$\sigma_{\epsilon_{FS}}$
39.6 GHz	RTSG	0.2874	0.5967	0.5110
	ITU-R	-0.1125	1.0623	0.9772
49.5 GHz	RTSG	0.2879	0.7772	0.7182
	ITU-R	-0.1912	1.1333	1.0352

CHAPTER 7

Synthesis of total attenuation time series

7.1 Introduction

In this chapter we discuss the generation of total attenuation time series. In the chapter 5 and 6 we have analysed separately the synthesis of the time series for ILWC and IWVC (selected with a joint procedure) and the synthesis of rain attenuation. The generation of the total attenuation time series requires a careful superimposition of these synthesized components, including also the contribute of oxygen attenuation.

We start considering the non rainy atmospheric components, i.e. the clear sky attenuation (water vapor and oxygen) and the cloud attenuation. First, we transform the integrated ILWC and IWVC into attenuation time series according to the radio link parameters (elevation angle, working frequency). The generation of a time series derived by the composition of these quantities is supported by the selection of synchronous daily time series of ILWC and IWVC. The only requirement is the ordering of the daily time series according to the procedure presented in section 5.2.5. Finally, the oxygen is assumed as a constant value derived from radiosounding and, in case they are not available, throughout Rec. ITU-R 1510-0 and Rec. ITU-R 676-10, and it is scaled for the defined elevation angle.

Clouds are assumed as the master variable in the overlapping of rain attenuation events. Making use of Cloud Type Algorithm (CTA), detailed in Appendix A, we discriminate rainy from not-rainy clouds. When a cloud is classified as rainy (Cloud Type 3 CT3 or Cloud Type 4 CT4) we superimpose the rain attenuation events.

Finally, the total attenuation is achieved by superimposing, sample by sample, clear sky, cloud and rain attenuation.

7.2 Clear-sky and cloud attenuation modelling

The output of Liquid Water and Water Vapor time series generator are two joint synthetic time series that reproduce the climatology defined in OBF. After the selection of daily time series they are ordered according to the daily time series date. Then, we translate the ILWC and IWVC values into synthesize time series of clear-sky and cloud attenuation. The synthetic time series refers to the integrated values at the zenith such that they can be converted into attenuation taking into account the operational frequency and scaled to the elevation angle defined for the Satcom system. The scaling procedure is quite simple and requires the evaluation by means of RAOBS measurements for the desired location, the mass absorption coefficients $a_{L,f}$ and $a_{V,f}$ which are mainly dependent from the system frequency and dielectric permittivity as reported in Eq. 4.7. In case RAOBS measurements are not available for the retrieval of mass absorption coefficient, the computation of cloud and clear-sky attenuation is obtained through Rec. ITU-R 840-6 [13] and Rec. ITU-R 676-10 [8], respectively. However, the use of the mass absorption coefficient for the computation of cloud attenuation provide a better estimation of the cloud attenuation value with respect to the elaboration through Rec. ITU-R 840-6. Indeed, this recommendation requires in input the use of integrated liquid water content reduced at 0°C that is different from the integrated liquid water content retrieved from radiometer. As shown in [72] the reduced liquid water is quite sensitive to the reduction temperature, therefore to avoid possible error introduced by this approximation we consider mass absorption coefficients when available. To the contrary, for the clear sky attenuation, in case the mass absorption coefficient for the water vapor or the attenuation for oxygen are not available from RAOBS measurements, the use of Rec. ITU-R 676-10 does not introduce any relevant uncertainty. The elevation angle θ of the satellite is taken into account by simply dividing the zenith values of ILWC and IWVC attenuation for the sine of the angle. Assuming L and V as the ILWC and IWVC [mm] respectively, the complete formulations for the scaling procedures are here reported:

$$\begin{aligned} A_L(f,\theta) &= \frac{a_{L,f}L}{\sin(\theta)} \quad [dB] \\ A_V(f,\theta) &= \frac{a_{V,f}V}{\sin(\theta)} \quad [dB] \end{aligned} \tag{7.1}$$

For the time series synthesis we assume an elevation angle between 5° and 90°. The evaluation of the absorption mass coefficients is obtained by means of RAOBS measurements for 14 sites listed in Tab. 7.1. The frequency is varied between 5 till 200 GHz as shown in Fig. 7.1. The Rayleigh approximation [12] of Mie scattering theory can be adopted for cloud's drops diameter up to 200 GHz.

Focusing on the city of Hemsby-In-Norfolk, the variation of $a_{L,f}$ and $a_{V,f}$ coefficients as dependent from frequency can be better estimated. Figures 7.2 highlight the effect of lines absorption at 22.253 and 183.3 GHz for the Water Vapor. In Fig. 7.3 we report an example of simulated attenuation time series for different frequency values [20, 40, 60, 80, 100, 140, 180 and 200 GHz]. As observed so far, for the mass absorption coefficients of IWVC, the CDFs at 20 and 180 GHz show increased values of A_V due to the line absorption present at these frequency bands.

Table 7.1: *List of selected sites for FERAS measurements considered for the test of ILWC and IWVC quantities*

Station Code	City	Country	Latitude (°)	Longitude (°)
02836	Sodankyla	FI	67.22	26.39
02963	Jokioinen	FI	60.49	23.30
03026	Stornoway	UK	58.13	-6.59
03496	Hemsby-In-Norfolk	UK	52.41	1.41
06260	De-Bilt	NL	52.06	5.11
06447	Uccle	BX	50.48	4.21
07481	LyonSatolas	FR	45.44	5.05
10384	Berlin(Templehof Airport) (Us)	DL	52.29	13.25
11035	WienHohe-Warte	OS	48.15	16.22
16080	Milano (Linate Airport)	IT	45.26	9.17
16320	Brindisi	IT	40.39	17.57
16429	Trapani (Birgi Airport)	IT	37.55	12.30
16560	CagliariElmas	IT	39.15	9.03
27612	Moscow	MSRS	55.45	37.34

Due to its slow yearly variation, the oxygen attenuation $A_{OXY,f}$ is there assumed to be constant for all the duration of the synthetic time series and is calculated throughout RAOBS measurements, when available, if not through Rec. ITU-R 1510 [42] and Rec. ITU-R 676-10. This quantity evaluated at the zenith is easily scaled for the required elevation angle as follow:

$$A_{OXY}(f,\theta) = \frac{A_{OXY,f}}{\sin(\theta)} \quad [dB] \tag{7.2}$$

In Fig. 7.4 we report the zenith value of oxygen attenuation for the city listed in 7.1 varying the frequency from 5 till 200 GHz. In Fig. 7.5 we give a detailed variation of the oxygen attenuation for the city of Hemsby-In-Norfolk (UK) according to the frequency. We observed that, as expected, the oxygen has two absorption lines in the band from 50 to 70 GHz and at 118.7 GHz.

7.3 Cloud type overlapping procedure

The last but more delicate procedure is the composition of the cloud and rain attenuation events. The basic rule is to collocate a rain event only in presence of a cloud interval. Within this study, we identified some cloud characteristics that can be exploited to better overlap rain events. We based the overlapping procedure on the recognition of which cloud types are most likely to support rain events with higher probability, according to the Cloud Type Algorithm (CTA) presented in Appendix A. With this method, we close off each cloud of the synthetic time series of ILWC and we classify it according to the values assumed by ILWC and IWVC within the cloud's interval. The classification is set up from the analysis of 10 years of RAOBS measurements. During this study we verified by means of radiometric measurements that the presence of rainy events is detected only within Cloud Type 3 CT3 and Cloud Type 4 CT4 clouds as shown in Fig. 9.8. The algorithm returns the indicator of clouds that have the higher probability of giving rise to rain (CT3 and CT4).

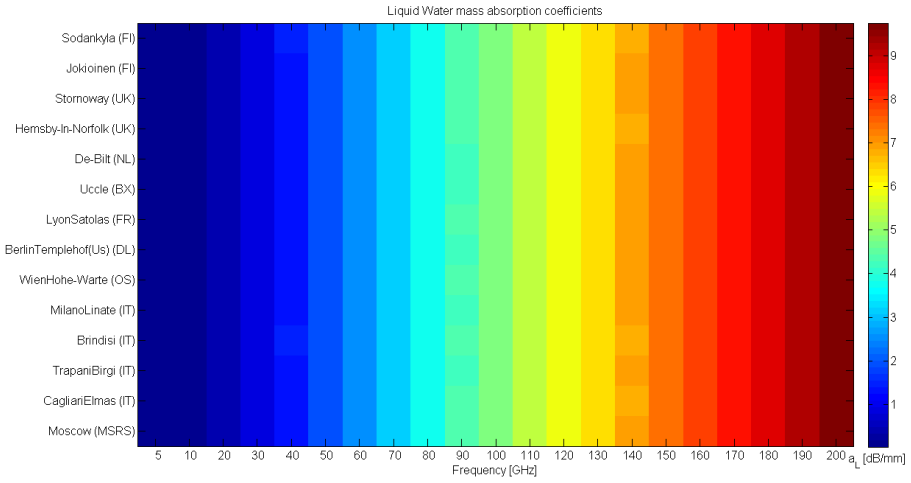

(a)

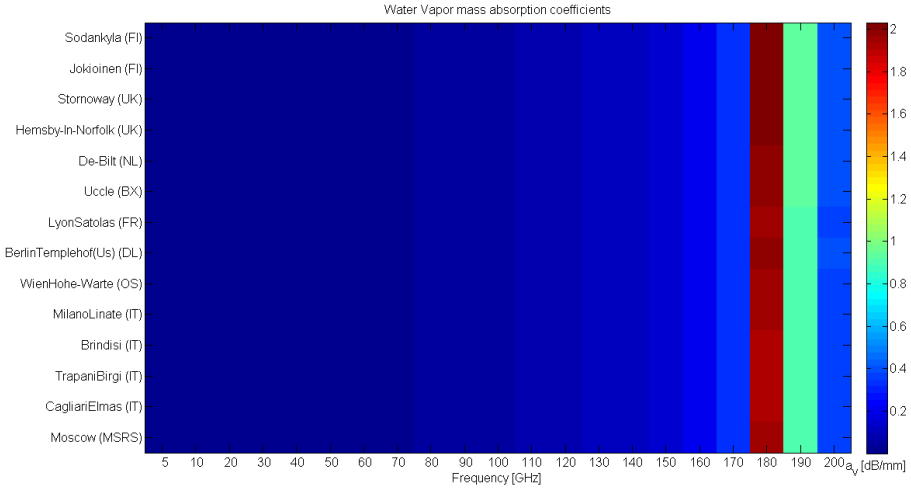

(b)

Figure 7.1: *Mass absorption coefficients $a_{L,f}$ and $a_{V,f}$ for 14 locations at varying frequencies (from 5 till 200 GHz)*

Moreover, making use of radiometric data and observing the rainy windows detected as proposed in paragraph 4.3.2 we observed that the percentage of each cloud interval interested by rain is less than the 50% interval length. Therefore, we adopted as general criterion to allocate at most $p = 50\%$ percentage of cloud interval, called *rainy mask* (RM), to be overlapped by an event of rain. An example of cloud interval and RM is depicted in Fig. 7.6 where in red dashed line we report the cloud interval while in magenta the RM.

Finally, the overlapping procedure takes place. With CTA algorithm we take in input the rain attenuation events $A_{R,i}$ and finally we return a synthetic time series A_R of concatenated rain attenuation events and not rainy intervals (set to zero). During the $A_{R,i}$ allocation ,we start considering with higher priority CT4 clouds. The procedure follows the steps below:

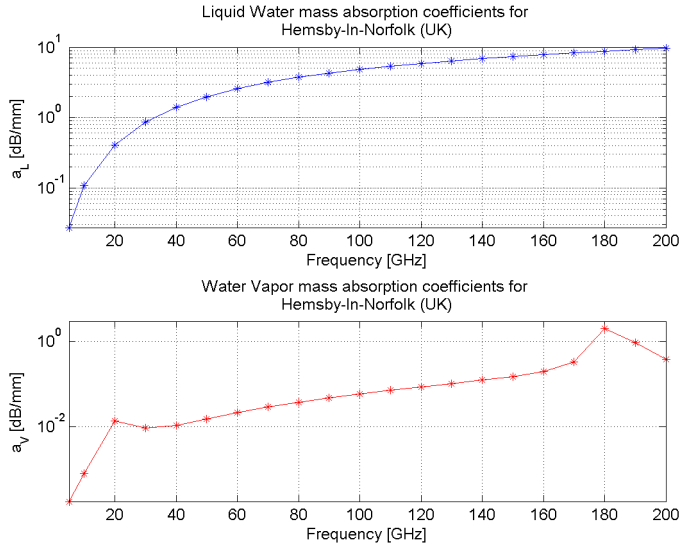

Figure 7.2: *Mass absorption coefficients $a_{L,f}$ and $a_{V,f}$ for the city of Hemsby-In-Norfolk (UK) at varying frequencies (from 5 till 200 GHz)*

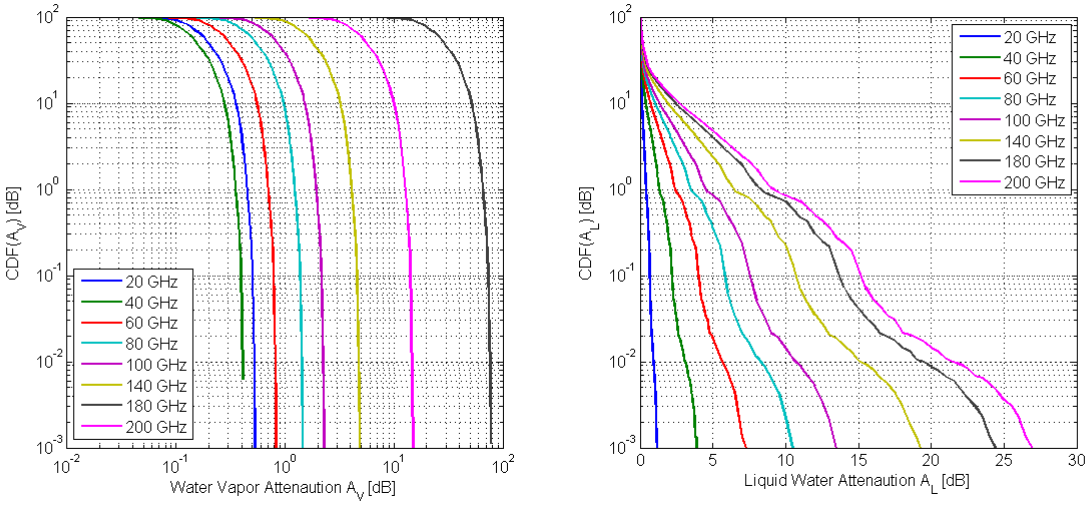

Figure 7.3: *An example of attenuation CDF for the city of Hemsby-In-Norfolk (UK) at varying frequencies (from 5 till 200 GHz)*

1. it superimposes a rain attenuation event and a rainy mask RM of equal length;
2. the remaining rain attenuation events are superimposed with RM of longer length and, if needed, single rain attenuation events are put together.

Note that, generating the A_R time series, short rain events can be put close to each other. This procedure does not affect the log normal distribution of duration of rain events. The achievement of the overlapping procedure is guaranteed from the fact that the percentage of time with cloud is higher than the percentage of time with rain attenuation.

An example of the output of the overlapping procedure is given in Fig. 7.7. Here

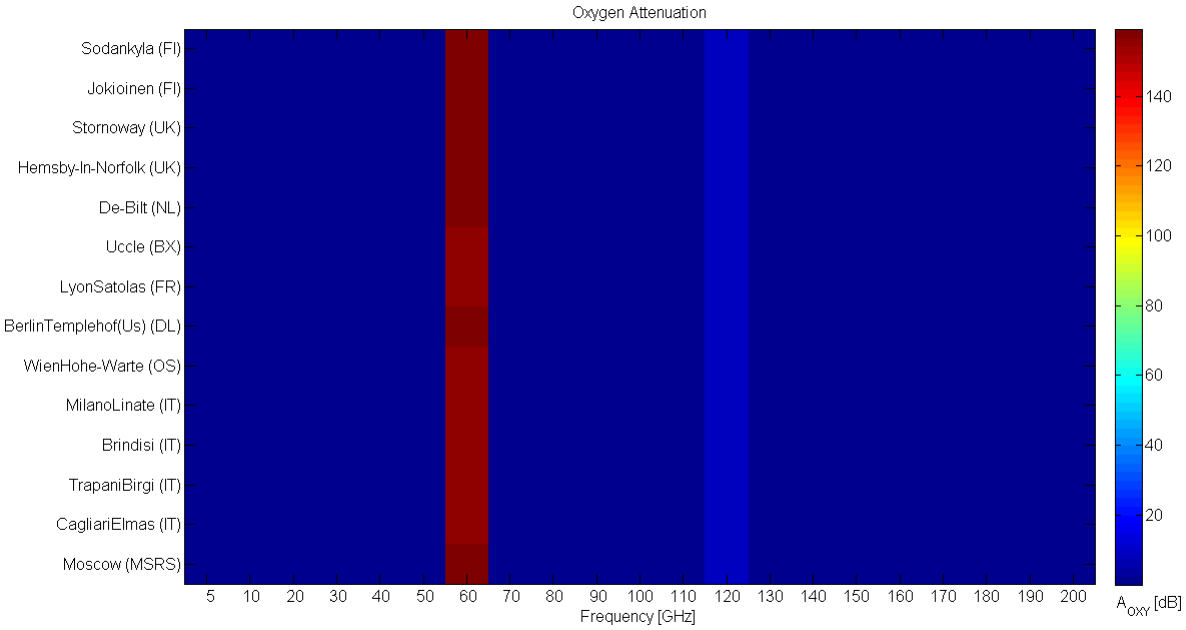

Figure 7.4: *Oxygen attenuation $A_{OXY,f}$ for 14 locations at varying frequencies [from 5 till 200 GHz]*

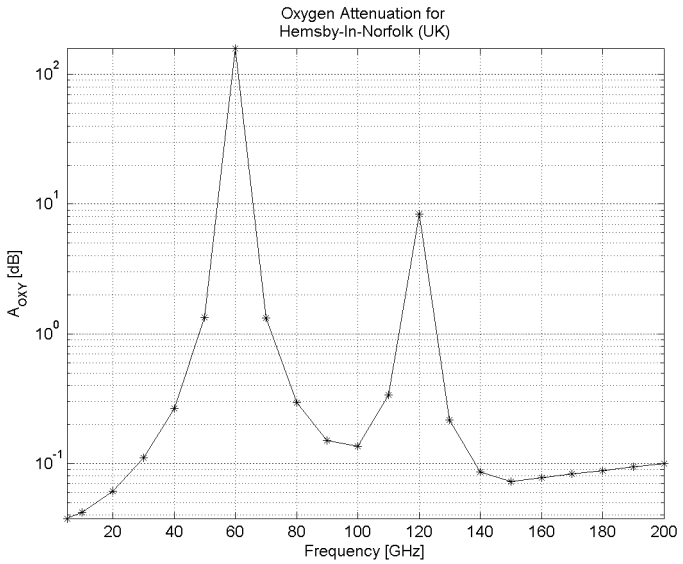

Figure 7.5: *Oxygen attenuation $A_{OXY,f}$ for the city of Hemsby-In-Norfolk (UK) at varying frequencies [from 5 till 200 GHz]*

we report the time series of Water Vapor and Liquid Water Content (with the cloudy intervals in red dashed line) and finally the rain events selected for each RM. As shown in the zoom image, a single event covers only the p percentage of the cloudy interval.

Once all the rain events are properly allocated and A_R time series is generated, a time series of total attenuation is built up.

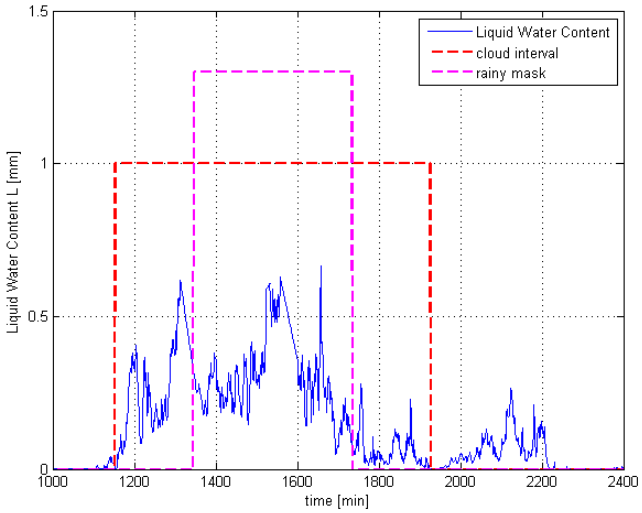

Figure 7.6: *An example of percentage time of rain (RM) allocated in a cloud interval.*

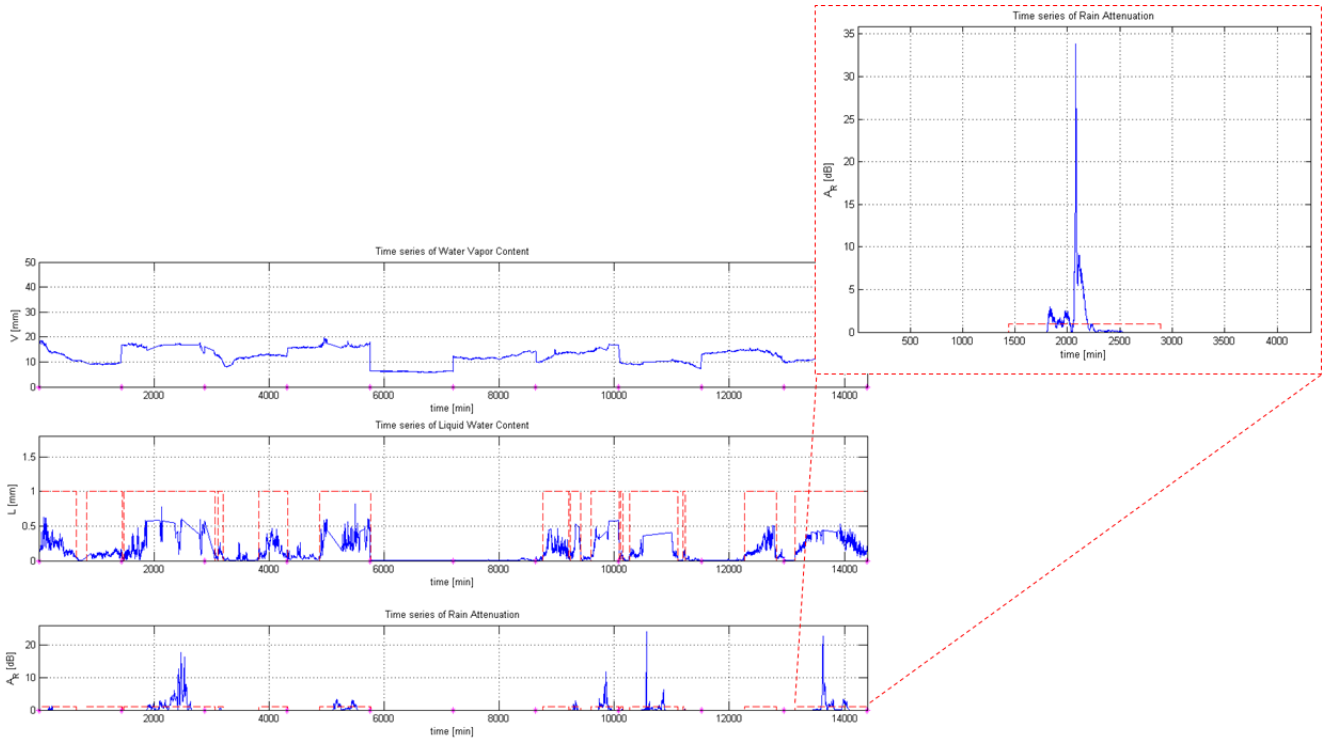

Figure 7.7: *An example of the water vapor, liquid water and rain attenuation time series. For the liquid water we identify in red dashed line the cloud intervals and we zoom a rain event to highlight the percentage of cloud p interested by rain.*

7.4 Total attenuation composition

The last step for the total attenuation time series synthesis consists in overlapping all the atmospheric components that have been individually generated. The total attenuation

A_{TOT} [dB] time series represents the combined effect of rain A_R, clear-sky (composition of water vapor A_V and oxygen A_{OXY}) and clouds (liquid water A_C) attenuation. The overlapping procedure must be performed sample by sample. Practically, as presented so far, due to the nature of the joint selection of clear-sky and clouds daily time series, an overlapping procedure is not required. To the contrary, the combination of the events of rain attenuation with clouds time series wants an accurate analysis of cloud properties with CTA. A general block scheme is reported in Fig. 7.8.

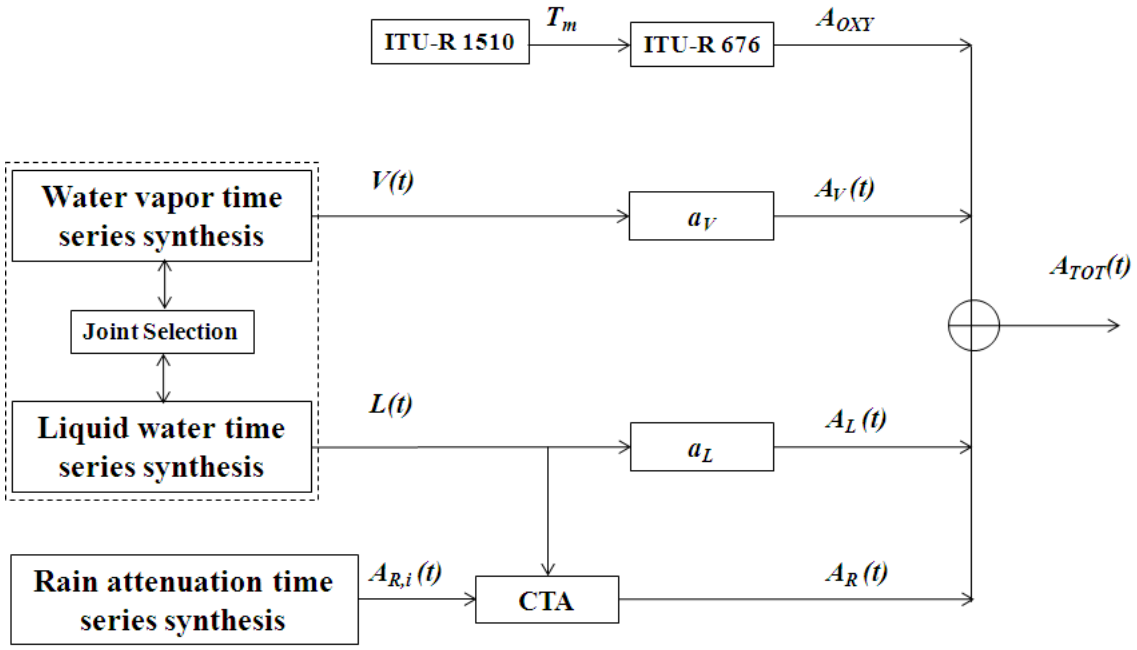

Figure 7.8: *Block scheme of the total attenuation time series synthesis.*

The total attenuation is therefore calculated sample by sample adding together the atmospheric components as:

$$\begin{aligned} A_{TOT}(i\Delta T) &= A_{OXY} + A_V(i\Delta T) + A_C(i\Delta T) + A_R(i\Delta T) \\ &= A_{clear-sly}(i\Delta T) + A_C(i\Delta T) + A_R(i\Delta T) \end{aligned} \tag{7.3}$$

where i is the index of each sample and ΔT=1 s is the time interval between two consecutive samples.

In Fig. 7.9 and 7.10 we report an example for the generation of a daily time series of total attenuation for Spino D'Adda for a radio link at frequency of 23.8 GHz and an elevation angle of 37.7°. In Fig.7.9 the single attenuation components are reported separately, while in Fig. 7.10 we superimpose all time series leading to the synthesis of A_{TOT} time series.

7.4.1 Time Series Synthesizer applicability

The time series synthesizer of total attenuation could be applied for the generation of synthetic data up to W band. In the definition of the range of frequencies for the applicability of the synthesizer, two specific frequency ranges, one for the clear-sky and cloud attenuation and another one for the rain attenuation are considered.

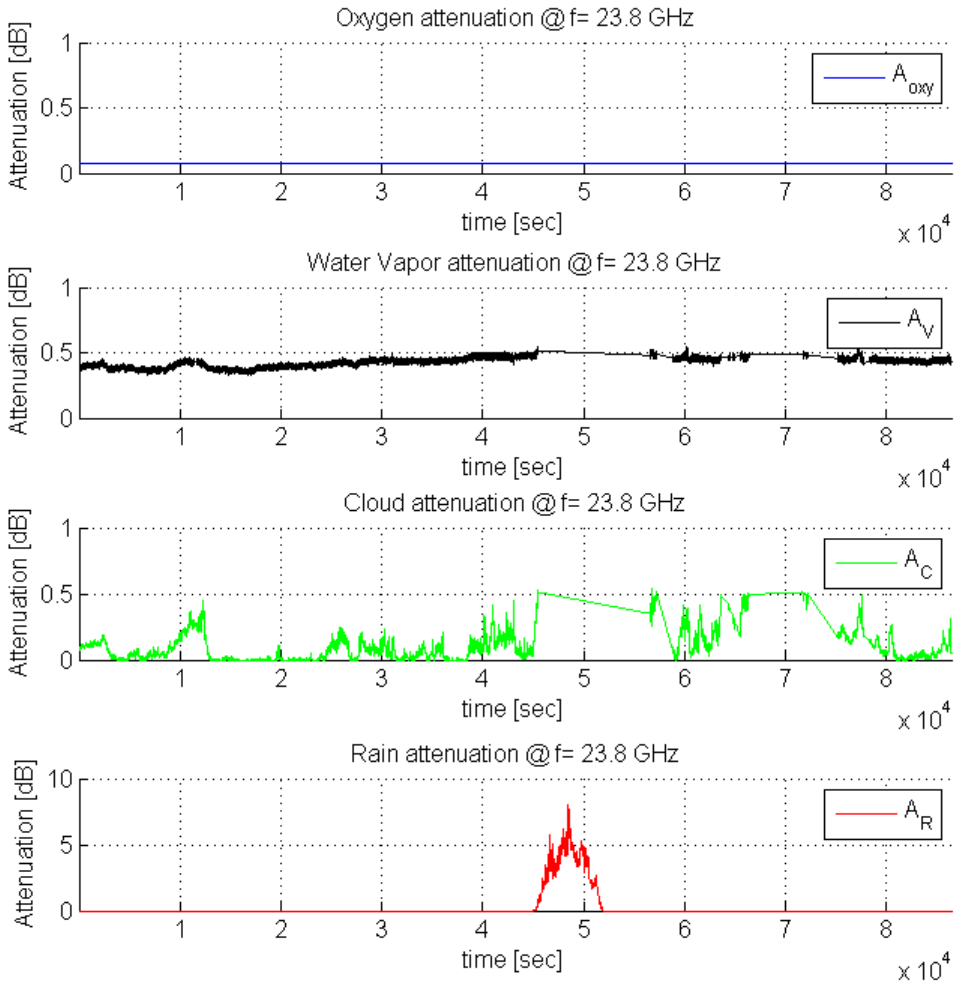

Figure 7.9: *Daily time series of simulated atmospheric components (oxygen, water vapor, clouds and rain attenuation).*

For what concern the clear-sky and cloud attenuation time series we could assume in principle a frequency range up to 200 GHz being the Rayleigh approximation of the Mie scattering theory, that allow the assumption that cloud attenuation depends only on the liquid water content, applicable up to 200 GHz (a physical limitations). Practically, we derived from the available brightness temperature measurements the time series of ILWC and IWVC and subsequently we multiplied the path integrated quantities for the mass absorption coefficients derived for the proper frequency by RAOBS measurements.

For what concern the rain attenuation time series, we selected the rain events (at 18.7 GHz) from the original ITALSAT database that are scaled in frequency (according to the formulation of frequency scaling presented in paragraph 6.2.1 used because of its simplicity and because the choice is not critical) when necessary only to ensure the presence of a significant number of events with high attenuation peaks as it is foreseen is occurring along a link operating at Q/V band and above. In fact, the model has no need

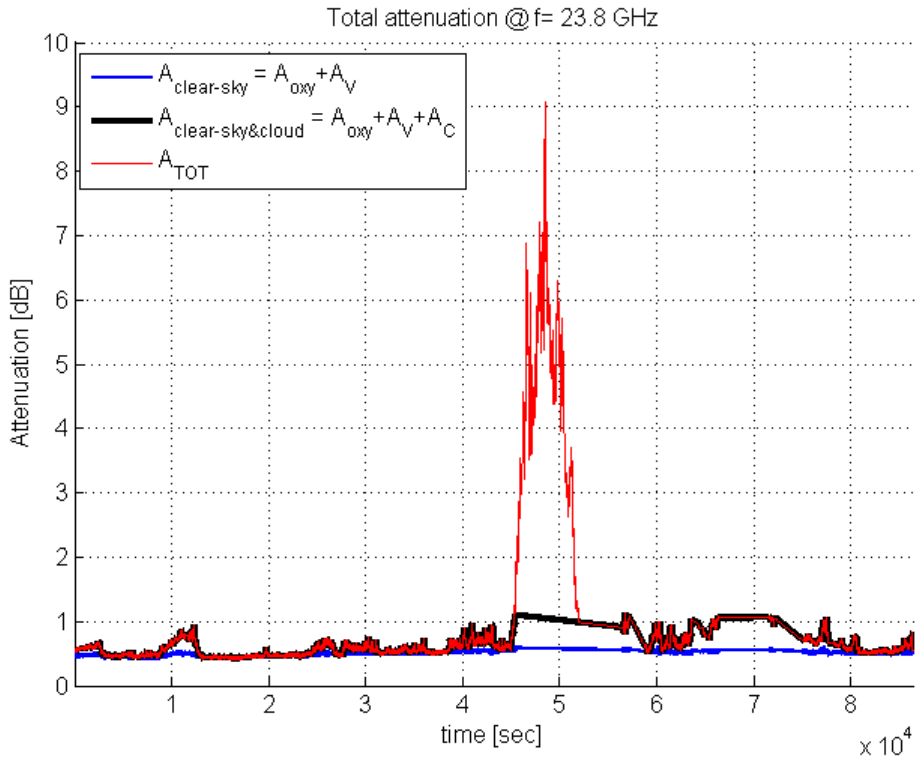

Figure 7.10: *Composition of clear-sky, cloud and rain attenuation for the daily time series shown in Fig. 7.9*

to use rain events measured at the frequency of the specific radio link to be synthesise. In this respect, in the previous chapter we verified that the frequency scaling do not affect the fade slope statistic of the synthetic time series. Therefore, in case the rain events present in the ITALSAT database cover the attenuation range of the specific radio link, we do not need to make even the scaling. Unfortunately, due to lake of measurements, we make the validation of first and second order statistics only over a database that contains measurements up to 50 GHz. Therefore, we have not been able to prove that effectiveness of the model is applicable for frequency above 50 GHz. To be absolutely conservative we indicated as upper bound the 50 GHz limitation.

In conclusion, even if for the clear-sky, cloud and oxygen we could model the effects up to 200 GHz, for the whole synthesizer we assume a valid range of frequency comprised between 5 and 50 GHz to be consistent with the frequency ranges assumed during the rain attenuation validation. Is important to underline that this frequency range is not mandatory for physical limitation and could be enlarged up to W bands.

The RTSG synthesizer has been tested with a database that consider measurements from 6° till 83° of elevation angle, therefore we consider the time series generator applicable for a range of elevation angles comprise between 5° and 90°.

Finally, for the region of pertinence, we tested the RTSG synthesizer over several location at different latitudes and longitudes, including tropical sites. Despite that, since in the ILWC and IWVC validation we assumed only European sites, we limit the region of applicability to temperate regions at middle latitude.

To conclude, although the validation have been conducted for data in frequency range 6-50 GHz and elevation angle in the rage from 6°-83 °, the synthesized time series of total attenuation are expected to be valid at least in the frequency range from 5 till 70 GHz and elevation angle between 5° and 90°. The time series of total attenuation is assumed as applicable for all the temperate regions at middle latitude.

CHAPTER 8

Conclusion

In this thesis we presented a synthesizer of tropospheric components (liquid water, water vapor, rain and oxygen) able to reproduce time series of total attenuation for given location and satellite link parameters (elevation angle and frequency). The basic idea behind the model is to generate consistent time series of attenuation for each tropospheric element and then to perform an accurate overlapping of all components to reproduce time series of total attenuation. The outputs (intermediate and final) of the algorithm are the following:

- joint generation of time series of water vapor and liquid water attenuation;
- rain attenuation events time series;
- oxygen attenuation contribution kept as a constant value;
- total attenuation time series;

The generation of any single element is obtained taking in input the long-term statistic of each effect. The synthesis has been supported by the use of a database of historical measurements (collected during ITALSAT experiment in Spino D'Adda) that has been assumed as exhaustive for the reproduction of climatology for any site at middle latitude. The use of historical database ensures a realistic behaviour of each atmospheric element. The events of rain attenuation have been extrapolated from beacon measurements at 18.7 GHz. The single event has been isolated within beacon signal and accurately filtered to remove scintillation effects. The Integrated Water Vapor content (IWVC) and Integrated Liquid Water Content (ILWC) have been derived from radiometric measurements at 23.8 and 31.6 GHz through an accurate retrieval with an additional procedure to correct lower values of ILWC (clear sky correction procedure). The rain intervals detected within ILWC and IWVC time series have been accurately

removed with a procedure that made use of information provided by three databases: radiometer, beacon receiver and raingauge. The analysis of the yearly, seasonal and daily trend of ILWC and IWVC showed that these two quantities cannot be considered as completely disjoint. To maintain this characteristic we chose the day as the basic frame to generate synthetic time series and we kept together the daily time series of ILWC and IWVC.

Structure of the tropospheric synthesizer

The synthesizer is constituted by two separated optimization procedures, one for the rainy and the other one for non-rainy components. The algorithm for the synthesis of the non-rainy components ILWC and IWVC is composed by two steps: a single optimization for each component separately and a joint selection of daily time series from the database to maintain the ILWC and IWVC synchronous variation.

The rain attenuation time series are based on the Rain Time Series Generator (RTSG) model based on a previous model called Experimental Measurement Base (EMB). This latter made use of an optimization procedure that is not effective for higher frequency ranges and that cannot control accurately the probability of rain defined for the given site. We modified the optimization procedure by changing the selection of rain events and we forced the algorithm to meet the probability range value of the simulated site. Furthermore, we introduced a new procedure to modify the rain probability conditioned to the radio-link elevation angle.

Finally all the generated time series are combined to produce the synthetic total attenuation. The ILWC is used as master in the overlapping procedure. The rain attenuation events are collocated over defined windows identified within cloudy intervals. We developed a new Cloud Type Algorithm able to discriminate and catalogue cloud types and identify rainy clouds. By observing the cloud and rain structure we defined that the 50% percentage of rainy cloud could be assumed as available for rain superimposition, the so called 'rainy mask'. On the contrary, IWVC time series do not require any superimposition since they are automatically overlapped to ILWC time series thanks to the selection of contemporary daily time series. Oxygen is there considered as constant and estimated by means of radiosounding or ITU-R model [8].

Model validation

The validation of the model has been performed separately for rainy and non-rainy components. For non-rainy components, the time series of liquid water and water vapor have been synthesized taking in input the CDF derived by RAOBS measurements in 7 locations. First, we evaluated the ability in the reconstruction of the Objective Function (OBF) statistics through the generation of 10 replicas of one year of synthetic time series for each site. We considered the discrepancy between the OBF and the long-term statistic obtained by the composition of the 10 replicas and furthermore the analysis of the inter annual replicas variation. For the long-term statistic the results showed a good ability of the synthesis of CDF statistics is comprised between 7-11% for ILWC and 2-8% for IWVC. The inter-replicas variability is quite limited and is minor than the inter annual variability detected by Radiometric Database (RADDB). A qualitative analysis allowed to assess the seasonal variations of ILWC and IWVC in the generated annual replicas to ensure an intra-annual dynamics of these values. This validation underline that, despite the model is not forced to reproduce the intra annual variability of ILWC and IWVC, the annual trend is quite evident in the synthetic time series.

For the validation of rain attenuation we considered the DBSG5 database [67] and beacon measurements collected in the ITALSAT experiment at 39.6 and 49.5 GHz. The goal of the testing was to evaluate the ability of the RTSG model to generate the OBF used as input to the model (first order statistic validation) and then to investigate in detail the dynamic behaviour of the time varying channel (second order statistic validation). The ITU-R model described in Recommendation ITU-R 1853-0 [68] has been used as term of comparison of the performance of RTSG model. In the first order statistics analysis, the validation took into account 143 different experiments, for a frequency range up to 50 GHz and elevation angle 6° and 73°. The percentage RMSE highlight that the RTSG model was the best performing since we obtain 15.3 % of error compared with 26.8% produced by ITU-R model. Furthermore, the ability of RTSG with respect to ITU-R has been increased when 49.5 GHz database is taken into account. The Fade Duration FD validation (second order statistic analysis) has been performed over 73 experiments for a frequency range up to 50 GHz and elevation angle 6° and 83°. The FD analysis performed for duration longer than 60 s showed a comparable performance of RTSG and ITU-R models, while the improvement of RTSG performance has been highlighted for 39.6 and 49.5 GHz frequencies. The Fade Slope FS validation (second order statistic analysis) has been carried out considering the ITALSAT database collected at 39.6 and 49.5 GHz. This validation has been performed even if the considered database showed comparable FS statistics with respect to the input ITDB database at 18.7 GHz. The FS results showed better performance of RTSG model with respect to ITU-R models.

The validation of both rain and non-rain components ensures an applicability of the synthesiser for temperate regions. The considered range of frequencies is between 5 and 70 GHz. The range of elevation angle is between 5° and 90°.

We observed an overall good characterization of single tropospheric elements that is ensured by real time series derived from historical database.

Further works

In this thesis we presented a time series synthesizer, able to characterize the channel varying behaviour of tropospheric components. The model assessment highlight its ability in producing synthetic time series for several location in temperate regions. At the end of this work we suggest some additional works that can be implemented to further improve the synthesizer performance. Three main topics can be developed:

- the introduction of a model for scintillation synthesis. In this work we did not focus on atmospheric turbulence, therefore we believe this implementation could be an interesting improvement for our model;
- an even more accurate procedure to manage the transition among two consecutive daily time series of ILWC or IWVC in order to improve the realistic behaviour of synthetic time series of non-rain components;
- the extension of the model to reproduce time series also for tropical regions. The RADDB database could be enlarged with the inclusion of tropical time series of ILWC and IWVC, in order to generate synthetic time series of tropical sites.

CHAPTER 9

APPENDIX A: Cloud type algorithm

9.1 Introduction

Clouds have a definite impact on the propagation of waves at frequencies above 30 GHz and their effect, in terms of path attenuation, must be taken into account. The evaluation of water cloud attenuation A_{cloud} up to approximately 200 GHz is facilitated, being A_{cloud} proportional to the ILWC along the path, i.e. it does not depend on the Droplet Size Distribution (DSD) or, in other terms, on the cloud type (CT). The situation is different if we move from microwave to optical wavelengths that are becoming the new frontier of the advanced telecommunication and space science systems. Indeed, the droplets size results to be much greater than the wavelength (0.8 to 1.5 μm) and the Rayleigh scatter approximation, typical for microwaves, does not hold any more. In this case, the Mie scattering up to its optical limit has to be used. Therefore, the DSD, which depends on the type of clouds, must be properly considered in the calculation of A_{cloud}.

In this Appendix we focus on the study of CT identification and classification. The two databases used are the time-series of the dual-channel MWR collected at the experimental station of Spino d'Adda (RADDB) and high resolution radiosonde observations (RAOBS) launched from Milano Linate airport. Exploiting the information extrapolated by RAOBS measurements we identify a general law to classify the cloud intervals detected into ILWC time series of RADDB. Results indicate that the cloud thresholds identified from RAOBS applies as well to the radiometric measurements. The difference between the occurrence of CT in the two datasets is in the order of a few percent. We also assessed that rain events are detected only in presence of two defined classes of CT (Cloud Type CT3 and CT4).

9.1.1 Cloud type identification

Different water clouds types exist in the troposphere with several shapes and sizes. Clouds are constituted by two components: water droplets and ice crystals. For Satcom systems that transmit at frequency range below 50 GHz, the presence of ice particles along the path, is not expected to produce a considerable attenuation due to ice particle size and low dielectric constant. Differently, water drops contained into clouds cause fading problems that depends on the amount of liquid water content and the vertical extension of cloud.

In literature different classifications of the main cloud types are presented, with some differences related to cloud's thickness [km] and water content [g/m^3]. In Tab. 9.1 [73] and in Tab. 9.2 [11] two classifications are reported.

Table 9.1: *Average properties of different cloud types as presented in [73].*

Cloud type	Average water content (g/m^3)	Average vertical height (km)
Cumulus	1.0	2.0
Cumulonimbus	2.5	2.0
Stratus	0.15	0.5
Stratocumulus	0.3	0.5
Nimbostratus	0.6	0.8
Altostratus	0.4	0.5

Table 9.2: *Average properties of four cloud types as presented in [11].*

Cloud type	Average vertical extent L_v (km)	Average horizontal extent L_h (km)	Average water content (g/m^3)
Cumulonimbus	3.0	4.0	1.0
Cumulus	2.0	3.0	0.6
Nimbostratus	0.8	10.0	1.0
Stratus	0.6	10.0	0.4

The basic idea of the Cloud Type Algorithm CTA is to apply the thresholds identified throughout RAOBS measurements to radiometric measurements to catalogue cloud intervals detected within ILWC time series. The RAOBS data are assumed as reference for this analysis. Water clouds derived from RAOBS data are catalogued according to their thickness in 4 classes (Cloud Type 1 CT1, Cloud Type 2 CT2, Cloud Type 3 CT3 and Cloud Type 4 CT4) and a scatter plot of IWVC against ILWC quantity is depicted for each CT. Looking at the scatter plot of the IWVC against the ILWC the above classes turn out to correspond to different regions that are separated by straight lines (cloud's thresholds). The cloud thresholds are adopted to classify cloudy intervals detected into RADDB time series according to ILWC and IWVC quantity detected within cloud interval. The CTA procedure is here reported.

9.1.1.1 Cloud identification in RAOBS measurements

We start considering a database of 10 years of RAOBS data measured in at the Linate airport (Milano, Italy). The vertical profiles of pressure, relative humidity and temperature are measured and used to derive the IWVC. Since radiosoundings do not measure directly the cloud water, it is necessary to use a cloud-detection algorithm to derive cloud liquid and ice density profiles. Therefore, ILWC and ice is evaluated by means of Salonen Uppala [16] cloud detection algorithm. In our analysis, it is assumed that each RAOBS ascent represents a picture of a cloud situation.

In our analysis we classify each cloud according to its thickness following the parameters defined in Tab. 9.2 and we rename the cloud types as:

- Cloud Type 1 CT1: vertical extent $L_v < 0.7$ km;
- Cloud Type 2 CT2: vertical extent $0.7 \leq L_v < 1.4$ km;
- Cloud Type 3 CT3: vertical extent $1.4 \leq L_v < 2.5$ km;
- Cloud Type 4 CT4: vertical extent $L_v \geq 2.5$ km;

For each CT we create a scatter plot of averaged ILWC and IWVC values evaluated within the cloud interval. In Fig. 9.1 we report the scatter plot of all the selected cloud (composed on both liquid water and ice) where each sample represents a cloud with its IWVC and IWVC components. From these figures we observe that each CT interest mainly a defined area of the scatter plot. We define 4 thresholds that delimit the regions pertinent to each CT. The CT areas delimited by the thresholds reported in Fig. 9.1 are defined in Tab. 9.3.

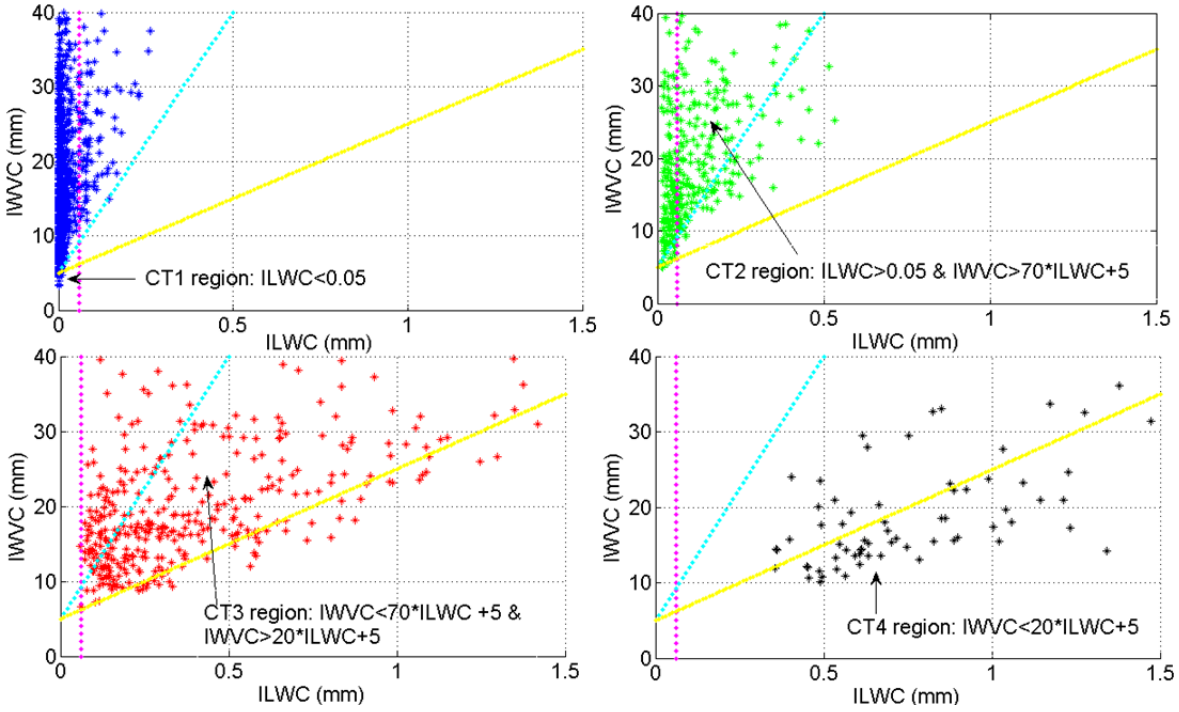

Figure 9.1: *Cloud classification of RAOBS data: Cloud Type 1 CT1 (blue markers),Cloud Type 2 CT2 (green markers),Cloud Type 3 CT3 (red markers) and Cloud Type 4 CT4 (black markers).*

Table 9.3: *Thresholds adopted to detect CT area.*

	Cloud type			
	CT1	CT2	CT3	CT4
Cloud detection area T_i [mm]	L$\leq$0.05	L>0.05 and V$\geq$70L+5	V>70L+5 and V$\geq$20L+5	V<20L+5

Finally, in Tab. 9.4 we report the percentage of occurrence for each CT and the averaged value of liquid water [mm] contained in the clouds of each class. We expect to evaluate a comparable percentage of occurrence of CT in the RADDB measurements.

Table 9.4: *Average cloud properties obtained from RAOBS data collected at Linate airport (Milan, Italy)*

	Cloud type			
	CT1	CT2	CT3	CT4
Frequency of occurrence [%]	56.45	18.70	20.81	4.04
Liquid Water column [mm]	0.0183	0.1105	0.3920	0.7823

9.1.1.2 Cloud identification in RADDB measurements

We considered for this simulation the entire RADDB database composed of 7 years (1994-2000) of radiometric measurement detected in Spino D'Adda (Italy). The time series of ILWC and IWVC quantities are retrieval from the time brightness temperature detected by the radiometer and mass absorption coefficients derived from RAOBS data [43]. An example of a ILWC and IWVC daily time series (24/02/1994) with minutes averaged samples is reported in Fig. 9.2.

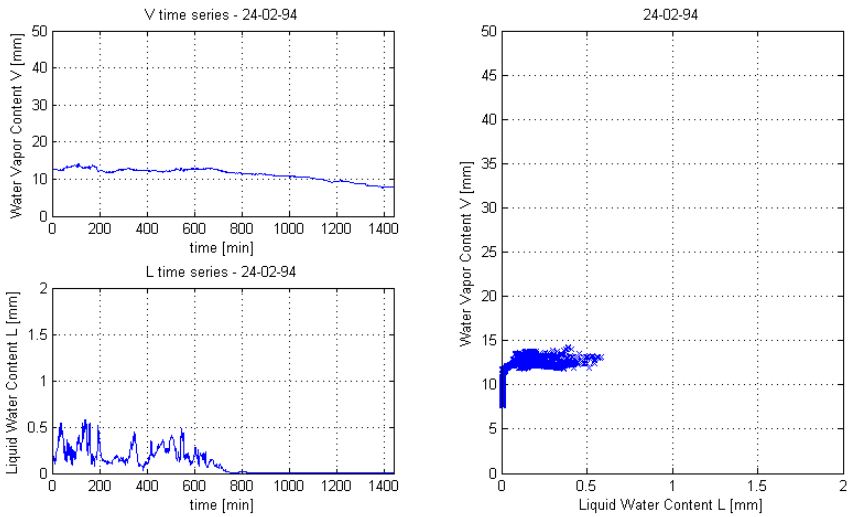

Figure 9.2: *Plot and scatter plot of daily time series of ILWC and IWVC quantities (24/02/1994).*

To remove possible short fluctuation of liquid water, the ILWC time series are low-pass filtered with a moving average of 30 samples length (1 samples each minute) and ILWC values lower than 0.01 mm are set to zero. Once the presence of a cloud is

identified in the ILWC time series, it is catalogued according to the linear dependences of ILWC and IWVC provided that the threshold is overtaken for a given number of minutes.

We identify the following procedure:

1. we first consider only cloud intervals that have all ILWC samples with L<0.05 mm (T_1 area);
2. for each cloud interval we consider the ILWC and IWVC and starting from the higher threshold of Tab. 9.3, the CT4 threshold, we check if there are at least 20 samples that fall into T_4 area, the cloud is classified in CT4 type. If this condition is not verified, we considered the T_3 area of the class below (CT3) and we checked if there are at least 20 samples that fall again in that class, and so on till the last class (CT2);

To be more flexible in the classification, two cloudy intervals that are separated by less than 10 samples are considered as pertinent to the same cloud. On the contrary, cloudy intervals shorter than 30 samples are not classified. Fig. 9.3 show an example of the implementation of CTA algorithm. For the daily time series of ILWC we firstly null the values below 0.01 mm (light green samples) and subsequently we threshold the time series with the upper bound of area T_1. For cloudy intervals shorter that 10 samples (red circles) we assume that they are pertinent to the same cloud, on the contrary for cloudy period shorter that 30 samples (dark green circles) we assume that they are not cloud (clear-sky samples).

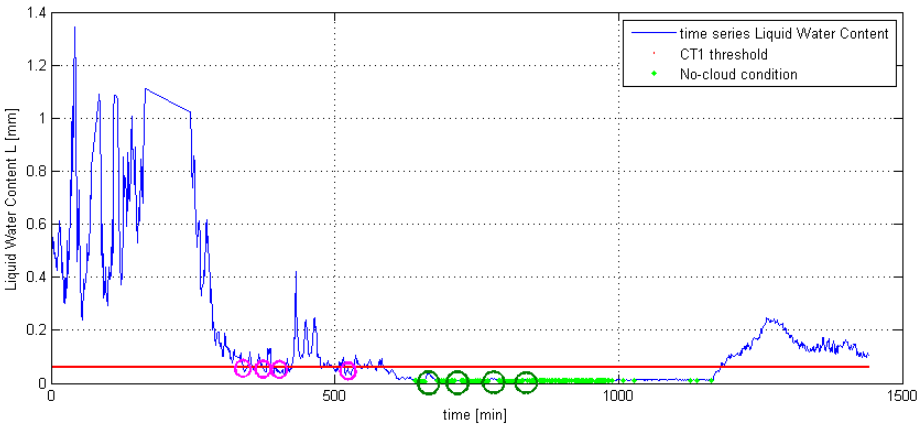

Figure 9.3: *An example of setting of thresholds for the CTA algorithm.*

Finally, in Fig. 9.4 we report an example of the classification of cloud obtained over one year of radiometric measurements (1994) of RADDB. We depict the averaged value of ILWC and IWVC assumed during a cloud interval. In Fig. 9.5 an example of the classification of cloud for two ILWC time series of consecutive days is reported.

9.1.2 Cloud type probability of occurrence

To evaluate the ability of the CTA in determining the CT for the time series we observe the percentage of occurrence of each CT. We consider for this simulation the entire

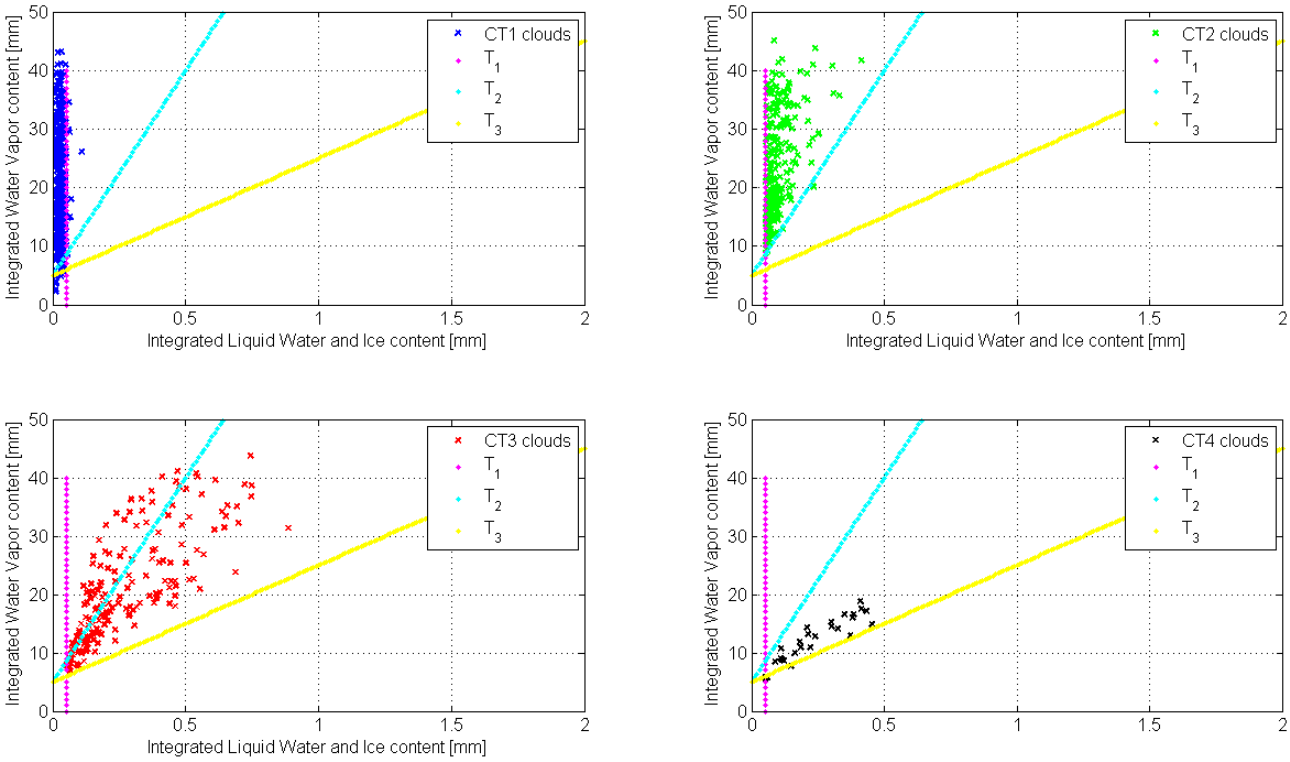

Figure 9.4: *Averaged value of ILWC and IWVC assumed within a cloud for each cloud classified according with thresholds reported in Tab. 9.3 (year 1994).*

RADDB. For each year we classify clouds and we evaluate the percentage of occurrence of each CT. The results are shown in Tab. 9.5 and Fig. 9.6. We observe, despite an acceptable inter annual variation, a good agreement between the classification for RADDB data and the classification for RAOBS measurements (derived from Tab. 9.4). Furthermore, we consider that assuming a simplified classification of CT by grouping classes CT1 and CT2 against CT3 and CT4 the percentage of occurrence are really close (Fig. 9.6 and Tab. 9.7).

9.1.3 Cloud type probability of rain

Finally, the more interesting analysis concerns the identification of which CT are mainly interested by the presence of rain. We keep track of the rainy interval identified in the time series of radiometric measurements and we check which CT are interested by rain events. In Fig. 9.8 we report the percentage of occurrence of rainy intervals within each CT. We observe that the rain intervals are detected, with different probability from year-to-year, only in the CT3 and CT4.

This result highlights that by assuming RAOBS measurements as benchmark for our classification the CTA is able to detects cloud types and reproduce the same probability of occurrence. We also concludes that, in case rain attenuation events must be overlapped to cloudy intervals, the CT3 and CT4 are the one that better agrees with rainy

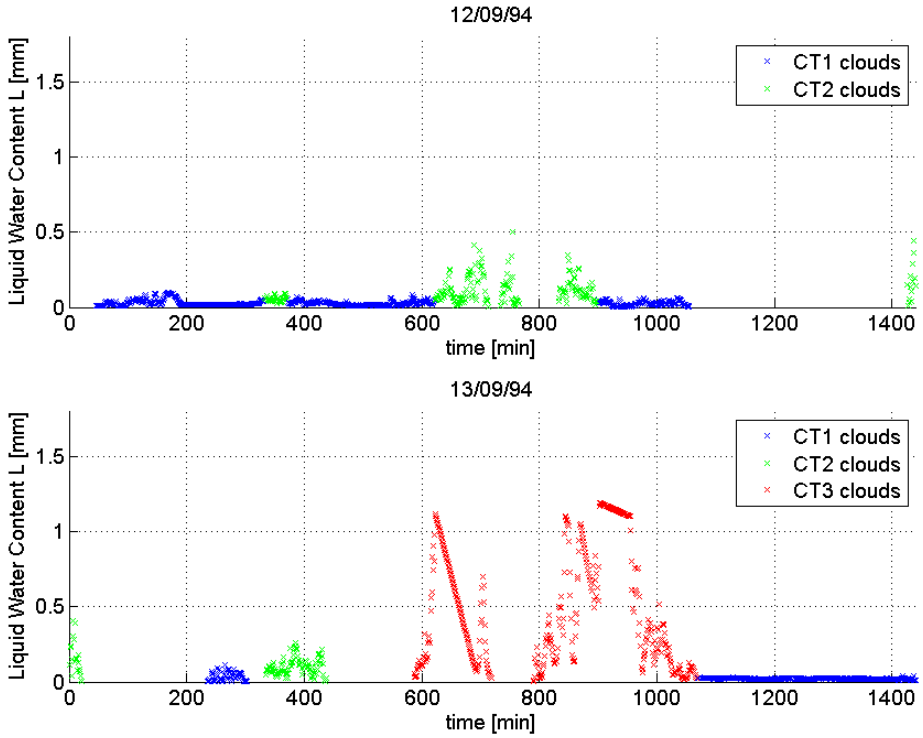

Figure 9.5: *An example of cloud classification for two consecutive daily time series (12 and 13 September 1994).*

Table 9.5: *Percentage for occurrence for different type of Cloud [%]*

	Cloud type			
	CT1	CT2	CT3	CT4
1994	49.68	27.69	19.61	3.02
1995	49.40	25.08	21.81	3.6
1996	47.53	25.63	21.99	4.47
1997	51.86	26.27	17.14	4.4
1998	51.59	24.32	19.83	3.78
1999	51.36	27.09	17.06	4.4
2000	52.43	21.04	20.39	6.04
1994-2000	50.55	25.3029	19.69	4.24429
RAOBS	56.45	18.70	20.81	4.04

condition.

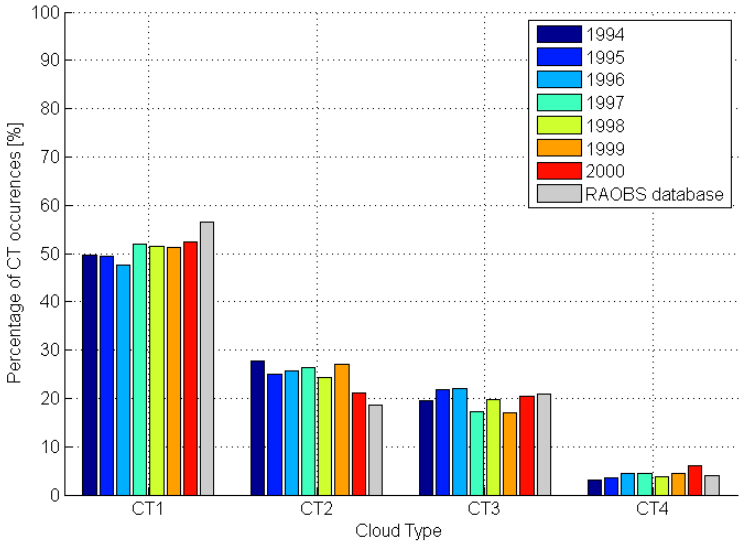

Figure 9.6: *Histogram of percentage of occurrence for each cloud's type (CT1, CT2, CT3 and CT4) for 7 year of radiometric measurements (1994-2000) and for the RAOBS data.*

Table 9.6: *Percentage for occurrence different type of Cloud [%]*

	Cloud type	
	CT1 + CT2	CT3 + CT4
1994	77.37	22.63
1995	74.48	25.41
1996	73.16	26.46
1997	78.13	21.54
1998	75.91	23.61
1999	78.45	21.46
2000	73.47	26.43
1994-2000	75.85	24.15
RAOBS	75.15	24.85

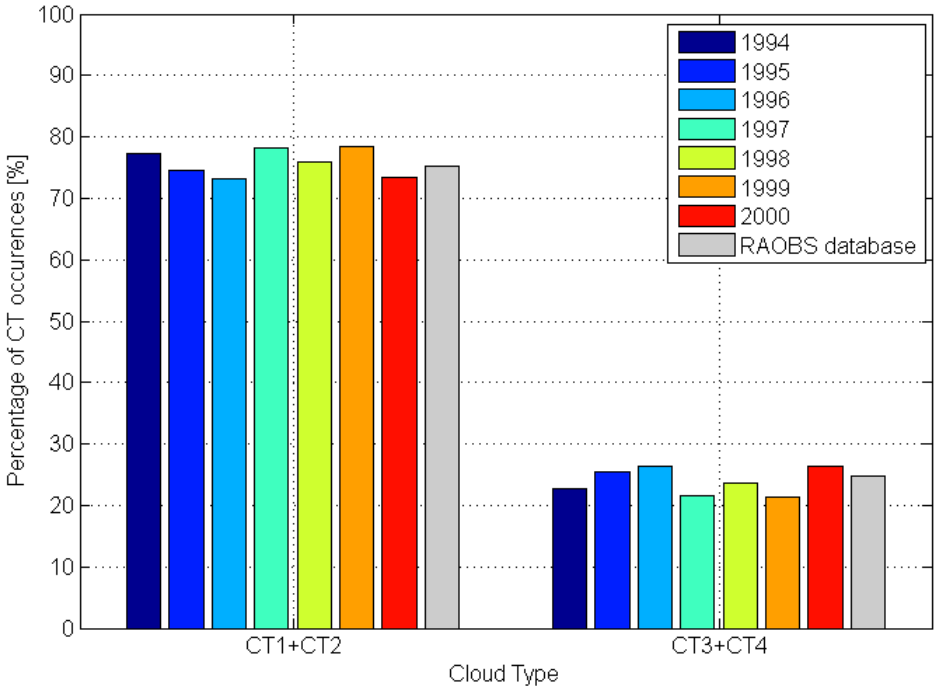

Figure 9.7: *Histogram of percentage of occurrence for two block classification (CT1 and CT2 vs. CT3 and CT4) for 7 year of radiometric measurements (1994-2000) and for the RAOBS data.*

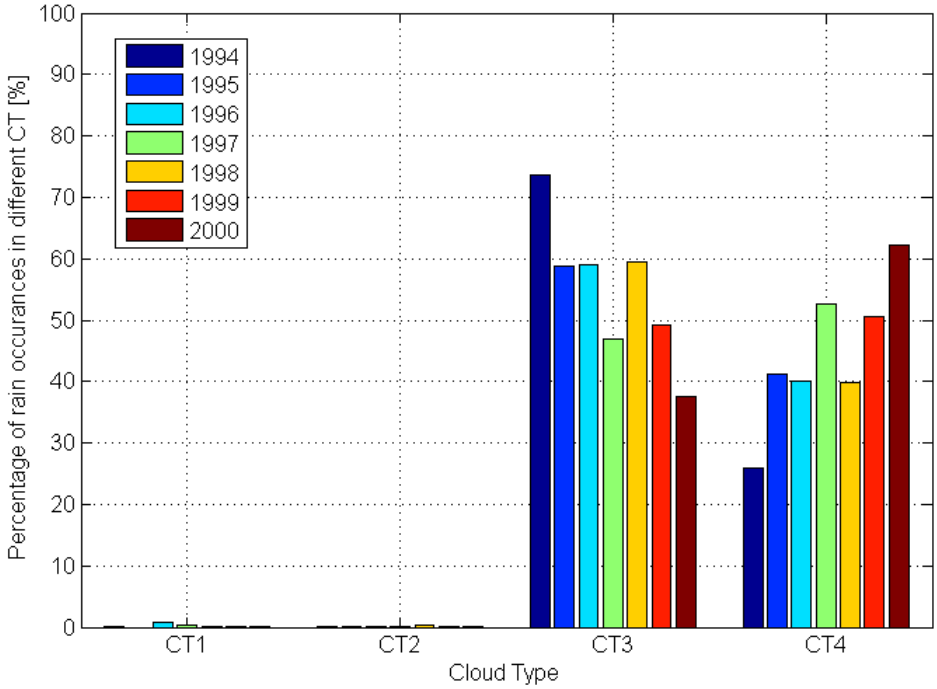

Figure 9.8: *Histogram of percentage of rain occurrence in different CT.*

List of Figures

List of Tables

List of Acronyms

ACM Adaptive Coding and Modulation

BER Bite Error Rate

BF Base Function

BFN Beam Forming Network

CDF Cumulative Distribution Function

CT Cloud Type

CTA Cloud Type Algorithm

DBSG5 Database Study Group 5

DLPC Downlink Power Control

DRR Data Rate Reduction

DSD Drop Size Distribution

ECMWF European Centre of Medium-Range Weather Forecast

EIRP Effective Isotropic Radiated Power

EMB Experimental Measurement Base

EHF Extremely High Frequency

FD Fade Duration

FS Fade Slope

GPS Global Positioning System

ILWC Integrated Liquid Water Content

IWVC Integrated Water Vapor Content

ITDB ITALSAT Database

ITU International Telecommunication Union

ModCod Modulation and Coding

MPA Multi-Port Amplifiers

MSE Mean Square Error

MWR Microwave Radiometer

OBF Objective Function

PDF Probability Distribution Function

PIMT Propagation Impairment Mitigation Technique

RADDB Radiometric Database

RAOBS Radiosonde Observations

REF Result Function

RM Rainy Mask

RMSE Root Mean Square Error

RTSG Rain Time Series Generator

SatCom Satellite Communications

SD Space Diversity

SSI Sky Status Indicator

SNIR Signal to Noise Interference Ratio

TS Time Series

TWTA Traveling-Wave Tube Amplifiers

ULPC Uplink Power Control

Bibliography

[1] "Tropospheric attenuatuon time series synthesis," *ITU-R P.1853-1*, vol. ITU-R P Series Recommendations Radiowave Propagation, 2012.

[2] T. Maseng and P. M. Bakken, "A stochastic dynamic model of rain attenuation," *IEEE Transactions on Communications*, vol. 29, no. 5, pp. 660–669, May 1981.

[3] M. M. J. L. van de Kamp, "Short-term prediction of rain attenuation using two-samples," *Electronics Letters*, pp. 1476–1477, Nov. 2002.

[4] U.C. Fiebig, "Modelling rain fading in satellite communications links," *Vehicular Technology Conference, IEEE VTS 1999,*, vol. 3, pp. 1422–1426, 1999.

[5] M.E.C. Rodrigues, G. Carrie, L. Castanet and L.A.R. da Silva Mello, "A rain attenuation time series synthesizer based on 2-state markov chains coupled to an 'event-on-demand' generator," *Proceedings of EuCAP 2011*, pp. 3865–3869, Rome, Italy,April 11-15, 2011.

[6] E. Matricciani, "Global formulation of the synthetic storm technique to calculate rain attenuation only from rain rate probability distributions," *IEEE International Symposium on Antennas and Propagation*, San Diego, July 5-11, 2008.

[7] L.J. Ippolito, "Radio propagation for space communications systems," *Proceedings of the IEEE*, vol. 69, no. 6, pp. 697–727, June 1981.

[8] "Attenuation by atmospheric gases," *ITU-R P.676-10*, vol. ITU-R P Series Recommendations Radiowave Propagation, 2013.

[9] "Reference standard atmospheres," *ITU-R P.835-5*, vol. ITU-R P Series Recommendations Radiowave Propagation, 2012.

[10] H.J. Liebe,T. Manabe and G.A. Hufford, "MilliÂmeter wave attenuation and delay rates due to fog/cloud conditions," *IEEE Trans. Ant. Prop.*, vol. 37, no. 12, pp. 1617–1623, Dec. 1989.

[11] A. Dissanayake, J. Allnutt and F. Haidara, "Cloud attenuation modelling for shf and ehf applications," *International Journal of Satellite Communications*, vol. 19, pp. 335–345, 2001.

[12] H.C. Van de Hulst, *Light Scattering by Small Particles*.

[13] "Attenuation due to clouds and fog," *ITU-R P.840-6*, vol. ITU-R P Series Recommendations Radiowave Propagation, 2013.

[14] E.E. Altshuler and R.A. Marr, "Cloud attenuation at millimeter wavelengths," *IEEE Transactions on Antennas and Propagation*, vol. 37, no. 11, pp. 1473–1479, 1989.

[15] F. Dintelmann and G. Ortgies, "A semi-empirical model for cloud attenuation prediction," *Electronic letters*, vol. 25, no. 22, pp. 1487–1488, 1989.

[16] E. Salonen, S. Uppala, "New prediction method of cloud attenuation," *Electronic Letters*, vol. 27, no. 12, pp. 1106–1108, Jun. 1991.

[17] "Specific attenuation model for rain for use in prediction methods," *ITU-R P.838-3*, vol. ITU-R P Series Recommendations Radiowave Propagation, 2005.

[18] C. Capsoni, L. Luini, A. Praboni, C. Riva, and A. Martellucci, "A new prediction model of rain attenuation that separately accounts for stratiform and convective rain," *IEEE Transaction on Antennas and Propagation*, Jan. 2009.

[19] "Propagation data and prediction methods required for the design of earth-space telecommunication systems," *ITU-R P.618-11*, vol. ITU-R P Series Recommendations Radiowave Propagation, 2013.

[20] A. Paraboni, A. Martellucci, C. Capsoni and C. Riva, "The physical basis of atmospheric depolarization in slant paths in the v band: Theory, italsat experiment and models," *IEEE Transactions on Antennas and Propagation*, vol. 59, no. 11, pp. 4301–4314, Nov. 2011.

[21] P. Yu, I. Glover,P.A. Watson, O.T. Davies,S. Ventouras, C. Wrench, "Review and comparison of tropospheric scintillation prediction models for satellite communications," *Int J Satellite Comm*, vol. 24, no. 4, pp. 286–302, May 2006.

[22] M. M. J. L. van de Kamp,J.K. Tervonen, E.T. Salonen, B.J.P.V. Poirares Baptista, "Improved models for long-term prediction of tropospheric scintillation on slant paths," *IEEE Transactions on Antennas and Propagation*, vol. 47, no. 2, pp. 249–260, Feb 1999.

[23] F. S. Marzano, G. D'Auria, "Model-based prediction of amplitude scintillation variance due to clear-air tropospheric turbulence on earth-satellite microwave links," *IEEE Transactions on Antennas and Propagation*, vol. 46, no. 10, pp. 1506–11 518, Oct 1998.

[24] L. Castnanet, A. Bolea-Alamanac, M. Bousquet, "Iterference and fade mitigation techniques for ka and q/v band satellite communication systems," *in Proc. Int. Workshop on COST Actions 272 and 280, Noordwijk, The Netherlands*, May 2003.

[25] A.D. Panagopoulos, P.D.M. Arapoglou, and P.G. Cottis, "Satellite communications at ku, ka, and v bands: propagation impairments and mitigation techniques," *IEEE Communications Surveys and Tutorials*, vol. 6, no. 3, pp. 660–669, Oct. 2004.

[26] MJ. Willis, BG. Evans, "Fade countermeasures at ka-band for olympus," *Int. Jour. Sat. Com*, vol. 6, pp. 301–311, June 1988.

[27] G. Tartara, "Fade countermeasures in millimetre-wave satellite communications : a survey of methods and problems," *Proc. Olympus Util. Conference*, Vienna, Austria, April 1989.

[28] B. Arbesser-Rastburg, A. Martellucci, O. Fiser, D. Vanhoenacker, E. Salonen, C. Riva, T. Tjelta, J.P.V. Poiares Baptista, F. Perez-Fontan, M. Dottling, S. Saunders, M. Vasquez-Castro, A. Formella, I. Frigyes, M. Pettinger, M. Schnell, L. Castanet, M. Filip, D. Mertens, P.A. Watson and J. Habetha, *COST Action 255 Final Report: Radiowave Propagation for SatCom Services at Ku-Band and Above*. ESA Publications Divison, Mar. 2002.

[29] R.G. Lyons, "A statistical analysis of transmit power control to compensate up- and down-link fading in an fdma satellite communications system," *IEEE Trans. Commun*, vol. 24, pp. 622–636, June 1916.

[30] C. Capsoni, A. Paraboni, C. Riva, E. Matricciani, L. Luini, M. Luccini, R. Nebuloni, L. Resteghini, L. Castanet, N. Jeannin, G. Carrie, J. Lemorton, P. Gabellini and F. De Cecca, "Verification of propagation impairment mitigation techniques," *ESA/ESTEC/Contract N° 20887/06/NL/LvH*, 2011.

[31] M. Aloisio, E. Casini and A. Ginesi, "Evolution of space traveling-wave tube amplifier requirements and specifications for modern communication satellites," *IEEE Trans. Electron Devices*, vol. 54, no. 7, pp. 1587–1596, Jul. 2007.

[32] M. Aloisio, P. Angeletti, E. Colzi, S. D'Addio, R. Oliva-Balague, E. Casini and F. Coromina, "End-to-end performance evaluation methodology for twta-based satellite flexible payloads," *Proc. IVEC*, pp. 175–176, 2008.

[33] P. Gabellini, A. Paraboni, A. Martellucci, P. Rinous, A. Nakazawa, N. Gatti, F. Maggio, C. Capsoni and L. Resteghini, "The rf design of a ka-band reconfigurable broadcast antenna for atmospheric fade mitigation," *ESA Workshop on Radiowave Propagation 2011*, Noordwijk, The Netherlands, Dec. 2011.

[34] J.G. Proakis, *Digital Communications*. McGraw Hill, 2001.

[35] G. Carrie, L. Castanet, F. Lacoste, "Validation of rain attenuation time series synthetizers for temperate areas," *International workshop on satellite and space communications*, Toulouse, October 1-3, 2008.

[36] M. M. J. L. van de Kamp, "Rain attenuation as a markov process, using two samples," *Post-doctorate thesis, Document ONERA RT 1/06733.04 DEMR,Toulouse, France*, pp. 1–5, March 2003.

[37] M.M. J. L. van de Kamp, "The two-sample model: Short-term prediction of rain attenuation," *Proceedings of the First European Coriference on Antennas and Propagation*, pp. 1–5, 2006.

[38] U.C. Fiebig, L. Castanet, J. Lemorton, E. Matricciani, F. Perez-Fontan, C. Riva and R. Watson, "Review of propagation channel modelling," *2nd Workshop of the COST 280 Action 'Propagation Impairments Mitigation for Millimetre-Wave Radio Systems', ESA/ESTEC, Noordwijk, The Netherlands*, pp. 1476–1477, 26-28 May 2003.

[39] G. Carrie, F. Lacoste, and L. Castanet, "New 'on-demand' channel model to synthesize rain attenuation time series at ku-, ka- and q/vbands," *International Journal of Satellite Communications and Networking, Special issue on Channel Modelling and Propagation Impairment Simulation*, November 2009.

[40] F. Lacoste, M. Bousquet, F. Cornet, L. Castanet, and J. Lemorton, "Classical and on-demand rain attenuation time series synthesis: Principle and applications," *Proceedings of 24th AIAA-ICSSC Conference*, San Diego, California,June 2006.

[41] E. Matricciani, "Physical-mathematical model of the dynamics of rain attenuation based on rain rate time-series and a two-layer vertical structure of precipitation," *Radio Science*, pp. 281–295.

[42] "Annual mean surface temperature," *ITU-R P.1510-0*, vol. ITU-R P Series Recommendations Radiowave Propagation, 2001.

[43] L. Luini, C. Riva, C. Capsoni, A. Martellucci, "Attenuation in non rainy conditions at millimeter wavelengths: assessment of a procedure," *IEEE Transactions on Geoscience and Remote Sensing*, vol. 45, no. 7, pp. 2150–2157, Jul. 2007.

[44] J.C. Liljegren, E.E. Clothia, G.G. Mace, S. Karo and X. Dong, "Journal of geophysical research," *A new retrieval for cloud liquid water path using a ground-based microwave radiometer and measurements of cloud temperature*, vol. 106, no. 13, pp. 485–500, Jul. 2001.

[45] D. Turner, A. Clough, J. C. Liljegren, E. E. Clothiaux, K. E. Cady-Pereira and K. L. Gaustad, "Retrieving liquid water path and precipitable water vapor from the atmospheric radiation measurement (arm) microwave radiometers," *IEEE Trans. Geosci.*, vol. 45, no. 11, pp. 3680–3690, Nov. 2007.

[46] C. Riva, "Characterisation and Modelling of Propagation Effects in 20-50 ghz Band," ESA, The Nederlands, Final report for the European Space Agency under ESTEC Contract No. 17760/03/NL/JA, 2006.

[47] Zhien Wang, "A refoned two-channel microwave radiometer liquid water path retrieval for cold regions by using multiple-sensor measurements," *IEEE Geoscience and remote sensing letters*, vol. 4, no. 4, pp. 591–595, Oct. 2007.

[48] D. Cimini, E.R. Westwater, A.J. Gasiewski, M. Klein, V.Y. Leuski and J.C. Liljegren, "Ground-based millimeter- and submillimeter-wave observations of low vapor and liquid water contents," *IEEE T. Geosci*, vol. 45, pp. 2169–2180, 2007.

[49] J.C. Liljegren, "Combining microwave radiometer and millimeter cloud radar to improve integrated liquid water retrievals," *Ninth ARM Science Team Meeting Proceedings*, March 1999.

[50] "Characteristics of precipitation for propagation modelling," *ITU-R P.837-6*, vol. ITU-R P Series Recommendations Radiowave Propagation, 2012.

[51] M. Mauri, C. Riva, "Nine years of statistics of meteorological parameters at spino d'adda," *Proc. CLIMPARA Conference*, Budapest, Hungary, 2001.

[52] C. Riva, "Seasonal and diurnal variations of total attenuation measured with the italsat satellite at spino d'adda at 18.7, 39.6 and 49.5 ghz," *International Journal of Satellite Communications and Networking*, vol. 22, no. 4, pp. 449–476, 2004.

[53] A.V. Bosisio and C. Capsoni, *Effectiveness of birghtness temperature ratios as indicator of the atmospheric path conditions*. Microwave Radiometry and Remote Sensing of Environment (Editor: D.Solimini).

[54] A.V. Bosisio, C. Capsoni, "Brightness temperature ratios: analysis of typical behaviour," *Proc. IGARSS*, vol. 2, p. 1133, 1995.

[55] V. Mattioli, A. Graziani, P. Tortora, A.V. Bosisio and L. Castanet, "Analysis and improvements of methodologies for discriminating atmospheric conditions from radiometric brightness temperatures," *IEEE Proc. 7th European Conference on Antennas and Propagation (EuCAP)*, pp. 1392 – 1396, 8-12 April 2013.

[56] A.V Bosisio , E. Fionda, P. Ciotti and A. Martellucci, "Preliminary results on the performance of an indicator to identify the status of the sky along a satellite link by means of ground-based brightness temperatures," *IEEE Proc. 7th European Conference on Antennas and Propagation (EuCAP)*, pp. 268 – 272, 8-12 April 2013.

[57] L. Resteghini, C. Capsoni1, C. Riva, "Analysis of liquid water and water vapor time series and rainy period detection from a two channel microwave radiometer," *IEEE Proc. 8th European Conference on Antennas and Propagation (EuCAP)*, 7-11 April 2014.

[58] J.L. Agnew, "A method for ongoing validation of profiling microwave radiometer water vapor products using radiosonde data," *SP-636 Envisat Symposium 2007*, 2007.

[59] M.G. Divakarla, C.D. Barnet, M.D. Goldberg, L.M. McMillin, E. Maddy, W. Wolf, L. Zhou, and X. Liu, "Validation of atmospheric infrared sounder temperature and water vapor retrievals with matched radiosonde measurements and forecasts," *Journal of Geophysical Research*, vol. 111, 2006.

[60] P. Ciotti, E. Di Giampaolo, P. Basili, S. Bonafoni, V. Mattioli, R. Biondi, E. Fionda, F. Consalvi, A. Memmo, D. Cimini, R. Pacione, and F. Vespe, "Validation of meris water vapour in the central italy by concurrent measurements of microwave radiometers and gps receivers," *Proc. IGARSS*, Jul. 2003.

[61] G. Drufuca, "Rain attenuation statistics for frequencies above 10 ghz from rain gauges observations," *J. Researches Atmospheriques*, vol. 8, no. 1-2, Jan.-June 1974.

[62] C. Capsoni, F. Fedi, C. Magistroni, A. Pawlina and A. Paraboni, "Data and theory for a new model of the horizontal structure of rain cells for propagation applications," *Radio Science*, vol. 22, no. 3, pp. 395–404, 1987.

[63] C. Capsoni, F. Fedi and A. Paraboni, "A comprehensive methodology for the prediction of wave propagation parameters in telecommunication applications beyond 10 ghz," *Radio Science*, vol. 22, no. 3, pp. 387–393, 1987.

[64] S. Bertorelli, C. Riva, L. Valbonesi, "Generation of attenuation time series for simulation purposes starting from italsat measurements," *IEEE Transactions on Antennas and Propagation*, vol. 56, no. 4, pp. 1094–1102, Apr. 2008.

[65] L. Luini, N. Jeannin, C. Capsoni, A. Paraboni, C. Riva, L. Castanet and J. Lemorton, "Weather radar data for site diversity predictions and evaluation of the impact of rain field advection," *Int. J. Satell. Commun. Network*, vol. 29, pp. 79–96, 2001.

[66] "Acquisition, presentation and analysis of data in studies of tropospheric propagation," *ITU-R P.311-14*, vol. ITU-R P Series Recommendations Radiowave Propagation, 2013.

[67] "Itu-r database and software online, online database and softwarespecific to the work of study group, sg3," *Databanks and computer programs on radiowave propagation , Databank DBSG5, ITU-R website, Online*, Jul 2005.

[68] "Tropospheric attenuatuon time series synthesis," *ITU-R P.1853-0*, vol. ITU-R P Series Recommendations Radiowave Propagation, 2009.

[69] "Prediction method of fade dynamics on earth-space paths," *ITU-R P.1623-1*, vol. ITU-R P Series Recommendations Radiowave Propagation, 2005.

[70] A. Paraboni and C. Riva, "A new method for the prediction of fade duration statistics in satellite links above 10 ghz," *Int. J. Satell. Commun.*, vol. 12, pp. 387–394, 1994.

[71] M.M.J.L. van de Kamp, "Statistical analysis of rain fade slope," *IEEE Transactions on antennas and propagation*, vol. 51, no. 8, pp. 1750–1759, 2003.

[72] L. Luini, C. Riva and C. Capsoni, "Reduced liquid water content for cloud attenuation prediction: the impact of temperature," *Electronics Letters*, vol. 49, no. 20, pp. 1259–1261, Sept. 2013.

[73] G.L. Stephens, "Radiation profiles in extended water clouds," *Journal of the Atmospheric Sciences*, vol. 35, pp. 2111–2122, 1978.

Publications with the author's contribution

Publications on Journals

- C. Capsoni, L. Castanet, P. Gabellini, A. Martellucci, G. Carrie, G. Gallinaro, N. Gatti, N. Jeannin, M. Luccini, L. Luini, R. Nebuloni, A. Paraboni, L. RESTEGHINI, C. Riva, "Rain field generators implemented in a European broadcasting satellite system using OBAPR: output results from an ESA study ", Space Communications Journal, In Press.
- R. Nebuloni, L. RESTEGHINI, M. Luccini, C. Capsoni, C. Riva, A. Martellucci, P. Gabellini, "Presentation of the Analysis Tool for Design of Onboard Reconfigurable Antenna for Broadband Satcom and Broadcast Services ", Space Communications Journal, In Press.

Publications on Congress Proceedings

- L. RESTEGHINI, C. Capsoni, C. Riva, "Analysis of Liquid Water and Water Vapor TimeSeries and Rainy Period Detection from a TwoChannel Microwave Radiometer ", The 8th European Conference on Antennas and Propagation (EuCAP 2014), The Hague, The Netherlands, April 8-12, 2014, pp. 1333-1335;
- L. RESTEGHINI, C. Capsoni, L. Luini, R. Nebuloni, "An attempt to classify the types of clouds by a dual frequency microwave radiometer " Proceeding of Microrad 2014 Conference, Pasadena, March 2014;
- L. RESTEGHINI, P. L. Lanzi, R. Nebuloni, C. Riva, C. Capsoni, P. Gabellini, "Single-Objective Genetic Algorithm for Dynamic Optimization of Reconfigurable Antenna Systems", The 7th European Conference on Antennas and Propagation (EuCAP 2013), Gothenburg, Sweden, April 8-12, 2013, pp. 1333-1335;
- R. Nebuloni , C. Capsoni, C. Riva , L. RESTEGHINI, "Prediction of Microwave Attenuation Across a Satellite Link From the ERA-Interim Global Atmospheric Database", The 7th European Conference on Antennas and Propagation (EuCAP 2013), Gothenburg, Sweden, April 8-12, 2013, pp. 1333-1335;
- C. Capsoni, M. Luccini, L. Luini, R. Nebuloni, L. RESTEGHINI, C. Riva, "Joint measurements exploiting the European ground network for the Alphasat experiment", Proc. of the first CNES-ONERA Workshop on Earth-Space Propagation, Toulouse, France, 21-23 January 2013;
- L. RESTEGHINI, C. Capsoni, R. Nebuloni, P. Gabellini, F. Maggio, A. Martellucci, P. Rinous, "Effect of Non-Ideal Components on the Performance of a Reconfigurable on-Board Antenna for Broadcasting Applications", The 6th European Conference on Antennas and Propagation (EuCAP 2012), Prague, Czech Republic, March 26-30, 2012, pp. 1487 - 1490;
- P. Gabellini, N. Gatti, C. Capsoni, L. RESTEGHINI, A. Martellucci, P. Rinous, "An On-Board Reconfigurable Antenna System for Ka-Band Broadcasting Satellite Services", The 6th European Conference on Antennas and Propagation (EuCAP 2012), Prague, Czech Republic, March 26-30, 2012, pp. 2636 - 2640;

- C. Capsoni, M. Luccini, L. Luini, E. Matricciani, R. Nebuloni, A. Paraboni, L. RESTEGHINI, C. Riva, L Castanet, G. Carrie, N. Jeannin, P. Gabellini, G. Gallinaro, N. Gatti, "Results and Conclusions on the Verification of Propagation Impairments Mitigation Techniques for SatCom Systems", Proc. of ESA Workshop on Radiowave Propagation 2011, Noordwijk, The Netherlands, 30 November - 2 December 2011, pp. 1-17;
- A. Martellucci, R. Nebuloni, L. RESTEGHINI, M. Luccini, C. Capsoni, C. Riva, P. Gabellini, "Presentation of the analysis tool for design of onboard reconfigurable antenna for broadband SatCom and broadcast services, Proc. of ESA Workshop on Radiowave Propagation 2011, Noordwijk, The Netherlands, November 30 - December 2, 2011, pp. 1-6;
- A. Paraboni, A. Martellucci, C. Capsoni, F. Maggio, L. RESTEGHINI, N. Gatti, P. Rinous, P. Gabellini, R. Nebuloni, S. Nakazawa, "The RF Design OF a Ka-Band Reconfigurable Broadcast Antenna for Atmospheric Fade Mitigation", Proc. of the 33rd ESA Antenna Workshop on Challenges for Space Antenna Systems, ESTEC - Noordwijk (The Netherlands), 18-21 October 2011;
- A. Paraboni, C. Capsoni, L. RESTEGHINI, R. Nebuloni, M. Luccini, "A Theoretical Approach for the Dynamic Reconfiguration of an On-Board Antenna Pattern and Its Performance Assessment", The 5th European Conference on Antennas and Propagation (EuCAP 2011), Rome, Italy, April 11-15, 2011, pp. 3953 - 3957;
- A. Paraboni, L. RESTEGHINI, R. Nebuloni, "Adaptive Distribution of the Radiated Power in Ka Telecommunications Satellite Systems " Proc. of the 12th URSI Commission F Triennial Open Symposium on Radio Wave Propagation and Remote Sensing, Garmisch-Partenkirchen (Germany), 8-11 March 2011.

Technical reports

- C. Riva, L. RESTEGHINI, R. Nebuloni, "TLC SOFTWARE Tool User Manual (Output of CCN Reconfigurable Ka-Band Antenna)", ESA CONTRACT No. 17877/04/NL/LvH CCN 002, 2011.
- A. Paraboni, C. Capsoni, C. Riva, E. Matriciani, F. De Cecca, G. Carrie, J. Lemorton, L. RESTEGHINI, L. Castanet, L. Luini, M. Luccini, N. Jeannin, P. Gabellini, R. Nebuloni, "Verification of Propagation Impairment Mitigation Techniques ", Final Report of ESA/ESTEC/Contract No. 20887/07/NL/LvH, 2011.
- C. Capsoni, L. RESTEGHINI, R. Nebuloni, "Baseline Antenna Reconfiguration Performance Assessment (Output of WP 4400) ", Demonstrator of a Reconfigurable Ka-Band Tx Antenna for Rain-Fade Mitigation for Broadcasting Satellite Systems - ESTEC Contract No. 22216/09/NL/ST, 2011.
- C. Capsoni, F. Foschi, F. Maggio, G. La Terza, L. RESTEGHINI, P. Gabellini, R. Nebuloni, "Baseline Antenna RF Performance Assessment (Output of WP4300) ",Demonstrator of a Reconfigurable Ka-Band Tx Antenna for Rain-Fade Mitigation for Broadcasting Satellite Systems - ESTEC Contract No. 22216/09/NL/ST, 2011.
- P. Gabellini, N. Gatti, M. Monopoli, R. Nebuloni, L. RESTEGHINI, C. Riva, "Final Report (Output of CCN Reconfigurable Ka-Band Antenna) " ESA CONTRACT No. 17877/04/NL/LvH CCN 002, 2012.